January 2016

LASER SHOCK IMPRINTING OF METALLIC NANOSTRUCTURES AND SHOCK PROCESSING OF LOW-DIMENSIONAL MATERIALS

Yaowu Hu
Purdue University

Follow this and additional works at: https://docs.lib.purdue.edu/open_access_dissertations
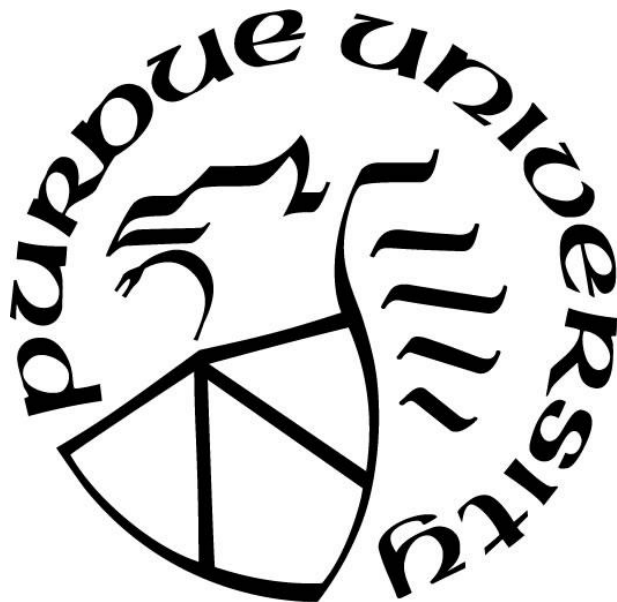
LASER SHOCK IMPRINTING OF METALLIC NANOSTRUCTURES AND SHOCK PROCESSING OF LOW-DIMENSIONAL MATERIALS

by

Yaowu Hu

A Dissertation

Submitted to the Faculty of Purdue University

In Partial Fulfillment of the Requirements for the degree of

Doctor of Philosophy

School of Industrial Engineering

West Lafayette, Indiana

December 2016

THE PURDUE UNIVERSITY GRADUATE SCHOOL
STATEMENT OF DISSERTATION APPROVAL

Dr. Gary J. Cheng, Chair

    School of Industrial Engineering

Dr. Peide Ye

    School of Electrical and Computer Engineering

Dr. Joseph Irudayaraj

    School of Agricultural and Biological Engineering

Dr. Ramses V. Martinez

    School of Industrial Engineering

Dr. Yi Xuan

    School of Industrial Engineering

Approved by:

    Dr. Abhijit Deshmukh

        Head of the Departmental Graduate Program

To my beloved family

ACKNOWLEDGMENTS

TABLE OF CONTENTS

LIST OF FIGURES

ABSTRACT

Author: Hu, Yaowu. Ph.D.
Institution: Purdue University
Degree Received: December 2016
Title: Laser Shock Imprinting of Metallic Nanostructures and Shock Processing of Low-dimensional Materials.
Major Professor: Gary J. Cheng

Laser shock imprinting (LSI) is proposed and developed as a novel ultrafast room-temperature top-down technique for fabricating and tuning of plasmonic nanostructures, and processing of one-dimensional semiconductor nanowires and two-dimensional crystals. The technique utilizes a shock pressure generated by laser ablation of sacrificial materials. Compared with conventional technologies, LSI features ambient condition, good scalability, low cost and high efficiency.

In this study, LSI is demonstrated as a top-down method for the fabrication of free-standing flexible nano-engineered metallic nanoarrays. Large-scale ordered structures with the capability of strong optical field enhancement, such as ultra-sharp 3D pyramids, 2D tips, and nanotrenches with 10-nm gaps, are nanoimprinted within nanoseconds and integrated with graphene. Polarized Raman spectroscopy of the suspended graphene veiled on shocked hybrid film reveals significantly enhanced and actively controlled light-matter interaction. By testing in reactive environment, elevated temperatures, and in the application of molecular sensing, the hybrid platform shows a significantly enhanced stability of light-matter interaction. In addition, LSI is applied to enable shock turning of an ordered metallic nanostructure and generate precise nanogap closing. It is found that the modification of nanoarray geometries is controlled by laser fluence and is nanoscale size dependent. A deformable transfer layer introduces a self-limiting effect with its collaborative superplastic flow with the target arrays, which forms a line-gap at sub-10 nm scale. Ultrafast opto-mechanical tuning of metallic nanoarrays with various designs is further demonstrated. Processed nanoantennas show red-shifts of their surface plasmon resonances and enhanced local fields, which significantly influence their performances in

applications such as surface enhanced Raman scattering. Finally, laser shock processing of semiconductor nanowires and 2D crystals is presented. This study develops a CMOS-compatible top-down fabrication methodology with the aid of laser shock to achieve large scale nanoshaping of nanowires in parallel with tunable elastic strains. As a result of 3D straining, the inhomogeneous elastic strains in GeNWs result in notable Raman peak shifts and broadening, and enhancement of electronic properties. Ultrafine graphene-copper hybrid nanostructures is also achieved by LSI in one step. The presented nanoshaping opens a new avenue to manipulate nanomaterials with tunable electrical-optical properties and create many opportunities for nanoelectronics, nano-electrical-mechanical system, quantum devices.

1. INTRODUCTION

1.1 Motivation

Lasers have been widely applied in almost every section of modern society, including entertainment, surgery, manufacturing, communication, spectroscopy and military. In the area of manufacturing and material processing, the control of parameters such as laser wavelength, power density, and time scale of laser-matter interaction creates opportunities for various processing domains. The advantages of laser manufacturing over conventional processes are characteristics such as contact-free processing, high efficiency and flexibility, spatial and temporal selectivity, and low environmental impact. Laser thermal engineering[1–5] has been intensely studied in additive and subtractive manufacturing. For example, laser selective melting/sintering, has been actively developed to in emerging 3D printing and remanufacturing for extended service life. Laser mechanical shock engineering[6–8], a different approach which utilizes the shock pressure generated through material ablation and plasma expansion, has been found to introduce significant changes of microstructural and mechanical property of targeted material and enhance fatigue life.

The emergence of nanoscale science and technology triggered enormous research interests and needs to develop understanding and manipulation methods of new materials in smaller scales. Moore's law[9], a prediction of the exponential growth of the number of components per integrated circuit, has been the golden rule for electronics industry for decades, and imposed economic and technological impacts on our society extensively. The need for size shrinking and creation of multifunctional devices calls for novel fabrication techniques which could effectively and efficiently tackle stringent requirements at increasingly smaller scale. In general, the fabrication techniques could be categorized into top-down approach and bottom-up approach. For example, the metallic nanocomponents have potential applications in photonics and optoelectronics. The bottom-up approach includes guided growth and self-assembly, which suffers from difficulties in controllability, reproducibility, and scalability. The top-down approach such as conventional lithography processes is typically inefficient and requires complex procedures, high vacuum and a

cleanroom to operate. Exploring novel approaches for efficient and effective manufacturing at low cost is highly desirable.

Laser based/assisted nano-manufacturing has been an exciting and promising route for ultrafast and tunable nanomaterial processing[10–19]. The investigation of materials responses under laser shock, a high-strain rate and high pressure transient process, has been limited to bulk materials[6,20] and the study in nanoscale remains largely unexplored[21]. The utilization of laser shock in nanomaterial deformation could yield interesting properties for harvesting. Throughout this study, the laser shock induced nanoshaping of various metals, low-dimensional materials, and hybrid systems will be explored.

1.2   Objectives

The aim of this thesis is to develop a versatile top-down fabrication technique capable of defining metallic nanostructures at 10-nm scale, with the utilization of laser shock. The behavior of low-dimensional materials under the impact of laser shock is studied to expand the regime of conventional laser-shock-processible material from the metallic to nonmetallic, from ductile to brittle, and from the three-dimensional to one- or two-dimensional materials. Nanoscale metallic nanostructures such as aluminum, silver, gold, copper and materials with higher hardness could be deformed. Based on the above motivation, we aim to accomplish the following objectives related to laser shock processing of plasmonic nanostructures and 2D crystals:

(a) Explore the capability of laser dynamic forming in nanoscale and even in sub-10 nm dimensions. We will focus on the dimensional limit, surface quality of fabricated nanostructures, and grain movement during laser shock processing, with both experimental and numerical studies. Finite element method based on continuum mechanics and Molecular dynamics will be used to yield insights on mechanism of the high-strain-rate forming at nanoscale.

 (b) Study the optical properties of such patterned metallic nanostructures. The fabricated nanostructures will be studied in terms of their field enhancement capabilities under

incoming laser excitations. Surface enhanced Raman scattering effect, and enhanced fluorescence effects of these substrate will be studied. Optical reflectance of these nanostructures will be calculated by finite-difference time-domain simulation technique. Molecular sensing capability of these substrate will be demonstrated.

(c) Investigate the effect of laser shock on pre-defined optical antennas. The effect of laser shock on symmetrical Au nanoantennas defined by Electro-beam lithography will be studied. A variation laser shock pressure will be applied. Laser shock processing of complex shapes of nanoantennas will be carried out. Dark field spectroscopy and Raman spectroscopy are used to monitor optical properties change after laser shock. Molecular dynamics will be used to study the mechanism of laser shock on nanoantennas.

(d) Research on laser shock direct patterning of low-dimensional materials such as nanowires and 2D crystals. CVD graphene grown on copper will be directly imprinted by laser shock. The fabricated hybrid system with nanostructured graphene and metals will be studied. Straining effect of graphene after shock imprinting will be quantified by polarized Raman scattering. Plasmonic field enhancemnt of this hybrid structure will be demonstrated by using near field scattering microscopy and Raman spectroscopy.

1.3   Structure of the Dissertation

This dissertation is structured as follows. (1) Chapter 1 is the introduction. (2) Chapter 2 gives a literature review of research works in related areas. (3) Chapter 3 summarizes the material characterization techniques used in this thesis. (4) In Chapter 4, the experimental and numerical study of laser shock imprinting of various materials is performed. The fabrication of free-standing nenoengineered metallic nanoarrays and graphene-plasmonic hybrid film on flexible substrate is enabled by the technique. (5) In Chapter 5, laser shock is developed as a general strategy for superplastic forming and precise nanoscale gap tuning of ordered metallic nanostructures. (6) In Chapter 6, the application of laser shock imprinting in the deformation of emerging materials such as semiconductor nanowire and 2D crystals is studied. (7) Chapter 7 is the summarization of this dissertation.

2. BACKGROUND AND LITERATURE REVIEW

2.1 Pressure generation in high-power-density laser-matter interaction

The interaction of high-power-density laser with matter is highly complex due to multiphysics phenomena such as electron excitation, phase transitions, plasma dynamics, and nonlinearities in material responses under high temperature and high pressure. Typically, when the laser intensity is larger than 10^6 W/cm^2, evaporation and plasma come into play. The associated recoil pressure could significantly deform the free surface of the molten material and result in the formation of a keyhole, bring applications significantly different from low-intensity laser thermal processes such as selective sintering and melting[22–26]. At extremely high intensities, ablation pressure could drive a shock wave into the materials and introduce modulation of structures and physical properties of the material[27–29].

In traditional laser shock peening, the pulsed laser usually has an intensity larger than 1 GW/cm^2 and pulse duration a few nanoseconds. A simplified model for laser induced shock momentum by Fabbro and coworkers[29–34],

$$\frac{dL(t)}{dt} = \frac{2}{Z}P(t) \qquad\qquad \text{Eq. 2.1}$$

$$I(t) = P(t)\frac{dL(t)}{dt} + \frac{3}{2\alpha}\frac{d}{dt}[P(t)L(t)] \qquad\qquad \text{Eq. 2.2}$$

where P(t) is the laser induced shock pressure at given instant, I(t) the effective laser intensity at time t, L(t) the thickness of the interface at time t. α is a constant to represent a fraction of internal energy related to pressure. Z is the shock impedance given by[35],

$$\frac{2}{Z} = \frac{1}{Z_1} + \frac{1}{Z_2} \qquad\qquad \text{Eq. 2.3}$$

where Z_1 and Z_2 are the impedances for the target metal and the confining media, respectively. Figure 2.1 shows a typical laser intensity temporal profile and the resulted plasma pressure for shock peening.
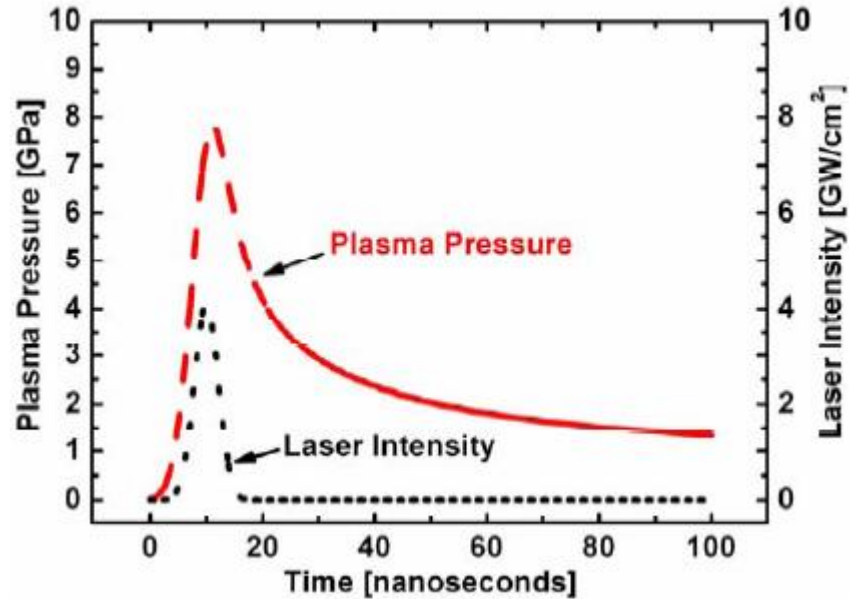
2.1 Temporal profiles of laser intensity and generated plasma pressure.[36]

2.2   Fabrication of metallic nanostructures

Nanostructured plasmonic surfaces with high field enhancement capability are of broad research interests and have successfully been demonstrated for several frontline applications including nonlinear optics[37–39], photo-chemistry[40], surface enhanced Raman scattering[41–47], optical force nanomanipulation[48,49], photovoltaics[50–53], wave mixing[54], chemical and bio-sensing[55–57], nanolasing[58] and quantum information technology[59]. One popular and cost-effective approach of fabricating these substrates is deposition of plasmonic nanoparticles synthesized via chemical method[60] or surface roughing of metallic substrate[61]. However, hot spots with large field enhancements are randomly distributed and with limited methods to control[62]. Reproducibility of the fabricated nanostructures and uniformity of field enhancement are huge challenges for bottom-up methods which need urgent attention. Controlled engineering of plasmonic hot spots via top-down methods is a complementary strategy and often relies on photo/electron beam lithography or focused ion beam milling[63], in which high cost and low yield are preventing these technologies to be adopted for large scale applications. Several nanolithography and nanopatterning techniques

have been developed to address such concerns. For example, soft lithography has been successfully been utilized to print micro-/nano-sized three-dimensional and curved structures with a PDMS mold.[64] However, difficulties in structural dimension control at nanoscale, lateral collapse and sagging of the polymer prevent this method from fabrication of large scale highly efficient devices. Mold assisted fabrication method such as template stripping[65–68] is able to fabricate structures with large field confinement, yet roll-to-roll capability is not achievable and extensive time consumption to manufacture still remains a cause of concern. Innovative precision nanomanufacturing technologies need to be developed, in order to fabricate engineered plasmonic nanostructures, at low cost and in scalable manner.

2.3 Integrated graphene-plasmonic hybrid system

Graphene, a unique ultra-thin, ultra-strong two-dimensional crystal from an earth-abundant element, carbon, features with high carrier mobility, optical transparency, hydrophobicity, chemical inertness and property tunability. The research on graphene has boosted significant inroads in various disciplines including materials science, electronics, physics, mechanical, bio- and chemical engineering, directly or indirectly in a very brief span of time[69,70]. Graphene-based nanosystem would be the next exciting topic with integrated properties of graphene and functionality of the other components. Plasmonic nanostructures have the capability of collective oscillating free electrons at a metal-dielectric interface under the resonant excitation electromagnetic wave, and have already been demonstrated to significantly enhance performances of nanophotonic devices[71–73], imaging[74], sensing[75], energy conversion[76], and material manipulations[49]. Interactions of graphene and plasmonic materials have been under increasing interest in recent years[77]. Coating of graphene on the surface of these materials could therefore result in a new class of thermally and electrically conducting, optically transperant, chemically inert surfaces and thus one can design hybrid nanomaterials with tunable physical properties having potential to be utilized in a variety of applications. For example, enhanced photoemission from graphene covered ZnO films was observed due to transformation of resonant excitation of graphene plasmon into propagating photons through the interface[78]. Hybrid systems with graphene superimposed over metallic nanostructures were explored to have higher chemical-/bio-sensing capability due to its chemical enhancement effect, chemical

protection of metallic surfaces[79–82] and prevention of photocarbonization and photobleaching of target molecules[83,84]. Graphene coating on metallic nanowires was also reported to have increased thermal and electrical conductivity for better thermal management and higher speed in future electronic devices[85].

Strategies for integration of graphene with various nanomaterials include *in-situ* wrapping of graphene while nanostructures are being formed by chemical reactions[86–95] or post-growth *ex-situ* graphene wrapping of nanostructures[96,97]. Ex-situ graphene integration techniques[98–101], such as wet chemical transfer, are the most commonly employed approaches, due to their flexibility of transferring graphene deterministically onto various target surfaces with controlled graphene thickness and integrity. However, such transfer methods are incapable of conformal coating and most often give rise to wrinkles and gaps. It has been noticed that graphene is subject to both intrinsic microscopic corrugations[102] and extrinsic wrinkle instability[103–105]. Periodic ripples of suspended graphene are found to form spontaneously[106] and manipulation of the intrinsic ripple features of graphene is found to effectively influence optical and electronic properties by inducing an effective gauge field[107–110]. For graphene transferred onto a structured surface, the morphology of graphene is influenced by graphene-substrate interaction and it is quite distinct from the random intrinsic wrinkles of free-standing graphene. This extrinsic morphology, also referred to as snap-through instability of graphene[111,112], is crucial to fine tuning of physical properties of graphene and more importantly, the graphene-covered systems. Wrinkles and ripples of graphene could drastically influence the chemical activity of the system[113,114], result in reactive oxygen or sulfur species diffusion or reaction with substrate underneath[115,116], decrease charge transfer rate and block the accessibility of intense hot-spots beneath it.

2.4   Chapter Summary

In this chapter, the fundamentals of laser induced shock pressure is briefly discussed. The importance of metallic nanostructures and current fabrication techniques are reviewed, calling for novel cost-effective strategies with high resolution and high through-put. The needs for post-fabrication tuning of plasmonic antennas and shaping of brittle

semiconductor nanowires for strained electronics are also discussed, bringing opportunities for laser shock-based process design and innovation.

3. CHARACTERIZATION TECHNIQUES

3.1 Atomic Force Microscope (AFM)

AFM is a versatile high-resolution scanning probe microscopy which images surface morphology and many other local properties of a material. It operates by scanning a sharp tip attached to a cantilever across the specimen surface in contact, tapping, and noncontact modes. The resolution of the system is typically determined by the sharpness of the probe. The interaction between the tip and the sample surface is sensed as a function of tip-surface separation. The major abilities of AFM include imaging, force measurement, and nanomaterial manipulation.

In this research, Veeco Dimension 3100 system is employed for acquiring AFM images and line profiles under tapping mode. The probe used has tip height $15 - 20$ um and rip radius 8 nm mounted on Antimony (n) doped silicon rectangular cantilever, purchased from Bruker. The tip has a resonant frequency around 75 kHz, spring constant 3 N/m, and length 225 um. Three different channels including height, phase, and amplitude, are recorded for accurate measurements.

3.2 Raman Spectroscopy

Invented by Indian scientist Sir C. V. Raman[117], Raman spectroscopy has been widely used to observe low-frequency modes and provide fingerprints of molecules for identification. The shift in wavelength during inelastic scattering shows the chemical and structural information. Depending on the vibrational state of the target molecular, the shifted photons could have lower or higher energy, corresponding to the Stokes and anti-Stokes radiation. There have been many variations of Raman spectroscopy, such as coherent anti-Stokes Raman spectroscopy (CARS), for the purpose of sensitivity enhancement, spatial and spectral resolution improvements.

In this study, a micro-Raman Renishaw InVia Reflex system attached to a Leica microscope with 633 nm and 532 nm laser excitations is utilized to perform Raman

spectroscopy. A 600 or 1800 or 2400 grooves per millimeter grating is used for spectral analysis. In typical high spatial resolution measurements, the laser spot size is controlled to be around 1 μm with a 100X objective lens.

3.3 Scanning Electron Microscope (SEM)

As a type of electron microscope, SEM produces images by focusing and scanning a beam of electrons. The electron-sample interaction generates various signals, including secondary electrons, back-scattered electrons, transmitted electrons, and photons (cathodoluminescence), providing information about the sample's surface topography, composition, and properties. The resolution of SEM can be better than one nanometer, making it a powerful technique for material characterization at nanoscale. Energy Dispersive X-ray Spectroscopy and cathodoluminescence microscope are typically attached to the SEM system for elemental analysis and electron-induced luminescence.

In this research, the surface morphology was studied by FESEM (Hitachi S-4800 field-emission scanning electron microscope) or FEI Nova 200 Nano-Lab. Elemental composition of the samples are characterized by Energy Dispersive X-ray Spectroscopy at 10 KV or 30 KV, and EDS software AztecEnergy (Oxford Instrument). To reveal the cross-sectional information, in some cases the samples are tilted at 52 degrees and selectively etched by focused ion beam.

3.4 Nanoindentation

Indentation has been commonly applied in research labs and industry for effective and efficient measurements of material mechanical properties. A diamond-like hard tip is pressed against the target sample surface, which generates permanent micro and nano features on the surface. Nanoindentation monitors the load-displacement curves with high resolution which can be used for interpretation of mechanical properties.

A Keysight Nano-Indenter G200 with a standard Berkovich diamond indenter is used in this research. Several loading/unloading cycles are applied to evaluate thickness-dependent

properties. The loading time and the hold period at maximum displacement were 10 s and 2 s, respectively. The hardness and elastic modulus are obtained from the measured force-displacement curves[118].

3.5 Dark-field microscopy

Dark-field microscopy utilizes an illumination technique which excludes the collection of unscattered beam. It uses a specially designed opaque disc to block some light from the light source so that only scattered light can reach the objective[119]. The elastically scattered light results from electric polarizability of the nanoparticles.

In this research, the Raleigh scattering spectra are obtained using a home-built hyperspectral dark-field microscope. A dark-field condenser with numerical aperture (NA) 1.2–1.4 is coupled with a tungsten halogen source (Illumination technologies Inc.) via a fiber-optic light guide to minimize the thermal fluctuation of the light intensity for accurate measurements. The scattered light is collected using a 100× oil-immersion objective with an iris, and then split into two light paths, one for real-time optical dark-field imaging and the other for hyperspectral measurement.

3.6 Device fabrication and Electrical Property Measurement

The micro/nano-materials for electric devices can be transferred by a variety of methods, as shown in Figure 3.1. Several transfer techniques including additive transfer, subtractive transfer, and deterministic assembly are used for effective transfer, depending on the adhesion and fracture mechanics at the ink-donor, stamp-ink, and ink-receiver interfaces. After that, standard photolithography and E-beam lithography processes are utilized for device fabrication: the sample is first spin-coated with photo-resist, and exposed with light or electron beam; then the exposed polymer is dissolved with appropriate developer; finally, metallization and lift-off are carried out.
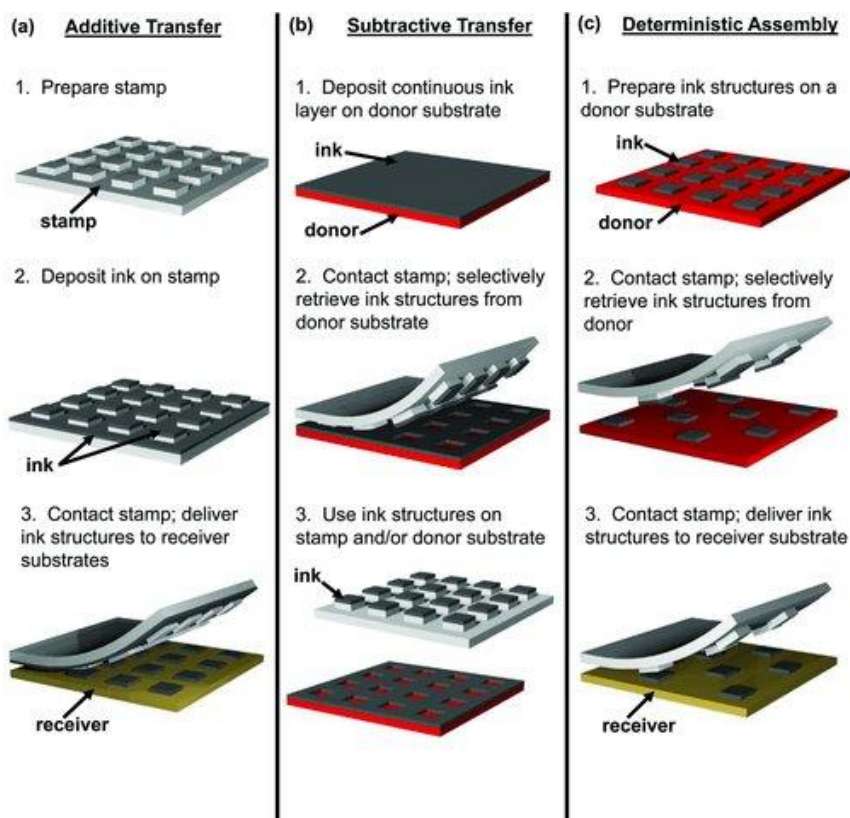
3.1 Transfer Techniques for device Fabrication.[120]

In this research, the nanomaterials are transfer printed with the aid of PDMS stamp or by contact sliding. Raith E-line E-beam system and Vistec VB6 system are adopted for pattern exposure. PMMA A4 is spin-coated on the sample surface. Moderate plasma etching or chemical etching is used during the fabrication process. The electrical properties are measured with HP4156 parameter analyzer.

3.7   Chapter Summary

In this chapter, the material characterization systems, including AFM, Raman spectroscopy, SEM, nanoindentation, dark-field spectroscopy, and electrical device fabrication and measurements are briefly reviewed and summarized.

4. LASER SHOCK NANOIMPRINTING OF METALLIC NANOSTRUCTURES

4.1 Introduction

Metallic nanostructures have found to be capable of harnessing collective oscillations of free electrons at the dielectric-metal interfaces when excited with light, and have been widely explored in nanophotonic devices and circuits[71–73], energy conversion devices[76,121–124], Surface enhanced Raman scattering[125–127], enhanced fluorescence[128–131], photothermal therapy[132–135], nano-particle manipulation by optical force[48,49,136,137], and metamaterials[138–140]. While fundamental and theoretical studies in these areas continue to bloom, large-scale practical implementation in industry has been greatly limited because of the high cost and low throughput inherited in current fabrication techniques. Fabrication of plasmonic nanocavity arrays through optical/electron beam lithography with subsequent metal evaporation and lift-off is intrinsically complex. The multi-step process traditionally used in industry and most research groups is highly sensitive to ambient conditions and high standard cleanrooms are generally required, which comes along with significant capital and energy investment. The fabricated nanostructures, on the other hand, suffer from multi-crystallinity, which introduces scattering and damping of surface plasmons[141]. Grain boundaries and large surface roughness often act as primary reasons of losses in polycrystalline materials and would diminish the plasmon propagation length and thus adversely impact the potential applications of such plasmonic nanostructures[142]. To this end, new fabrication techniques accompanied with good quality in controllable and efficient way need to developed. Considering the cost of commonly used materials today, aluminum could be a good candidate to replace silver and gold as a plasmonic materials in various applications if the performance of aluminum was tolerable and the fabrication cost is low.

In this section, we explore developing a new low-cost and energy efficient process, called laser shock nanoimprinting[143–145], which can produce ultrasmooth crystalline nanostructures instantaneously at ambient conditions. Different Al plasmonic nanocavity arrays, such as trenches and grids with various dimensions and good precision are

successfully generated by utilization of this technique. Nano-crystalline thin films fabricated by physical vapor deposition are also shock imprinted into structures with 10-nm resolution.

4.2   Technical Approach

4.2.1   Laser shock set-up

Q-switch Nd-YAG laser (Continuum® Surelite III) was used to ablate carbon coating (Asbury Carbons, U.S.A.) on thin metal foil (Al, 4 μm thick) (Lebow Company USA). The wavelength of the laser was 1064 nm with pulse duration 5 ns. The produced ionized plasma expansion was delayed and intensified through a glass confinement to generate ultra-high momentum for nanoimprinting. Another aluminum foil with 2.5 μm thickness (Lebow Company USA), cleaned successively with toluene, acetone, and Isopropyl alcohol, was placed between the sacrificial metal foil and a mold. In this study, silicon substrates (600 μm thick) were coated with HSQ photo-resist, exposed with VB6 Ebeam lithography, developed in TMAH, and plasma etched to desired depth. The imprinting set-up was placed on top of a motorized stage to enable in-plane scanning when total imprinting area was larger than the spot size used. Laser pulse energy and defocusing distance are adjusted to control the intensity of shock wave. It is noted that while excessive shock wave might decrease the life-time of silicon mold and thus decrease its repeatability, inadequate shock wave momentum would result in incomplete imprinting. After laser shock nanoimprinting, the 2.5 μm aluminum foil got an inverted replica of the mold beneath and was peeled off followed by fixing to flat substrate for analysis. The whole imprinting process was finished within one minute. Figure 4.1 shows the experimental set-up for laser shock nanoimprinting of aluminum.
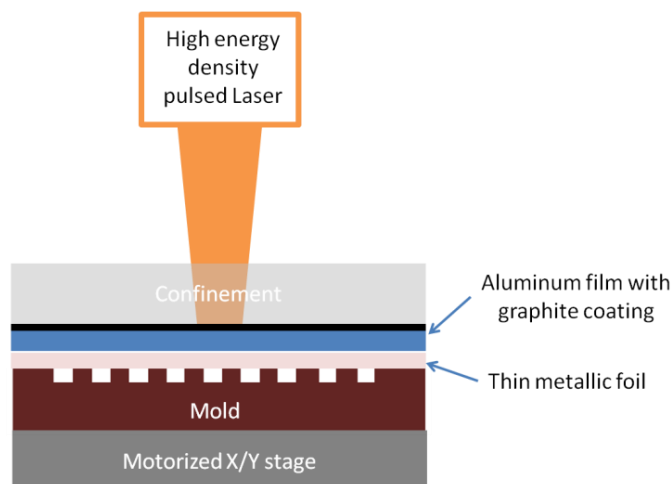
4.1 Schematic drawing of laser manufacturing of plasmonic nanostructures.

4.2.2 Graphene transfer

Single layer graphene grown on copper by Chemical vapor deposition (CVD) (Graphene Supermarket, Inc.) was spin-coated with PMMA A4 at 4000 rpm for 1 minute, followed by baking at 180 ^{0}C for 2 minutes. Underlying copper substrate was completely etched with aquatic iron nitrate solution. PMMA supported graphene was then washed with DI water and transferred on top of the laser shock nanoimprinted nanostructures. The sample was placed overnight to dry naturally before washing PMMA with acetone and cleaning with IPA.

4.2.3 Optical characterizations

The Raman spectra of graphene were recorded with a Renishaw inVia Raman spectroscope with 50 × objective (numerical aperture 0.75). The grating used for spectral analysis was with 1200 lines per mm. Laser excitation wavelength was 633nm from a He-Ne laser. Laser spot size was kept 2 μm during the measurement.

The local field of fabricated aluminum nanostructures was detected by a home-made Scattering near-field scanning optical microscopy (s-NSOM) in reflection mode. The exitation source was a Helium-Neon laser with 633 nm wavelength. The laser beam was focused on the s-NSOM tip by an objective (numerical aperture 0.42) mounted on a three-axis piezo scanner.The polarization direction was controlled to be perpendicular to the trench through a 1/2 waveplate.

Aquatic Rhodamine 6G (R6G) solution (50 µM) was dipped onto laser shock nanoimprinted aluminum structures. Photoluminescence of the molecules were observed using a confocal microscopy (Inverted LSM 710; Zeiss) through a coverslip with an air 20 X objective (numerical aperture 0.8) and laser excitation at 488 nm in reflection mode. R6G molecules of known concentrations were spin-coated on graphene veiled patterned plasmonic nanostructures and the samples were then dried up. Raman spectroscopy and photoluminescence spectroscopy and imaging were exploited for molecular detection. Raman spectroscopy was conducted using a micro-Raman Renishaw InVia Reflex system attached to a Leica microscope with 633 nm laser excitation and spot size 5 µm. Photoluminescence spectroscopy of R6G molecules anchored on graphene veiled plasmonic nanostructures with measured concentrations of molecules were recorded. Emission images of molecules lying on graphene veiled gold nanopyramids were also captured at different excitation wavelengths.

4.2.4   Numercial simulations

A finite-difference time-domain (FDTD) simulation technique has been employed for plasmonic modeling for a few geometries to validate experimental findings. The influence of graphene veil to laser shock nanoimprinted patterned plasmonic structures could be incorporated in the calculations of local field. Considering graphene to be infinitesimally thin two-dimensional material, the in-plane optical conductivity is a function of angular frequency, absolute temperature, Fermi energy and scattering rate. [146,147]

$$\sigma(\omega) = \frac{2ie^2 k_B T}{\pi\hbar^2(\omega + i\tau^{-1})} \ln\left[2\cosh\left(\frac{E_f}{2k_B T}\right)\right]$$
$$+ \frac{e^2}{4\hbar}\left\{\frac{1}{2} + \frac{1}{\pi}\arctan\left(\frac{\hbar\omega - 2E_f}{2k_B T}\right) - \frac{i}{2\pi}\ln\left[\frac{(\hbar\omega + 2E_f)^2}{(\hbar\omega - 2E_f)^2 + (2k_B T)^2}\right]\right\}$$

Eq. 4.1

where e is the elementary electronic charge, ω is angular frequency, k_B is the Boltzmann's constant, T is temperature, $\hbar$ is the reduced Planck constant, τ is carrier relaxation lifetime and characterizes electron-disorder scattering processes. In-plane electric permittivity is then given by,

$$\varepsilon_{eff} = 1 + i\sigma / (\varepsilon_0 \omega t)$$

Eq. 4.2

where t=0.5 nm, ε_0 vacuum permittivity.

Out-of-plane refractive index electric permittivity is,

$$\varepsilon_{eff} = 2.5 \qquad \qquad \text{Eq. 4.3}$$

Finite-difference time-domain (FDTD) simulation was employed to calculate local field under incoming laser source to validate experimental findings. Auto non-uniform meshing was applied (mesh accuracy 2) and the maximum mesh step was chosen to be 1 nm. Perfectly matched layer (PML) boundary condition was assigned to the maximum z-direction, and Bloch boundary was applied for x and y directions. Two dimensional Spatial harmonic analysis (SHA) technique was used to calcualte the reflectance spectrum of various aluminum structures. The step wavelength to be less than 3 nm. Transverse magnetic (TM) modes are choose for the perpendicular incidence wave. Molecular dynamics simulation of laser shock imprinting of aluminum film is taken out by using the open source MD package Lammps[148]. Aluminum is assumed to be single crystalline with FCC lattice (lattice constant 4.05 Å). EAM potential is used for Al and Lenard-Jones (LJ) potential is used for the interaction between silicon mold and aluminum. A constant velocity (100 m/s) of the mold is applied to aluminum, which corresponds to a strain rate 3~4 orders higher than the experiment, because of limited simulation resources. The atomistic data is post-processed by using the open visualization tool (OVITO).[149]

4.3   Results and Discussions

4.3.1   Nanoarrays on metal thin films

High energy density pulsed laser was used in this process. The ultra-fast nature of this process could enable roll-to-roll manufacturing. The aluminum replica nanostructures of silicon mold features were successfully obtained after the process. Figure 4.2 demonstrates the ordered aluminum nanostructures at sub-100 nm scale. The gaps of nano-trenches could be readily fabricated at 10-nm resolution. It should be noted that the starting material was cheap commercial aluminum film, while imprinted structures were quite tunable and with high quality. This would result in significantly reduced manufacturing costs and increased through-put in the field of plasmonic nanostructures fabrication.
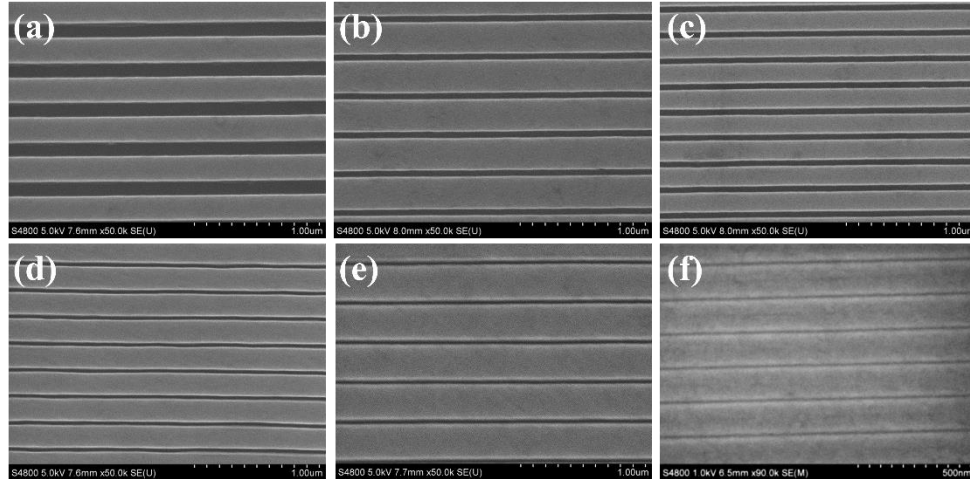
4.2 SEM of images of fabricated ultrasmooth nanotrenches.
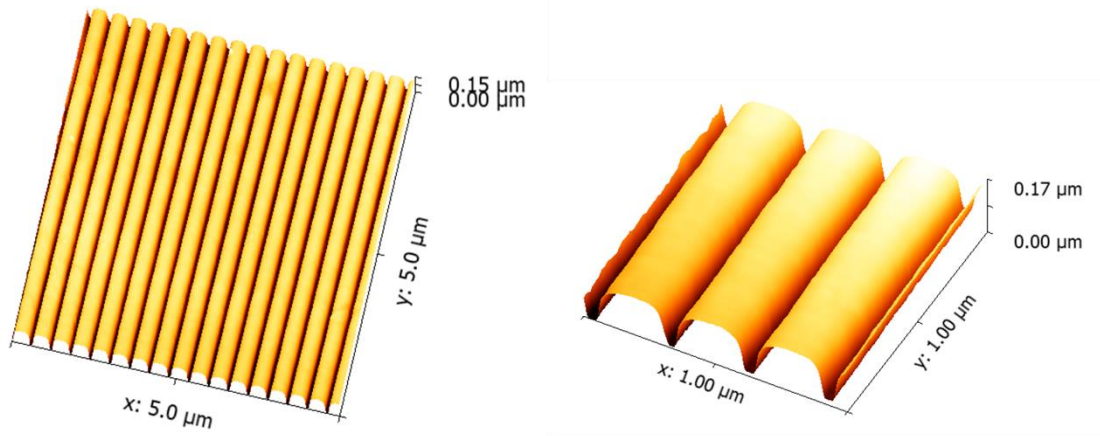
4.3 AFM images showing atomically smooth 100nm channel.

Figure 4.3 shows AFM images of fabricated ultra-smooth aluminum nanoarrays. The observed surface roughness of shocked aluminum is below 1 nm, demonstrating its atomic smoothness. This is benefited from the extreme condition experienced by the aluminum surface, and the surface smoothness of the EBL defined silicon nanomold. The detailed deformation mechanism will be discussed in the next section.
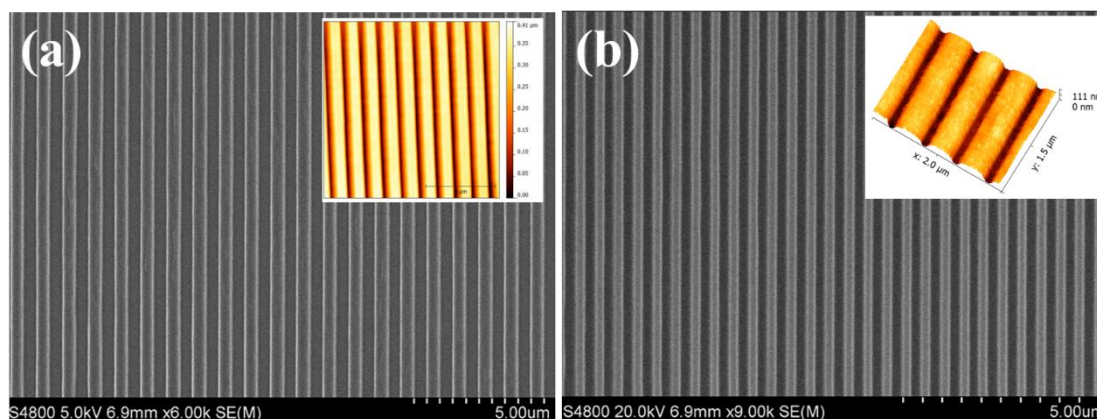
4.4 SEM and AFM images (inserted) showing ultrasmooth nanoforming of Titanium thin film by LSI.

LSI is also a suitable technique to pattern hard metals, such as Ti with a melting temperature of 1668°C and a Vicker's hardness 5 times that of aluminum. The ultrasmooth nanostructures fabricated on the surface of a 2.5-mm-thick layer of Ti (Figure 4.4) demonstrate its good formability using LSI.

4.3.2 Deformation of multilayered metallic thin films
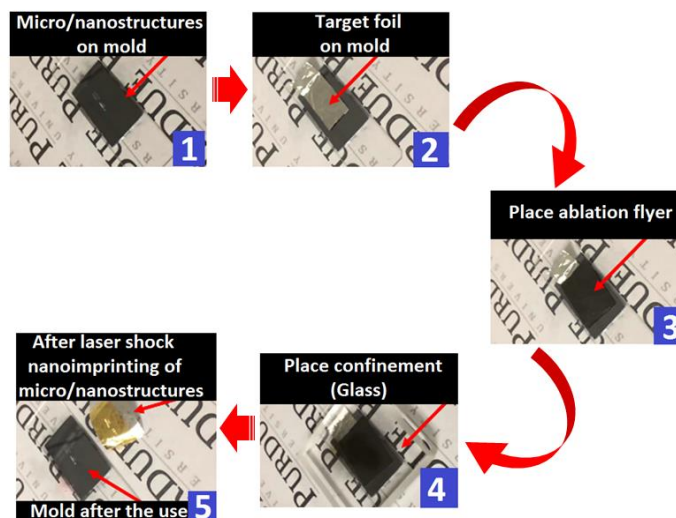
4.5 Successive steps for LSI fabrication of multilayered gold plasmonic nanoarrays.

The fabrication of multilayered nanoarrays provides greater flexibility for tunable properties. The procedures for this purpose (shown in Figure 4.5) are as follows: (1) Fabricate silicon mold; (2) Place target aluminum foil supported gold coating against the

predefined mold; (3) Place graphite flyer on top; (4) Place glass confinement to hold the whole set-up compact; (5) Separate the fabricated sample from mold for reuse.
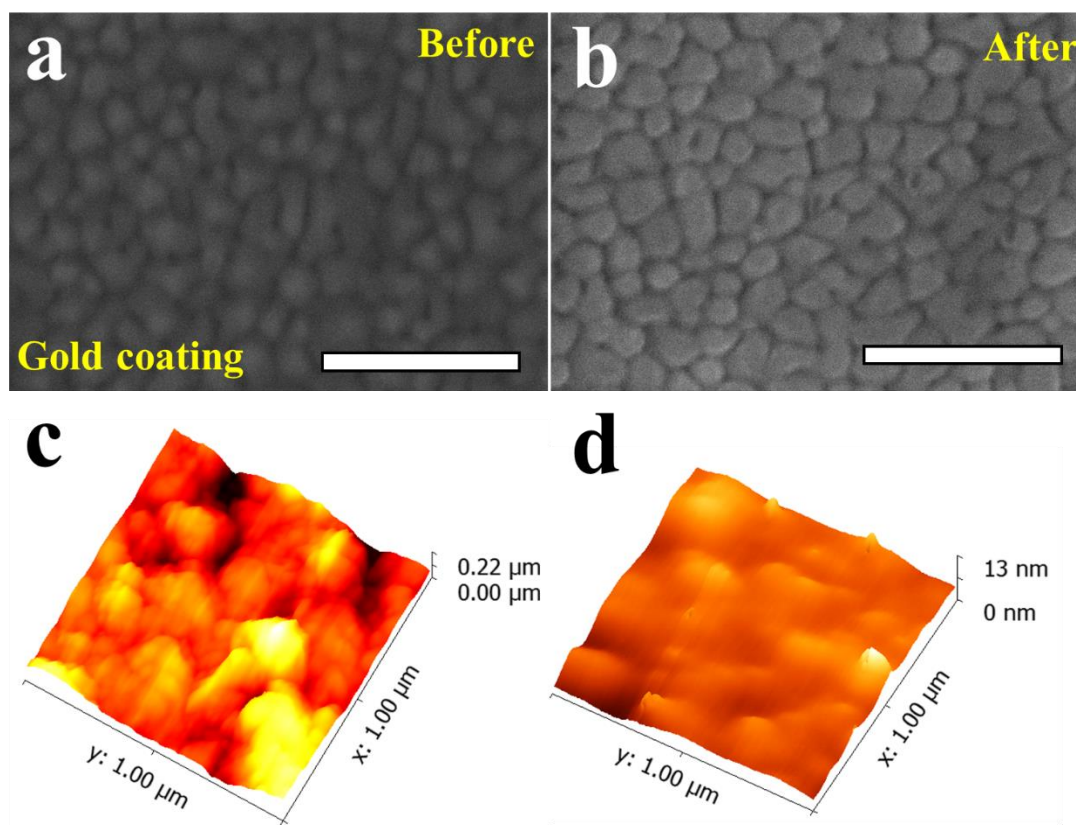
4.6 FESEM and AFM images of gold coating at flat areas before (a, c) and after (b, d) laser shock. Scale bar: 300 nm.

The typical grains size of vapor-deposited thin film is about 50 nm, which impedes fabricating structures with comparable size, serves as intrinsic surface roughness and introduces scattering or damping of surface plasmons.[142] For laser shock imprinting of aluminum nanostructures, the aluminum surface is pushed against a silicon mold which is atomically flat. Various surface variations could be flattened during this process and thus it yields ultra-flat surfaces.

Figure 4.6 shows high-resolution SEM images of the gold coating before and after laser shock process at the flat areas respectively. Slight grain size change could be oberved due to shock induced compression. The corresponding AFM imaging of the surface morphology demonstrates the significantly reduced surface roughness. Figure 4.7 shows

the effect of ultra-thin titanium layer in this process. If the plasmonic material is coated on the substrate without an adhesion layer, the fabricated patterns could be easily peeled off from the substrate during seperation of the patterned film from mold, due to comparable adhesions between plasmonic coating-substrate interaction and plasmonic coating-mold interaction. With the help of Ti, plasmonic coating-substrate adhesion is considerably increased and thus well defined structures are fabricated on the film.
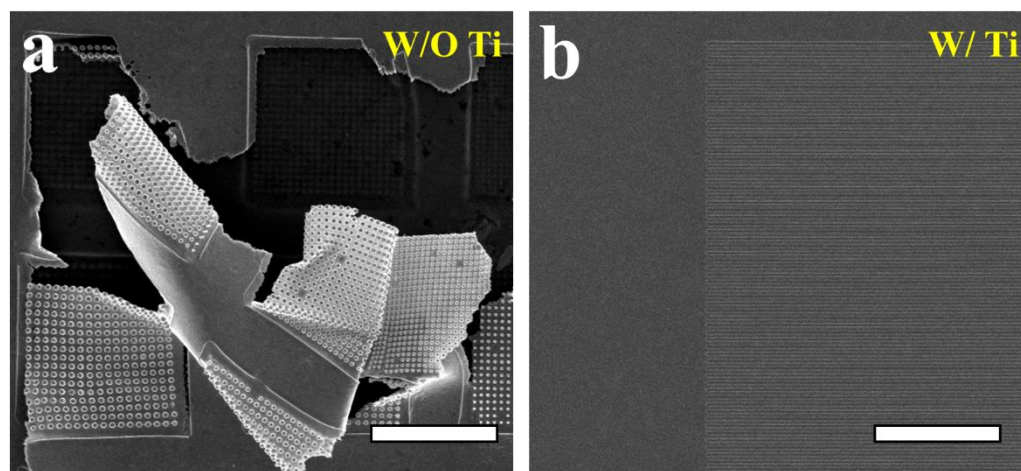
4.7 LSI of Ag coated aluminum foil without (a) and with (b) Ti (5 nm) adhesion layer. Scale bars: 5 μm.
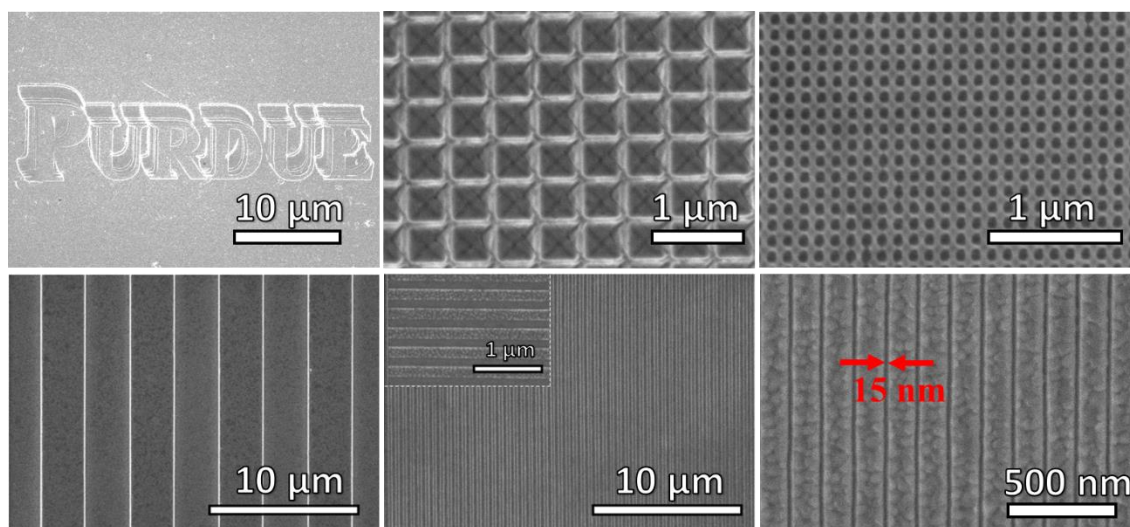
4.8 SEM surface morphology imaging of obtained multilayered nanoarrays. Inserted is higher resolution SEM image of nanostructure.

Micro- and nanometer scale gold patterns are fabricated precisely and reproducibly, as shown in the FESEM images in Figure 4.8. The present LSI technique is equipped with the

capability of precision nanoscale imprinting of functional nanostructures on flexible substrates in scalable and reproducible manner. Structures including but not limited to trenches, circles, and holes with dimensions as low as 20 nm have been obtained on the hybrid film by a single laser shock. Deposition of a layer of Au on thin flexible substrate generally results in much rougher surfaces, because of thermal stress and deformation associated with rapid non-uniform heating and cooling effect during the deposition process, large initial roughness of the supporting substrate, and wrinkles generated during sample cleaning and handling.

4.3.3 Deformation mechanics
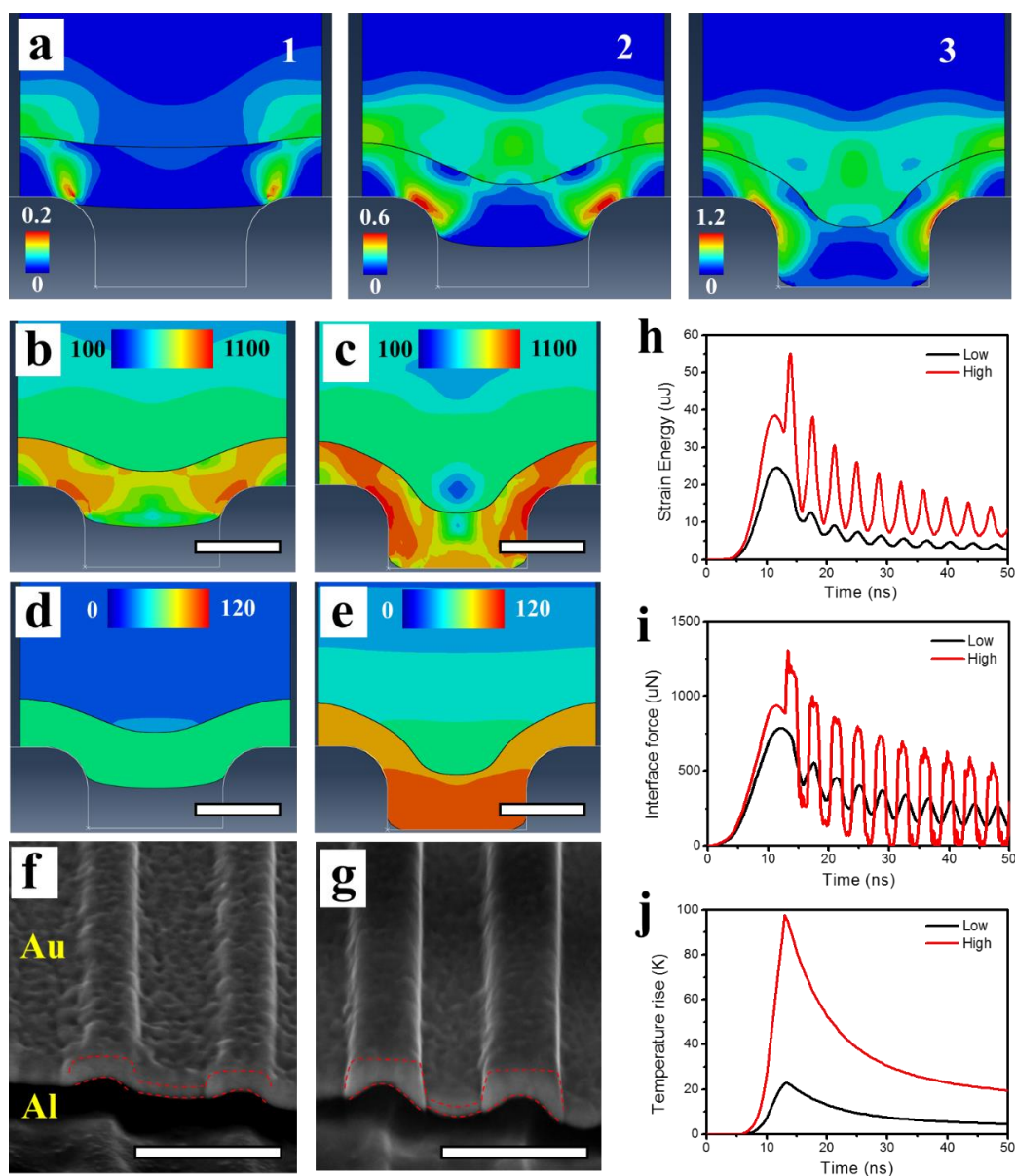
4.9 (a) Schematic of plastic strain generation during laser shock imprinting of hybrid films with different mechanical properties: (1) initialization of plastic flow, (2) developed stage, (3) final stage. (b-e) Calculated von Mises stress fields (unit: MPa) (b-c) and temperature fields (unit: K) (d-e) for laser intensities of 0.27 GW/cm^2 (b, d) and 0.48 GW/cm^2 (c, e), respectively. (f-g) Corresponding FESEM images of obtained cross-sections. Scale bars: (a-e) 300 nm, (f-g) 1μm. (h) Strain Energy history of the system. (i) Corresponding contact force at gold coating and aluminum film interface. (j) Temperature rise and dissipation due to high strain rate deformation and thermal transport.

Impulse imparted by shock waves raises momentum of metal thin film to a level which suffices for the 3D plastic deformation conformal to the micro/nano scale molds. Metals under extreme laser shock pressure, achieves excellent 3D micro/nano forming due to high strain rate exceeding 10^6 s^{-1}. Ultrafast laser based 3D micro/nano forming results in compactness in formed materials which strengthens them. Since strain rate varies over huge range within minute fraction of second, plastic strain σ would have significant strain rate dependence. Considering that Johnson-Cook (J-C) strain sensitive plasticity model applies to the present case, the slope of the flow stress curve is independently influenced by strain, dimensionless strain rate and local temperature achieved in constriction.

$$\sigma = (A + B\varepsilon^n)\left(1 + C\ln\frac{\dot{\varepsilon}}{\dot{\varepsilon}_0}\right)(1 - T^{*m}) \qquad \text{Eq. 4.4}$$

where ε is the plastic strain, $\dot{\varepsilon}$ is plastic strain rate, $\dot{\varepsilon}_0$ is the reference strain rate. A, B, and C are material constants. T^* is the homologous temperature defined by,

$$T^* = \frac{T - T_r}{T_m - T_r} \qquad \text{Eq. 4.5}$$

4.1 Mechanical and thermal properties of aluminum and gold. [150,151]

	Al	Au
Density (g/cm^3)	2.7	19.3
Young's modulus (GPa)	36	79
Poisson ratio	0.33	0.42
Thermal conductivity (Wm^{-1}K^{-1})	237	318
Specific heat capacity (J/g^{o}C)	0.90	0.16
Coefficient of thermal expansion (K^{-1})	14.2 x 10^{-6}	23.1 x 10^{-6}
Melting temperature (^{o}C)	660	1064

Temperature rise during the high strain rate process is considered by setting inelastic heat fraction for plastic flow. The temperature dependence of yield stress is set to zero, as it was found that yield stress of gold does not vary with temperature at low temperature region.[152] Two different sets of thermal and mechanical properties are assigned to represent the deposited polycrystalline Au layer and aluminum. The material properties are shown in

Table 4.1. ABAQUS software has been used to numerically simulate the stress as well as temperature fields during the process.

Figure 4.9 (a) shows the successive stages of hybrid film deformation under shock pressure. At abrupt geometrical changes, materials are subjected to severe strain fields due to stress concentration. For different laser conditions, the calculated von Mises stress fields and cross sections are different, as shown in Figure 4.9 (b, c). Stress field in gold coating is generally larger than that in aluminum because of its stronger strain-rate sensitivity (Table 4.2). At the upper corner of the mold, Au layer directly bears the reaction force from the mold and flows into the trench. The thickness of Au layer inside the trench is thus anticipated to be thicker than that outside (Figure 4.9 (c, e, g)). Depending on the stage of the deformation and laser intensity, Au layer can suspend on the trench (Figure 4.9 (b, d, f)) for low laser shock pressure, or touch the bottom (Figure 4.9 (c, e, g)) for high laser shock pressure. The gold layer under high shock pressure is punched against ultra-flat silicon mold, thus generating a replicated smooth surface. The simulated results in Figure 4-9 (b-e) qualitatively agree well with those from experiments (Figure 4.9 (f-g)).

4.2 Parameters for Johnson-Cook plastic model [151–153] for Al and Au with average grain size around 80 nm.

	A (MPa)	B (MPa)	C	n	T_r (^0C)	m
Al	140	157	0.016	0.167	527	1.7
Au	120	243	0.056	0.147	23	0

Figure 4.9 (h) shows the strain energy of the hybrid during and after laser shock loading. While the pulse duration is only around 5 ns, the first peak in strain energy is found to occur several nanosecond later than the peak in laser intensity, resulted from the prolonged plasma-induced shock pressure due to confining media and a time delay for elastic and plastic stress wave propagation. The second peak, which is more obviously present in the case of high laser intensity, emerges when the film impacts on the bottom of the mold and kinetic energy of the material transfers into strain energy of the system. Similar phenomena are found for the interface force (Figure 4.9 (i)). The strain energy, interface force and local temperature rise (Figure 4.9 (j)) are found to decay as plastic stress wave propagates and reflects. The maximum temperature rise is around 100 K and 20 K for laser intensity of

0.48 GW/cm^2 and 0.27 GW/cm^2, respectively. Thermal energy is uniform inside the thin gold layer and dissipates quickly due to the high thermal conductivities of the metals. Depending on the material properties, maximum temperature which locally rises in the ultra-high strain rate deforming process could be increased, due to competing effects of heat generation and dissipation. It should be noted that accurate material properties and processing parameters are often difficult to obtain, especially in the present case of non-equilibrium plasma shock induced micro/nanoscale high-strain-rate deformation. However, the calculated results shown in Figure 4.9 could be interpreted qualitatively and serve as estimations of temperature rise and deformation profile.
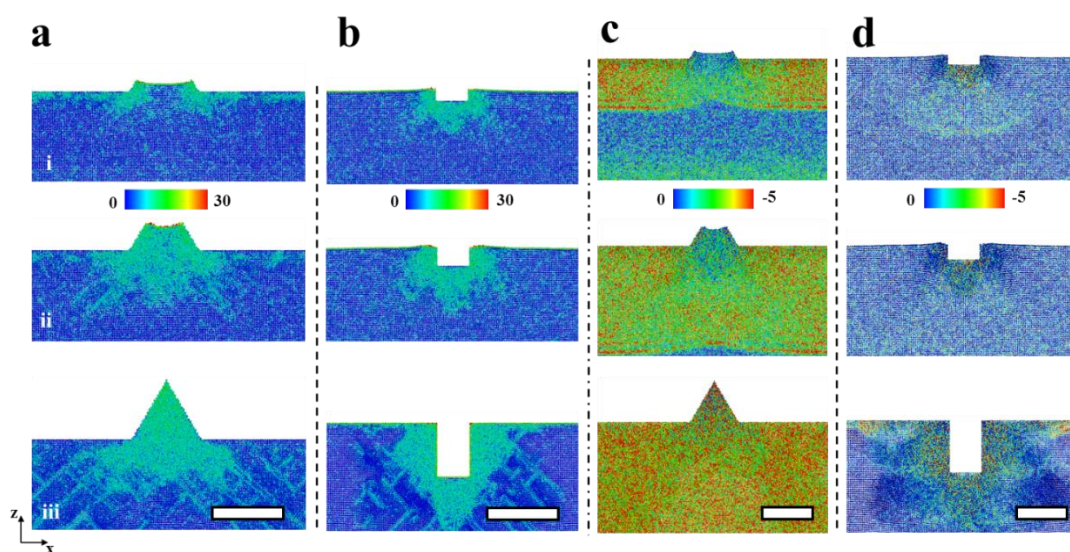
4.10 (a-b) Centrosymmetry parameter plots during molecular dynamics simulation of nanotip (a) and nanotrench (b) formation at the initiation stage (i), developing stage (ii), and final stage (iii). (c-d) Corresponding stress fields (Mbar) along z-direction for nanotip (c) and nanostrench (d). Scar bars (a-d): 8 nm.

Here the mechanism to imprint ultrasmooth 10-nm nanostructure from PVD deposited nanocrystalline thin film are investigated in atomic scale. Although the typical grain size of pre-deposited gold or silver coating is around 50 nm and the surface is rough after E-beam evaporation, the fabricated structures after LSI are within a few nanometers precision. The structures are normally difficult to obtain in large area for other techniques such as electron-beam lithography, due to the low throughput and also self-shadowing effect[154] during metal evaporation, as well as other metal imprinting process, due to the high temperature induced roughness and limited formability at low strain rates. Herein, the

nanocrystalline thin film after physical vapor deposition process, such as E-beam evaporation, could be easily deformed into ultra-small patterns with high fidelity during a high-strain-rate process – LSI.

High strain rate induces high dislocation density and formation of nanocrystalline or subgrains. A full description and explanation of LSI technique in nano-deforming nanocrystalline multilayered film is complicated by the presence of various extreme conditions such as high hydrostatic pressure, highly localized large shear stress at sharp mold geometries due to stress concentration, ultra-high strain rate, local temperature rise due to mechanical-thermal energy conversion, and material flows in nanoscale. During the present ultrahigh-strain-rate processing (10^7 s^{-1}), especially at gaps or edges of the structures where severe stress fields exist, laser shock can be utilized to generate large shape changes at very small length scales. This enables laser shock to fabricate free-standing plasmonic nanoarrays with fast speed, high precision, and improved mechanical performance. Figure 4.10 (a-b) shows the contour plots of centrosymmetry parameter at different stages of the nanoshaping process. During high-strain-rate forming, dislocations are nucleated at mold geometrical sharp edges for both nanotips and nanotrenches. As shock wave propagates, the dislocation sources at those edges coalesce and form a united highly-disordered microstructure around mold geometries for subsequent recrystallization. It is found that forming nanotrenches requires much lower laser intensity than the case for the 2D or 3D nanotips (0.4 GW/cm^2 compared to 0.9 GW/cm^2), which qualitatively agrees with our MD simulations as shown in Figure 4.10 (c-d). Material pile-up against mold edges could be observed at this stage, because of plastic flow above the free surface. As the shaping process continues, the undesired pile-up impacts on the flat areas of the mold and is thus eliminated, resulting in high-fidelity feature transfer and crystalline nanostructures. Depending on the laser intensity used, material properties and geometrical dimensions, atomically smooth and single crystalline[155] nanostructures would be fabricated. Apart from its capabilities to fabricate smooth and crystalline nanoshapes, characteristics such as instantaneous single-step, ambient processing and low-cost, enable laser shock nanomanufacturing technique to outperform the existing technologies such as electron- or ion- beam fabrication[156,157], in fabricating plasmonic nanoarrays on free-standing substrates.

4.3.4 Optical properties
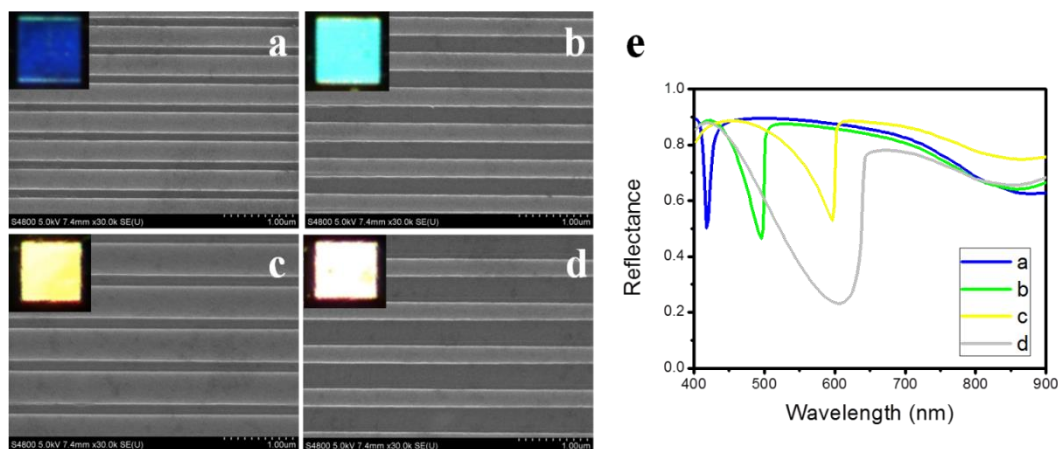
4.11 SEM pictures of fabricated Al gratings with different dimensions ((a) 100 nm gap with 400 nm period, (b)250 nm gap with 500 nm period, (c) 100 nm gap with 600 nm period and (d) 370 nm gap with 640 nm period). Insets show corresponding dark field images (20 μm× 20 μm) and (e) calculated reflectance.

Dark field images are recorded for different fabricated structures and their reflectances are calculated as shown in Figure 4.11. The step wavelength is less than 3 nm. Transverse magnetic (TM) modes are chosen for the perpendicular incidence wave. By changing structural period and gap distance, the resonance wavelength of the structure could be tuned. The color of dark field image is found to shift from blue to yellow when the period changes from 400 nm to 600 nm, keeping the gap distance unchanged (Figure 4.11 (a) and (c)). The calculated reflectance of the structure shows a shift of reflectance minimum from at 420 nm to 590 nm, which agrees well with the dark field images. Changing the period of the structure could also shift the resonance, as shown in Figure 4.11 (b) and (d). And the structure could be further tuned to behave as a perfect absorber at visible frequencies, which would have broad technological impacts in various fields such as optical metamaterials, energy harvesting devices, and photocatalysis.

4.3.5 Graphene-mediated surface enhanced Raman scattering

Various graphene-plasmonic nanostructures can be top-town fabricated on flexible substrate. Figure 4.12 shows the FESEM images for several nanoengineered plasmonic

arrays, including ultra-sharp 3D pyramids, V-groove (10 nm ridge), and nanotrenches (10 nm gap).

As shown in Figure 4.12 (a), after graphene is transferred onto the nano-pyramid with sharp tips, graphene foldings are formed between the tips. Graphene is subject to large mechanical straining[158], which would locally change its optical and electronic properties by introducing pseudo-magnetic fields and possibly opening an electronic bandgap[107–110]. In addition, rounded features on the tips can be observed as a result of the strain fields generated during graphene transferring onto 3D nanostructures. We found graphene could be smoothly transferred on nanogrooves and nanotrenches (Figure 4.12 b, c)) without strain induced breaking and folding. For nanogrooves with sharp tips, side illumination or non-symmetrical design is needed for manipulating the constructive plasmon interference[65,159] at the apex.
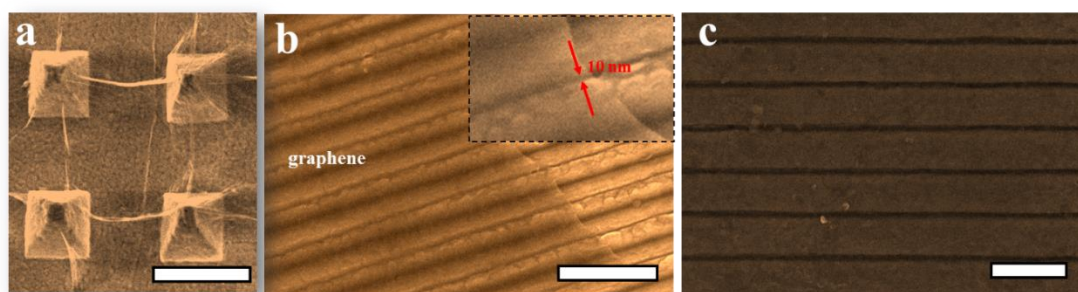
4.12 (a) FESEM image of graphene on patterned gold pyramid (3D nanotip) arrray fabricated by LSI. Scale bar: 1 µm. (b) FESEM image of graphene veiling on top of ~10 nm nanogrooves (2D nanotips) fabricated by LSI. Scale bar: 500 nm. (c) FESEM image of graphene veiling fabricated nanotrench. Scale bar: 500 nm.

Noticeable 2D peak enhancements are also observed for our microstructures, showing a positive correlation with trench frequency for large gaps (Figure 4.13 (a)) in which case there is no or weak local surface plasmon resonance coupling between the two sharp corners. As structural dimensions keep shrinking (gap distance much smaller than incident laser wavelength), near-field coupling and resonance of the structure under Raman laser excitation would result in further enhancements. By adjusting the gap distances, a more than 1000-fold 2D peak enhancement could be easily achieved (Figure 4.13 (b)). It should be noted that we also observed a decrease of the enhancement when the gap distance is below 100 nm (Figure 4.13 (c-d)). This is in accordance with resonance red-shifts with

gap distance shrinking[160]: when the resonance of the structure shifts away from the Raman laser, a decreased 2D peak enhancement is observed. Full exploitation of the structures requires careful design of the structural dimensions including the periods, depths and gap distances. These along with aforementioned spatial control and polarization effect would give rise to active control of light-matter interactions, as underlying nanoarrays enable ultrafast doping of graphene and dynamic tuning of its Fermi energy. In addition, graphene could serve as a thinnest conductive pathway to realize charge transfer plasmon[161] and resonance tunability.
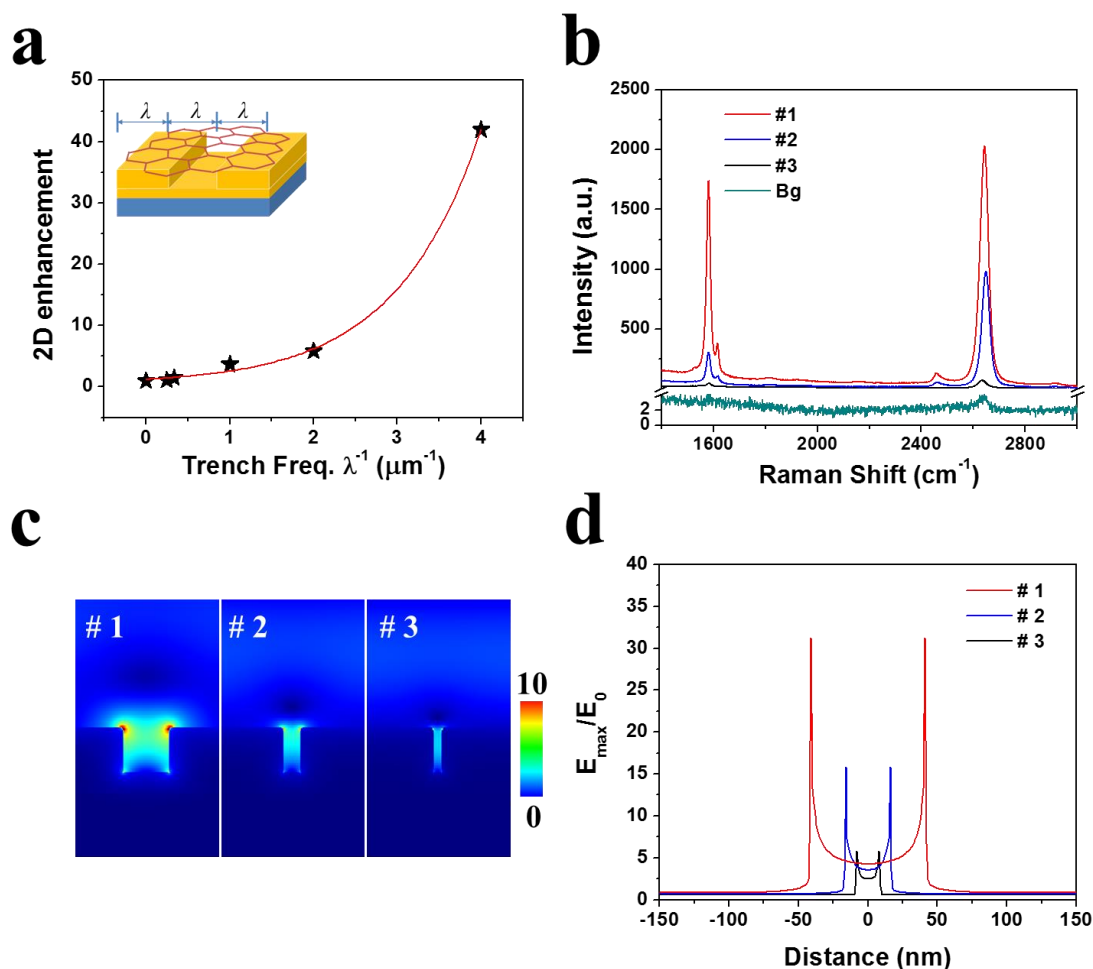
4.13 (a) 2D enhancements vs. trench frequency (μm⁻¹) plot. Inset: schematic of the structure. (b) Enhanced Raman scattering of graphene for different nanotrenches. (#1: 80 nm; #2: 30 nm; #3: 15 nm) under TM polarized excitation. (c) Calculated field enhancement at graphene surface. (d) Line profiles of the field enhancements at graphene surface.

The optical reflectance of the hybrid film is then studied by varying the number of graphene layers integrated. As shown in Figure 4.14 (a), with single layer graphene veiling on gold plasmonic nanostructures, a more than 20% enhanced light absorption at resonance wavelength is achieved. With increasing number of layers, resonance dips of the hybrid structure increasingly get broadened and shallowed, especially for graphene with more than five layers. This could be understood from the loss and dissipation of graphene. Veiling gold plasmonic nanostructures with multilayers of graphene would result in red-shift of resonance wavelength. As shown in Figure 4.14 (b), the red-shift with increasing graphene layers is 1.5 nm per layer.
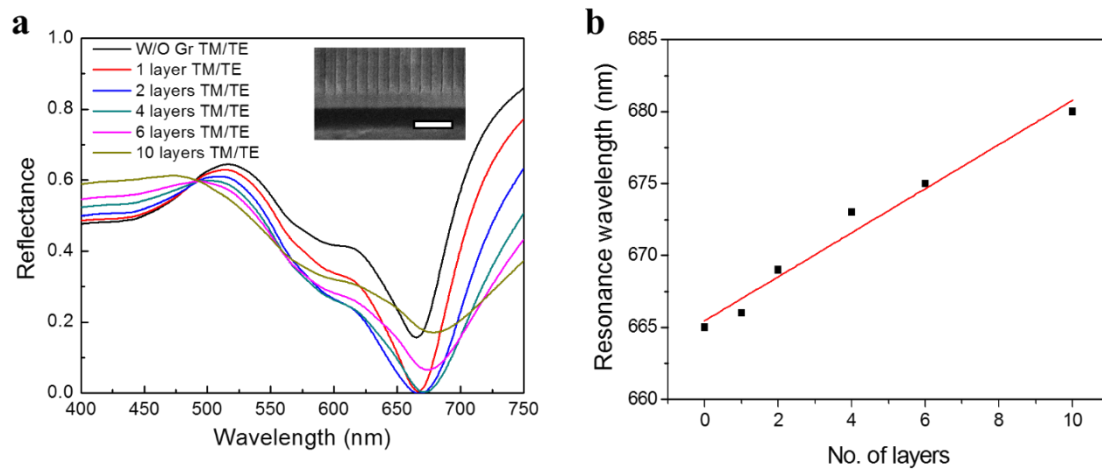
4.14 (a) Calculated optical reflectance of the graphene veiled hybrid film. Scale bar: 500 nm. (b) Resonance wavelength shifts with graphene thickness.

The enhancement of 2D peak of graphene is correlated to its optical power absorption at overlapped electric field[41,162]:

$$P_{abs}(\omega) = \frac{1}{2}\omega \int imag(\varepsilon)|E|^2(\omega)dV \qquad \text{Eq. 4.6}$$

where ω is angular frequency of incident light, E the electric field, ε the dielectric function. As the more than 1000-fold enhancement arises from 10 nm areas, according to Eq. 4.6, a more than 10^2 fold field enhancement (E_{max}/E_0) could be achieved for these ordered nanoarrays after incorporating near-field localization. Thus SERS intensity enhancement is calculated to be as high as 10^8 for these samples. The large enhancement achieved at 100 nm gap size is due to the sharp corners obtained by our technique. Compared with structures with rounded corners, sharp features could thus couple with tunable gaps, generating large field enhancements accompanied with more enhanced volume to benefit

applications such as SERS where molecules need to reach the hot spots to be probed. The hybrid nanosystem achieved in this paper thus provides degrees of control and tunability over excitation laser polarization, resonance frequencies, and spatial selectivity, and demonstrate its advantages in terms of predictability and reproducibility[162,163].

An open-air annealing test of the hybrid film at elevated temperatures (up to 300 ^{0}C) reveals its stability against oxidization and solid state dewetting of the thin silver layer, demonstrating its supreme performance even at harsh environments. In the case of silver, void formation and growth are observed at temperatures above 200 ^{0}C for bare nanostructures without graphene veiling, especially for silver coating with small thickness due to its small induction time for solid-state dewetting[164]. As shown in Figure 4.15 (a), the grain size increases from around 85 nm to 500 nm for bare samples. Such giant grain growth would result in substantial morphological damage to the structured areas and degradation to SERS performance (Figure 4.15 (e)). The driving force for this damage is free energy reduction in the ambient-film-substrate system, accompanied by oxygen species facilitated hole formation and subsequent hole growth by decreasing catchment area, enhancing surface diffusion, and lowering surface energy required to form hillocks[164]. Silver oxide nanoparticles are also observed to grow on the surface, which could become instable at high temperature and decompose. Similar thermal coarsening effect could also be anticipated for gold nanostructures[165]. Veiling graphene on top would effectively block direct contact of metallic surfaces with reactive species and catalytic agents (Figure 4.15 (c)). Besides that, suspended graphene could homogenize local non-equilibrium temperature distribution, benefited from its supreme thermal conductivity, and provide an additional ultra-thin surface for increased surface energy to initiate thermal instability. In contrast to the giant grain growth and surface oxidization, for graphene veiled samples the grain size remains at around 100 nm (Figure 4.15 (b)), and severely damages to metallic nanoarrays at elevated temperatures are inhibited by suspended graphene (Figure 4.15 (d)). As shown in Figure 4.15 (e), Raman intensities of graphene peaks for graphene veiled nanoarrays are found to be uniformly increased after heat treatment at 250 ^{0}C, which is in sharp contrast with the giant decrease for uncovered arrays. The increase could be understood from better crystallinity and void elimination which reduce scattering and

dephasing of surface plasmons[166]. The nanoarrays are also found to slightly decrease gap distance during annealing, which would result in higher field confinement and red-shifts of surface plasmon resonance, and give rise to unequally enhanced G and 2D peaks. Annealing at temperatures higher than 300 ^{0}C would introduce graphene oxidation. For that, other two-dimensional materials with higher temperature stability (such as boron nitride) could be veiled in a similar manner and is thus out of the scope of the present study.
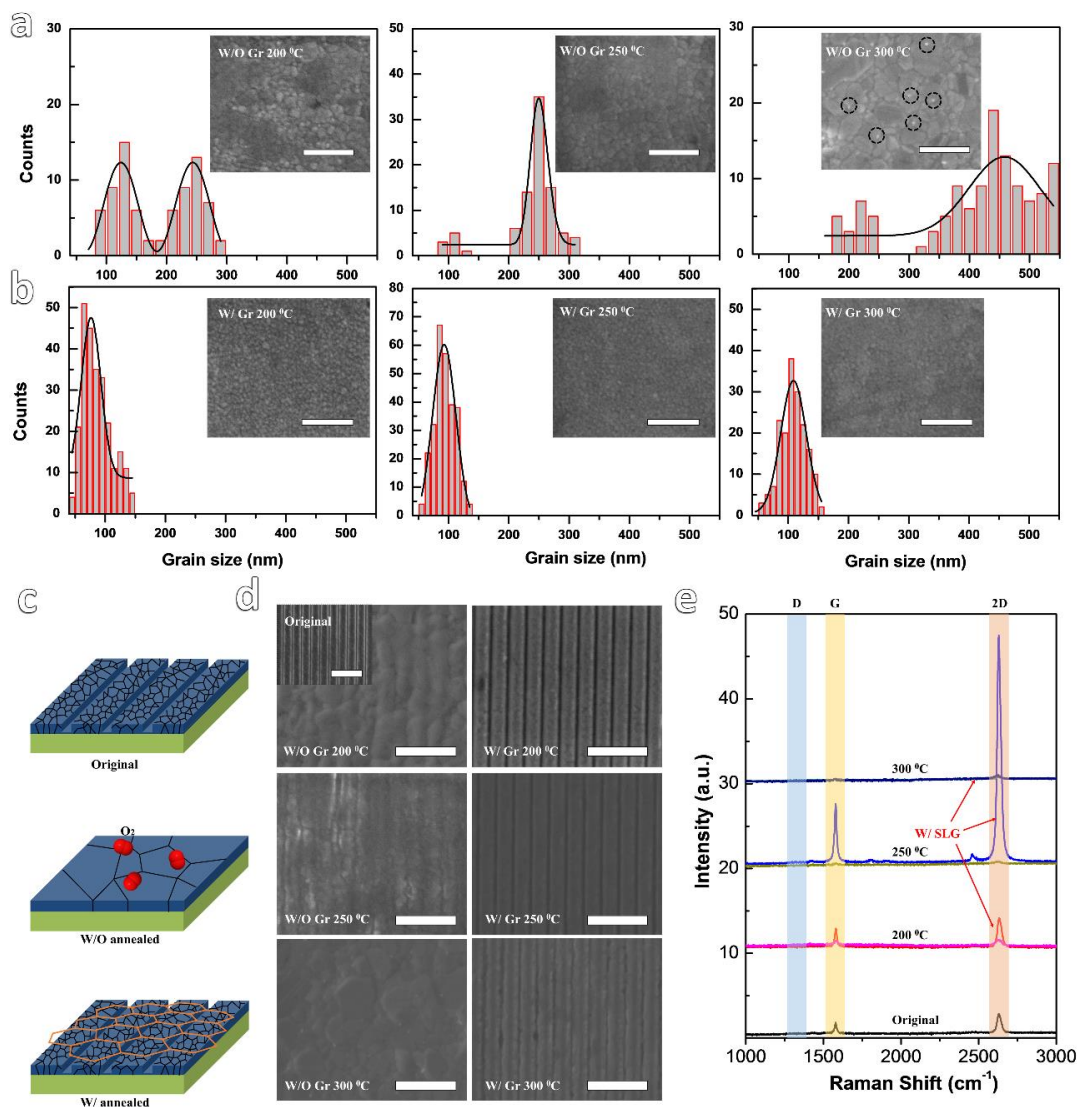
4.15 Graphene veiled hybrid system at elevated temperatures. (a-b) Histograms of grain size of free-standing silver coating (200 nm) on aluminum substrate without (a) and with (b) graphene veiling annealed in open air at 200 ^{0}C, 250 ^{0}C, 300 ^{0}C for 5 min respectively. Inserted are corresponding SEM images. The dashed black circles indicate silver oxide nanoparticles. Scale bars are 1 μm. (c) Schematics of stability of the hybrid film at elevated temperature annealing. (d) SEM images of morphology evolutions of the original, uncovered and SLG veiled plasmonic nanoarrays. Scale bars are 1 μm. (e) Raman spectra of SLG veiled silver plasmonic nanoarrays after different temperatures annealing.

To unfold one of the emerging applications of such hybrid nanosystem, we investigate its use as stabilized molecular sensing platform. The hybrid multilayer is employed as an anchor surface for R6G molecules (10^{-7} M level). Raman spectra, recorded on bare flat gold surface as well as flat areas covered with SLG do not show any characteristic Raman

fingerprints of the R6G molecules (Figure 4.16 (a)), due to the low concentration and off-resonance of the molecules under red laser excitation. In contrast, vibrational fingerprints of the molecules at 613, 775, 1187, 1360, 1509 and 1650 cm^{-1} are vividly apparent on LSI treated surfaces. Suspended graphene veiling over the imprinted nanoarrays provides additional enhancements, the magnitude of which depends on several competing effects. Firstly, adsorption or adhesion of organic molecules is generally stronger on graphene covered nanoarrays, due to their π- π interactions. Secondly, graphene as an ultra-thin two-dimensional material could provide additional enhancement due to Chemical Mechanism (CM) by facilitating charge transfer between plasmonic nanostructures and probe molecules, when Fermi level of graphene sits between the lowest unoccupied molecular orbital (LUMO) and highest occupied molecular orbital (HOMO) of the molecule. Thirdly, by resonance energy transfer, graphene could effective quench the fluorescence of the target molecules and the luminescence of the gold nanostructures[167], thus providing clearer background for sensitive detection. Fourthly, local electric fields could be changed due to suspended graphene coverage. However, suspended graphene as an impenetrable shield would also prevent molecular accessing tiny gap areas beneath. Due to these combined contributions, several folds of enhancements due to presence of graphene are typically observed.

The hybrid system with suspended graphene could stabilize the target molecules due to graphene surface passivation effect, superior thermal conductivity[168,169] and capabilities of preventing photo-induced damages such as photo-carbonization of the molecules and plasmonic welding[3] of metallic nanostructures. Figure 4.16 (b-e) shows time-dependent experiments to compare the stabilities of R6G on bare structures and suspended graphene veiled structures. For molecules on bare structures, with continuous laser excitation, molecules keep getting photo-damaged (with more than 60% Raman signal intensities decrease), even though the intensity of the incident Raman laser is kept low. This results from highly intense local electro-magnetic fields due to light trapping of the nanostructures. Such photo-induced damages at hot spots would pose major roadblock towards distinctive molecular recognition. However, when R6G molecules are placed on top of hybrid system with suspended graphene, its Raman signatures are significantly stronger and much more stable, as shown in Figure 4.16 (c). This signal stabilization effect for molecules in contact

with the graphene sheet is found to work excellently for R6G-graphene interactions. The signal enhancement of R6G signatures due to the presence of graphene is typically three times initially, and with repetitive Raman laser irradiation, it could increase up to ten times. Such evidences demonstrate the advantages of the hybrid film in molecular sensing and SERS applications.
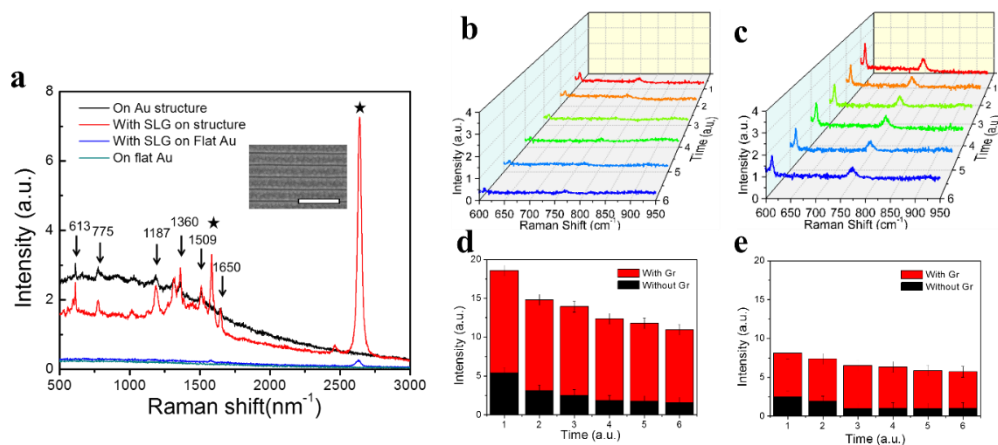
4.16 (a) SERS of R6G molecules on flat gold, patterned gold nanostructures, SLG veiled flat gold and SLG veiled patterned gold nanotrenches. Inset is SEM image of the structure. Scale bar: 500 nm. Repetitive recorded Raman spectra of R6G molecules on fabricated gold nanostructures before (b) and after graphene veiling (c). (d) Spectra intensities at 613 cm^{-1} for bare structure and with SLG coverage. (e) Spectra intensities at 775 cm^{-1}. Laser excitation wavelength is 633 nm.

The flexible free-standing hybrid film is further investigated as a thin sensor for real-time detection of trace-amount antibiotics from their waste containers. As a kind of seriously abused chemicals, antibiotics such as Norfloxacin (Nor) have been realized as most concerning pollutants because of the threat in triggering allergic reactions in human and an increasing in drug-resistant bacteria. Benefited from the flexibility, the hybrid film could be directly attached to chemical containers for spectral analysis. The Raman spectrum of Nor with different concentrations have been obtained, as shown in Figure 4.17 (a). The characteristic peaks could be observed at 10 ppm, which is 100 times lower than the concentration of Nor in commonly used injection drug, indicating a much lower detection limit for practical use of sensitive molecular structural analysis. The intensity at 1240 cm^{-1} and 1391 cm^{-1} versus their concentrations were listed in Figure 4.17 (b). A linear relationship between signal intensities and molecular concentrations was observed. It should be noted that even probed on a curved surface through the glass container, the

measurements showed good reproducibility and homogeneity, with small intensity variations due to slight differences of the laser incident angle in Raman spectroscopy. The direct detection of antibiotics on waste glass container is not achievable for the current rigid SERS substrates. The ultra-small thickness induced extremely high flexibility and small mass, enables the direct conformal attach of the hybrid platform to various curved surfaces, with minimum bending energy and large surface/volume ratio for adhesion at van der Waals interactions. The bending strain (e) is related to sample thickness (t) and bending radius (R): $e = t / 2R$. The minimum bending radius for 1 % strain is calculated to be around 0.2 mm, which is small enough for most curved surfaces in drug storage. Besides enhanced Raman scattering, the free-standing hybrid system could also be exploited for other plasmon enhanced applications, including surface enhanced fluorescence which depends on the competing effects of amplification due to local field and creation of additional non-radiative channels. Other two-dimensional materials and their heterostructures could be integrated in a similar manner to explore designer plasmonic-2D crystal free-standing hybrid smart films.
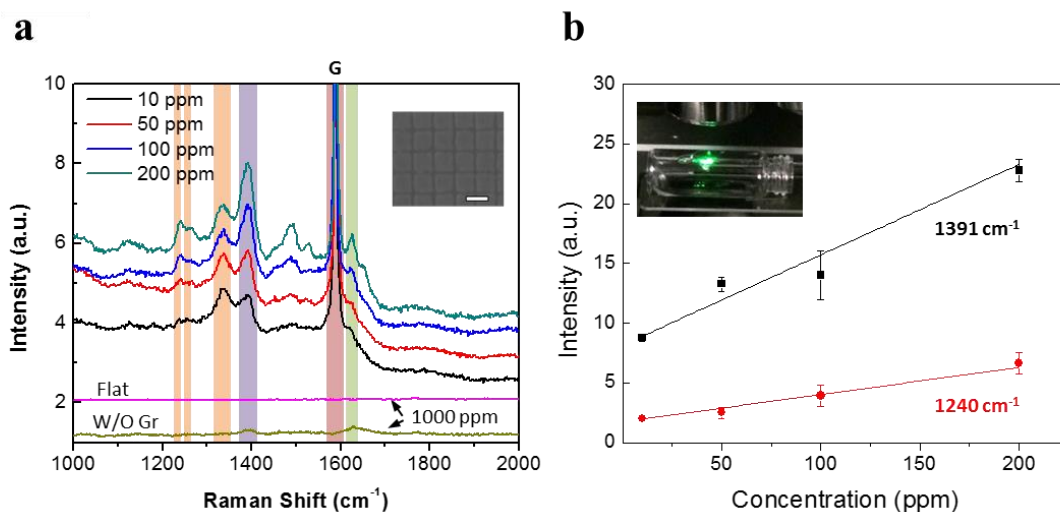
4.17 Graphene veiled flexible silver nanoarrays for the detection of Norfloxacin: (a) obtained Raman spectra at different concentrations (spectral intensities are vertically shifted for clarity). Inserted is the SEM image of the nanostructure used, scale bar: 200 nm; and (b) plot of relative Raman intensity vs. concentration of Nor. Laser excitation wavelength is 532 nm. Inserted is the camera image of the experimental setup.

4.4   Summary

In conclusion, we have demonstrated a new technique that features single step precise nanomanufacturing with good scalability. The fabricated nanostructures are found to be ultra-smooth and have large enhanced local fields at visible range. Finite element method and molecular dynamics simulations are carried out to investigate the mechanism of the imprinting process.

The top-down fabrication of a free-standing nenoengineered graphene-plasmonic hybrid film on flexible substrate is enabled by 10-nm laser induced lithography. The fabricated hybrid system is with thickness less than 5 μm and nanopatterns as small as 10-nm, making it the thinnest and finest free-standing suspended graphene-plasmonic nanoarrays to date. The fundamental behavior of light–plasmon coupling in this plasmonic nanostructure at sub-100nm is investigated. We show that anisotropic light-matter interactions with tunable field enhancement, hot electron transfer at graphene-metal interface and optical reflectance in the graphene – sub-100nm nanoengineered metal structure. Significant enhancements (above 1000) of 2D and G peaks of graphene are observed, and analyses of their positions and intensity ratios demonstrate active light-matter interaction with controlled hot-electron transfer from the underlying substrate. Stabilized light-matter interaction could be achieved on such hybrid film. This hybrid nanosystem is found to be very stable in reactive environment (sulfur) and at elevated temperatures up to 300 ^{0}C. Time-dependent analysis shows that the hybrid system is very stable in molecular sensing applications, and could increase the enhancement several times due to suppressed photo-induced damages to target molecules caused by probing laser. We demonstrate the application of such hybrid film in trace-level direct detection of antibiotics from their waste containers. Direct detection of trace amount of Norfloxacin from its waste container is developed. This 10nm lithography enabled graphene-plasmonic nanosystems will stimulate development of many novel devices in hybrid tunable hot carrier-surface plasmonic concept. This research will open exciting opportunity to design 10nm scale nanopatterned graphene-metal hybrid structures and open new avenues for such as ultrafast optical communication, optical injection of hot carriers in graphene and *in-situ* optical diagnosis of chemical reactions, where low-cost,

high-quality, controllable, bio-compatible and free-standing graphene-plasmonic hybrid films are required.

5. LASER SHOCK MANUPULATION OF METALLIC ANTENNAS

5.1 Introduction

Nanogaps between metallic nanostructures are of enormous importance in nanotechnology and have wide applications in nanolithography[170], field enhancement based plasmonic sensors[171–176], heat assisted magnetic recording[177–179], imaging[180], and trapping/manipulating of nanoscale particles and quantum dots[137,181–183]. Nano-gaped electrodes could be used in electrical sensing devices and enable ultrafast or label-free single molecule detections[184–189]. Shrinking gap distances are found to exponentially increase field enhancement[190,191], electrical current response and thus promote device performances[188].

To fabricate metallic nanostructures with small gaps, a variety of methods have been developed such as chemical synthesis and self assembly[192,193], solid-state dewetting[194], photolithography, electron beam lithography, focused ion beam (FIB) milling, and molecular-beam epitaxy (MBE). While chemical method is incapable of generating ordered nanostructures, the rests on the list are typically of high cost and need a cleanroom or high vacuum to operate. In photo/electron beam lithography and FIB, the resolutions are limited by the size of the focused beam, introducing extreme difficulties in sub-10 nm gap fabrication. Apart from the aforementioned problems in tiny gap fabrication, there have been no universal method to tune the gap distances for an existing metallic nanostructure. A few attempts to tune gap separations have been made such as chemical treating of reactive metal mirror to increase dielectric thickness[195], straining of the supporting flexible substrates[196,197], and inserting the gap with additional nanopartilcles by DNA-directed assembly[198]. The application of these methods are either limited by the specific substrate[195–197], or complexity and difficulty in mask alignments[198], and are thus limited for large-scale implementation. There is a need to produce large scale gap tuning of metallic nanostructures which are not possible using current top-down and bottom-up methods.

Here we present a general strategy[199] that utilizes the laser shock to enable ultra-fast tuning of ordered metallic nanostructure to change the distance between them and generate precise

nanoscale gaps. When two metal nanostructures are compressed, they expands laterally with gaps narrowing. However, this method has several challenges: 1) under low strain rate loading of single or polycrystalline metal nanoparticles, the anisotropic deformation of the nanostructure will result in non-uniform expansion and not well controlled gap formation; 2) When pressure is transmitted with a rigid compressor, the nanostructures expand at high speed and hit each other, resulting with fusion of the gaps. In this report, we will overcome these issues with a laser shock induced high strain rate deformation with a deformable-thin-compressor. To the best of the authors' knowledge, it is the first method to enable post-fabrication fast gap tuning of metallic nanostructures supported on a rigid substrate. When the shock loading is transmitted to the nanoparticles through the metal-thin-compressor, the 3D interaction between metal-thin-compressor and the nanoparticles will generate a protrusion of nanoscale volume in between the metal nanostructures and form an ultrafine gap. The liquid-like superplastic flow of the nanostructures will result in desirable shape changes. Molecular dynamics simulation will be conducted to reveal the process mechanism and help control the process. This ultrafast opto-mechanical method can be used to precisely control nanogaps in various shapes of metallic nanostructures at large scale, offering unique robustness for interrogation of both quantum and classic coupling interactions.

5.2   Experimental

The Au nanoantenna structures were fabricated on silicon substrate or indium-tin-oxide glass substrate (Fisher Scientific Co.). PMMA A4 (MicroChem Corp.) photo-resist was spin-coated onto the substrate at 3000 rpm for 60 s. The photo-resist was prebaked on a hot plate at 180 $^{\circ}$C for 60 s before E-beam lithography. After defining the patterns with Vistec VB6, Methylisobutyl ketone (MIBK)/isopropanol (IPA) (1:3) was used to develop the photoresist for 45 s. A thin adhesion titanium layer and an Au layer with nominal thickness of 60 nm or 100 nm were then deposited by Electron beam evaporation at 1 Å/s in a 5×10^{-7} Torr vacuum chamber. Finally, the sample was soaked in PRS-2000 solution at 80 $^{\circ}$C for 10 hours to perform lift-off.

Laser shock tuning of metal nanogaps was performed by using a Nd:YAG laser (wavelength: 1064nm) as the energy source. The schematic experimental setup is shown in Figure 5.1(a). To be brief, sacrificial layer with graphite painting on thin (4 μm) Al film (Lebow Company Inc., Bellevue, WA) was used to absorb the laser energy. Upon pulse laser irradiation, the graphite layer was instantaneously evaporated and ionized. The expanding plasma was confined by a transparent confining media and thus instant pressure shock wave was generated. In this paper, a 4 μm Al film was used as a compressor to transfer the pressure shock wave to the metal nanostructures. The beam diameter (typically around 3 mm) was controlled by a focus lens and calibrated by a photosensitive paper (Kodak Linagraph, type: 1895).

Field emission scanning electron microscopy (Hitachi S-4800) was used to monitor the geometrical changes of the plasmonic nanostructures. Surface profiles were measured using Veeco Dimension 3100 atomic force microscope (AFM) under tapping mode. The Raman scattering spectra were obtained on a home-built system. 632.8 nm laser from a HeNe source and an Olympus 100 X objective (numerical aperture 0.8) at room temperature and in open air were used in the microscopy. The excited Raman scattering signals were collected by Horiba LabRAM HR800 Raman spectrometer. Spectral uncertainty of the spectrometer was 0.27 cm^{-1}. The Raman laser energy was kept low (around 0.25 mW) to avoid any heating effects. For molecular sensing experiment, the original and the treated samples were soaked together in a diluted Rhodamine 6G (R6G) molecules (Sigma Aldrich) aqueous solution (100 nM) for 30 min, then rinsed with deionized (DI) water and naturally dried. The Raleigh linear scattering spectra were obtained with a home built hyperspectral dark-field microscope. A tungsten halogen source (3900, Illumination technologies Inc.) with highly stable light output (intensity fluctuation < 0.1%) was coupled to a dark-field condenser (NA 1.2-1.4) via a fiber optic light guide to minimize the thermal fluctuation of light intensity for accurate measurements. The scattering light was collected with a 100× oil immersion objective with an iris, and then split into two light paths, one for real-time optical dark-field imaging and the other for hyperspectral measurement.

5.3 Numerical

Au nanostructures were assumed to be a single crystal in thesimulation. A shock wave was generated by applying an initial velocity to the Al impactor. Both Al and Au are assumed to be single crystalline, and are assumed to be of <001> oriented face-centered cubic (FCC) structure with lattice constant 4.05 Å and 4.078 Å, respectively. The diameter of the nanodisks is 12 nm and height 6.5 nm. The thickness of titanium (Ti) adhesion layer is 0.8 nm. Hybrid pair styles are used in the calculations. Embedded-atom method (EAM) potentials are used to describe Au, Al and Ti of individual nanodisk. LJ potentials are used for metal-substrate interactions. The MD simulation was performed using microcanonical ensemble (NVE) with the temperature around 300 K and the time step was 1 fs.

5.4 Results and discussion

5.4.1 Nanoscale strain hardening effect
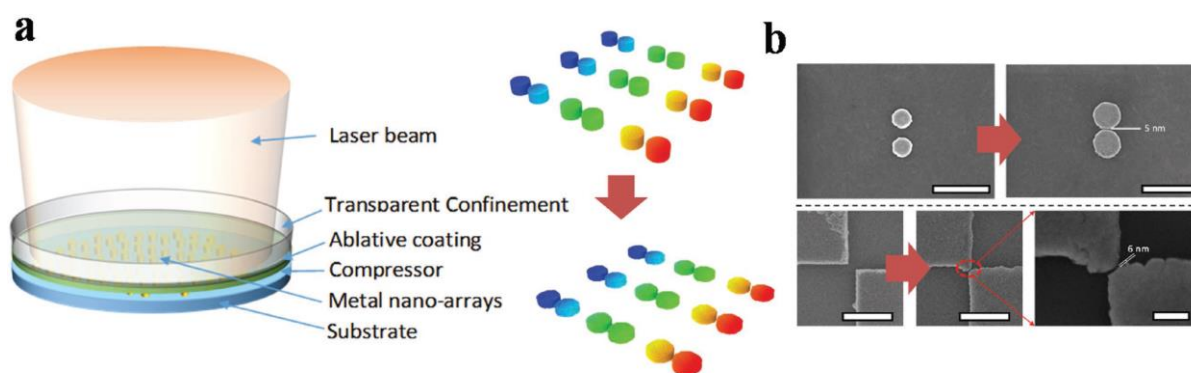
5.1 (a) a) Schematic laser-shock compression of arrays of plasmonic nanoantennas. b) Influence of laser shock on shrinking nanogaps of typical plasmonic nanoantennas. Scale bar: 500 nm; higher-magnification image: 100 nm).

We investigate the shock responses of different sizes of nanodimers under a given laser fluence. Figure 5.2 shows typical SEM images of Au nanodimers with two different diameters before and after LST. The nanostructures are treated at the same laser conditions. LST of nanodimers shows strong size-dependency. To our surprise, under laser fluence of 17 kJ/cm^2, the 160 nm nanoparticle has 75.5% (compressive) and 37.8% plastic strains in the axial and radial directions respectively, which are significantly larger than

corresponding strains of 38.6% and 19.3 % for the 300 nm nanoparticle. Similar size effect is also observed on other dimensions and laser fluences. It should be noted that this size-dependency is in sharp contrast with previous reports where small Au pillars are found to be mechanically stronger than large ones under uniaxial compression with a nanoindentor[200], and the flow stress is inversely proportional to pillar diameters[201]. To understand such an abnormal size effect, it should be noted that the previous studies are quasi-static deformations, while LST is an ultrafast process in which dynamic properties other than flow stress are dominating during LST of nanodimers. The discrepancy between responses of nanodimers under laser shock and their mechanical properties could be analyzed from the decreased aspect ratio (height/diameter) as the diameter increases, and non-equilibrium plastic flow under ultra-high strain-rate laser shock. When the nanodimers are supported by a rigid substrate, the influence of their heights is more pronounced than that of the lateral dimensions. Frictional forces from the substrate hinders lateral material flow at high strain rates. Under non-equilibrium conditions, compared with large particles, materials of small particles could flow freely with less constraints. From an energy perspective, dimers with less volume and mass require less energy to be tuned and thus show larger plastic flows. In order to study the effects of particle-particle interaction, the diameter/gap ratio (γ) is changed from 2 to 12 as shown in Figure 5.2 from the top row to the bottom. When γ is small, the two components of the dimer behave as isolated nanoparticles ($\gamma < 3$ and 2 for 300 nm and 160 nm dimer, respectively), and no mechanical interaction could be observed. However, when γ is above the thresholds, particle-particle interactions come into play.
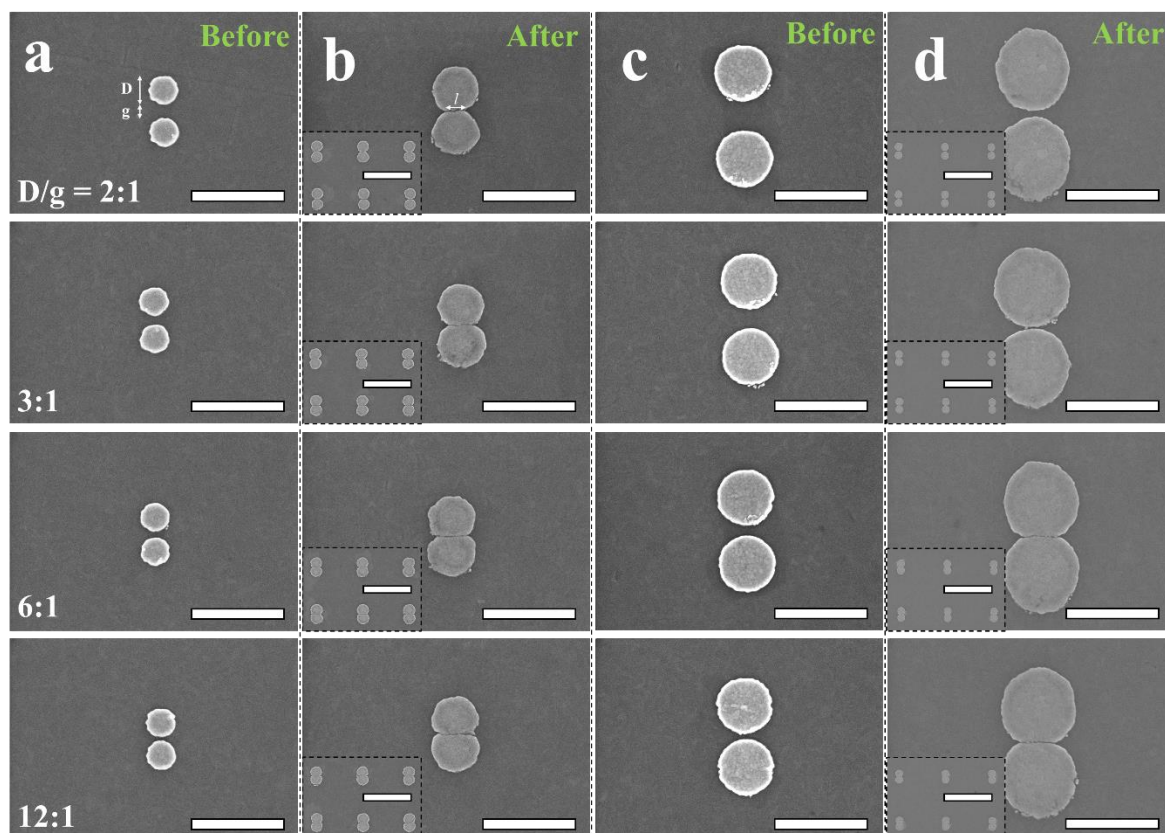
5.2 (a–d) Nanodimers with various diameter/gap ratios (2:1, 3:1, 6:1, 12:1) before (a,c) and after (b,d) laser shock. The initial nanoparticle radii are 160 and 300 nm for (a) and (c), respectively. The insets show the treated nanodimer arrays, showing the good uniformity of the process. Scale bar: 1 μm (insets: 2 μm).

MD simulation of shock compression of nanostructures could provide insights at atomic scale, especially the size effect on mechanical properties as the thickness of the nanodisks sharply decreases during the process. The initial gold nanostructures are consist of two Au cylinders with same dimensions. Upon shock compression, it is found that the diameters both the cylinders increases, and the periphery regions of the cylinders have higher atomic displacements compared to the central region, as shown in Figure 5.3 (c). Along with the movement of atoms in x-direction, one can conclude that during shock compression, the atoms are moving eccentrically and displacements are radially symmetric. The top view of the cylinders shows good circles after deformation. This should results from isotropic material properties, structure dimensions, and loading conditions. The gap distance between two cylinders is thus decreased, as the center is stationary during the process. As

the strain rate in this simulation is quite high and the shock wave is propagating from the top to the bottom, the structure has larger diameters at the top of the cylinders.
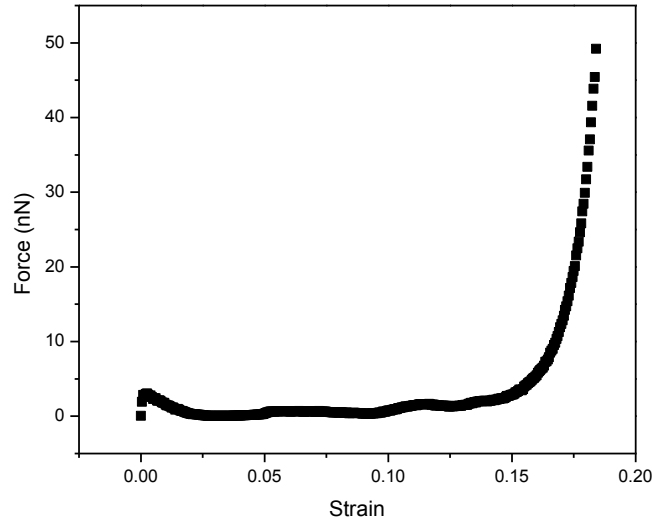
5.3 Load-engineering strain relationship monitored during the simulation

In this displacement controlled loading situation, the geometrical changes and loading force are monitored and plotted, as shown in Figure. The engineering strain is calculated by using the equation $\varepsilon = |(L-L_0)/L_0|$ which indicates the displacement of atoms movement. At the beginning stage of the deformation, the cylinder is under elastic deformation which shows only tiny strains. After that, the force quickly decreases accompanying with dislocation dislocation nucleation and propagation in the second stage, similar to yielding in macroscopic guasi-static compression test. Finally when dislocation density reaches a certain value, the force needed to generate additional strain exponentially increases and the deformation would stop if the force required is larger than provided. Although the simulation settings are quite different from those in real experiments such as strain rate, loading mode and geometries, it could provide meaningful atomic insights to laser shock compression of nanostructures. And the structure is found to become stronger after two stages of deformation.

5.4.2 Effects of laser processing condition
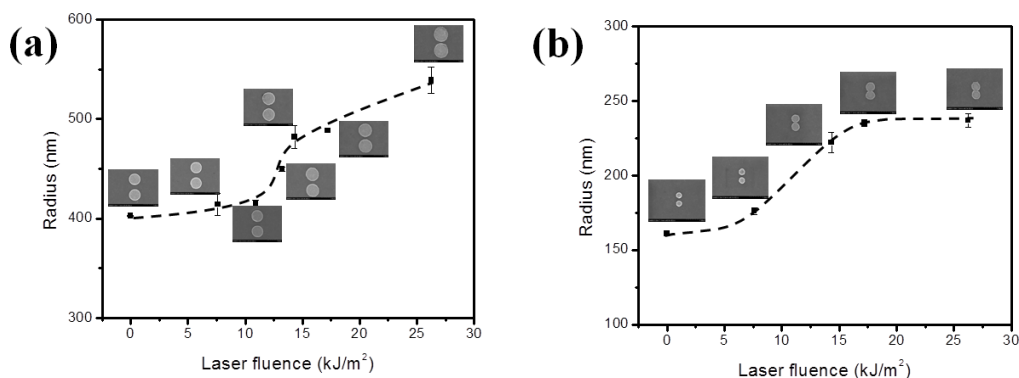
5.4 Influences of laser energy fluence on nanoparticle dimensions: (a) initial radius around 400 nm; (b) initial radius 160 nm.

The geometries of nanodimers and dimensions of the closing gaps are determined by the laser fluence. As can be seen in Figure 5.4 and Figure 5.5, several different process windows could be distinguished. At small laser fluences (0 - 12 kJ/m^2 for 400 nm dimer), the shock pressure generated by ablation could hardly trigger grain boundary movements and dislocation sources in the polycrystalline Au nanodimers. The aforementioned size effect also shows at various laser fluences. The gap shrinking of small nanodimers are much faster than that of the large ones. In the range of 0 - 12 kJ/m^2, less than 10 nm gap separation change could be observed for the 400 nm dimer (while the 160 nm dimer shows more than 100 nm gap shrinking). The generated shock pressure is below Hugoniot elastic limit (HEL), and it is insufficient to generate irreversible plastic deformation through dislocations creation and motion. The gap change is mainly due to onset of grain boundary (GB) accommodation mechanisms. At medium laser fluences (12 - 17 kJ/m^2), the gap closes sharply. In this range, there is dramatic increase of dislocation densities and grain movements, as the laser pressure exceeds the threshold force required for triggering dislocation avalanches on multiple slip systems. It should be noted that smaller particles require less laser fluence in this window. The shock pressure (less than 1 GPa) needed to trigger dislocation motions is found to be much lower than previous studies where pressures are typically 5-50 GPa[202,203]. Such differences are attributed to the lack of lateral confinements which significantly decreases the hydrostatic pressure (P), which is

positively correlated to the flow stresses for GB sliding (σ_{GB}) and dislocation plasticity (σ_{Dis}).

$$\sigma_{GB} = (\sigma_0 + \alpha P)(1 + d/d_0)$$ Eq. 5.1

Where σ_0 is the flow stress for amorphous metals at zero pressure, d the grain size, α and d_0 the constants. According to Hall-Petch relation,

$$\sigma_{Dis} = C(G_0 + \beta P)(d/d_1)^{-0.5}$$ Eq. 5.2

Where G_0 is the shear modulus, C, β, d_1, the constants. For grain size below critical values where inverse Hall-Petch relation holds, the influence of P on σ_{dis} is still valid. Compared to steady shock waves and nonequilibrium one-dimensional waves with periodical boundaries, the hydrostatic pressure in LST of nanodimers is relaxed through nanoparticle flattening, while the deviatoric stress builds up. In the third laser window, it is found that deformation almost stagnates, with little incremental deformation when laser fluence is further increased. This indicates that with LST, the mechanical properties of Au nanodimers are strengthened significantly. As the aluminum (Al) film is used as a MTL, the increased laser pressure is consumed by plastic deformation of the MTL other than Au nanodimers.
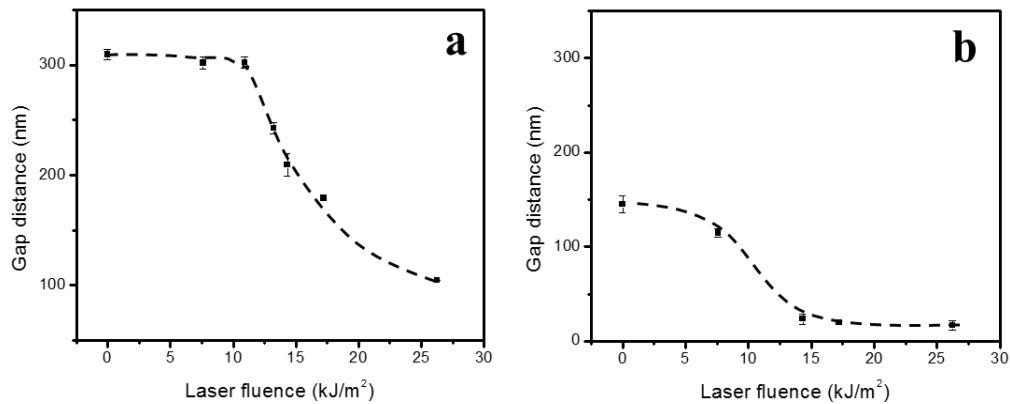
5.5 Influences of laser energy fluence on antenna nanogaps : (a) initial gap distance around 300 nm; (b) initial gap distance 150 nm.

5.4.3 Interaction of MTL and metallic nanostructures for nano-gap tuning

Although we observed the ultrafine nanogaps are formed after LST, it is not clear how the nano-line-gaps are formed instead of nano-point-gaps, and if the gaps are formed by "hit-n-separate" or other unknown mechanism. Molecular dynamics simulation is used to shed

light on gap formation mechanism during LST. We apply an initial velocity (V_0) to the deformable MTL based on the following equations[30].

$$P^2(\tau) = mI_0\alpha/2\tau(\alpha + 1) \qquad \text{Eq. 5.3}$$

$$V_0(\tau) = 2P(\tau)\tau/m \qquad \text{Eq. 5.4}$$

Where I_0 is the nominal laser intensity, τ the pulse duration, m the mass of metal-thin-compressor, P the pressure generated during laser irradiation, α the factor to account for increase of plasma thermal energy by absorbing laser irradiation. A typical velocity of 0.5 km/s (~0.15 of sound speed of Au) is applied, which yields a strain rate of 10^{11} s^{-1} in the present case. The deformation shown in Figure 5.6 finishes within the first 30 ps of interaction between Al MTL and Au nanodimer. The Al MTL placed on nanofeatures is subject to superplastic flow upon laser shock. This enables stress-wave transmission from Al MTL onto targeted Au nanodimer and interactive deformations between them (compare Figure 5.6 (a, b) and (c, d)). At the initial stage, due to lateral confinement induced large strain gradients[204] and hydrostatic pressure, MTL could perform stiffer than Au nanodimers. The nanodisk transforms to a dome shape within 10 ps as the plastic wave reaches the supporting substrate. Au and Ti show similar deformation morphologies (Figure 5.7) at this stage. The nanodimer is strain hardened in the second stage. From 10 ps to 20 ps, as the deformation continues, different strain-hardening effects of Au and Ti are observed. The Ti layer gets strengthened faster than Au and its strain is significantly lower. The adjacent Au particles approach each other and form a straight gap in between. It should be noted that with strain hardening of Au and Ti, the AL MTL is further deformed, generating higher strain gradients inside. Similar to imprinting of metallic thin film on a silicon nanomold [34], the strain-hardened nanodimers serve as a dynamic mold for deformation of Al-thin compressor and the bar separating adjacent holes in Al is narrowed. In the final stage, shock momentum quickly dissipates. After 20 ps, the velocity of Al quickly decreases to zero and the deformation finishes. Homogeneous deformation is observed even at large plastic strains due to the high strain-rate effect. The deformations of Au and Al are found to be interactive and collaborative. The adhesion layer (Ti in the present case) engages in the process and its thickness and mechanical properties are thus anticipated to influence final geometries. The calculated geometries of Au nanoparticle and Ti adhesion layer closely resemble the experimental ones as shown in Figure 5.7.
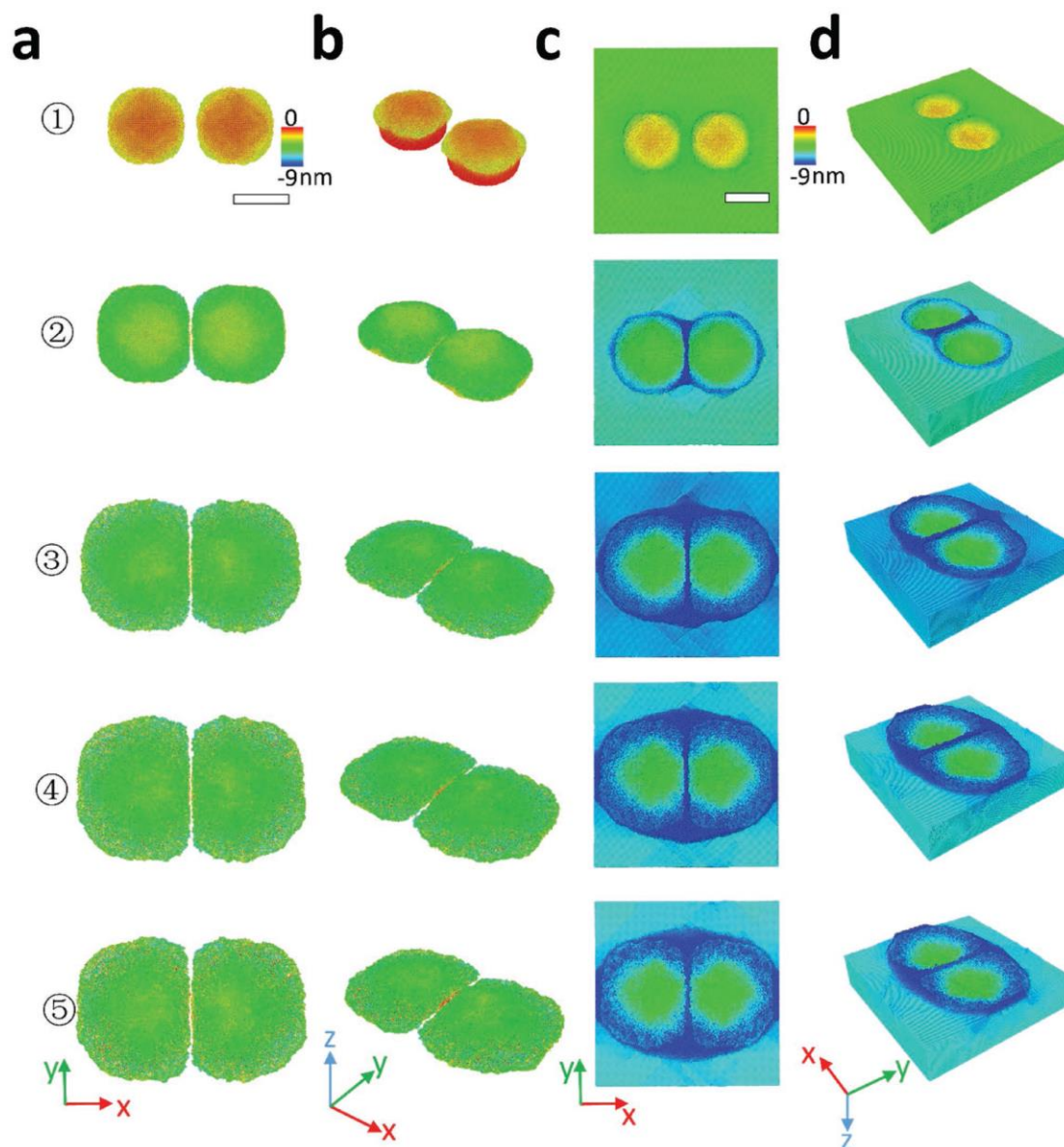
5.6 Ultrasmall gap formation by collaborative deformation of gold nanodisks and aluminum film as flyer. a) Atomic snapshots of a gold nanodimer (in top-view) during laser shock at different time steps (from 1–5: 5 ps, 10 ps, 15 ps, 20 ps, and 30 ps). The color represents the z-displacement of the gold nanodimers. b) Tilted 3D view of (a). c) Temporal evolution of aluminum deformation (top-view). d) Corresponding 3D view of (c). Scale bar: 5 nm.
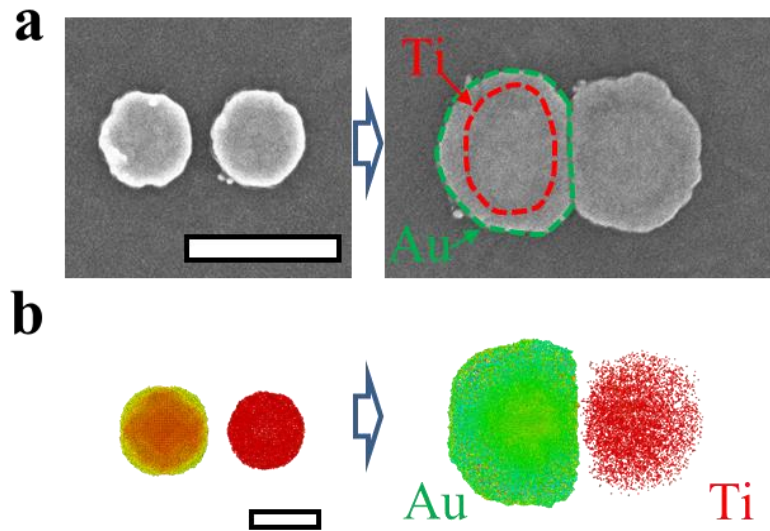
5.7 Experimental (a) and simulated (b) nanodimer geometries. Scale bars: 500 nm (up), and 5 nm (bottom).

The gap shrinking and ultrafine gap formation is a result of 3D interaction of MTL and metal nanostructure. The mechanical properties of the MTL could affects the deformation and gap formation during LST significantly. On the one hand, the effective laser shock pressure is related to the shock impedance of the compressor[8,144]. The propagation of the stress wave introduces continuous dynamic yielding of the compressor, which results in energy dissipation. A MTL with less or no plastic flow could be more efficient in delivering shock waves to target metallic nanostructures. On the other hand, the deformation of the compressor introduces nonlinearity at the MTL-antenna contacts, which influences shock wave transmissions and results in confinement for plastic flows of the nanodimers.
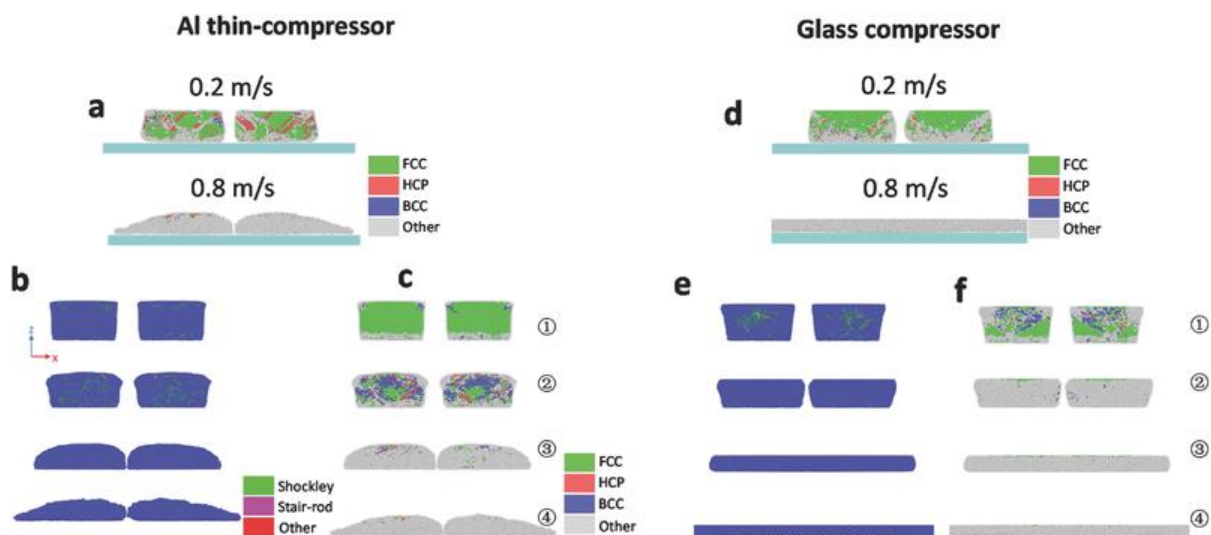
5.8 For Al thin compressor: a) Disordering and crystal structure analysis at the cross section for Al thin compressor at speeds: 0.2 and 0.8 km s^{-1}. Scale bar: 5 nm. b) Cross - sectional view of dislocation initialization and evolution in the nanodimer under laser shock at time steps of 2, 5, 10, and 30 ps. Impactor speed: 0.8 km s^{-1}. Scale bar: 5 nm. c) Corresponding crystal-structure analysis of (b). For glass compressor: d) Disordering and crystal structure analysis at the cross section at speeds: 0.2 and 0.8 km s^{-1}. e) Cross-sectional view of dislocation initialization and evolution in the nanodimer under laser shock at time steps of 2, 5, 10, and 30 ps. Impactor speed: 0.8 km s^{-1}. Scale bar: 5 nm. f) Corresponding crystal structure analysis of (e). (Note: FCC: face-centered cubic; HCP: hexagonal close-packed; BCC: body-centered cubic; Other: unknown coordination structure).

MD simulation is conducted to reveal the difference of the deformation in nanodimer using two MTLs, Al-deformable MTL and glass-rigid MTL. As shown in Figure 5.8 (a) and (d), for both MTLs, it is observed that dynamic recrystallization of Au nanodimer takes place during LST with V_0 of 0.2 km/s. While for V_0 at 0.8 km/s, amorphorization/melting of the FCC nanodimers is observed. When the two nanodimers come close, the ones under glass MTL hit and fuse together. The two amorphorized nanodimers hit and join together like liquid after laser shock induced high speed impaction. However, the nanodimers under deformable-MTL are separated with an ultrafine gap, consistent with experiments, as results of the 3D interaction between deformable-MTL and the nanodimmers, as shown in Figure 5.7. The microstructure changes during the LST under two types of MTLs are also shown in Figure 5.8. For deformable MTL, the Au nanodimers form multiple dislocation sources at the shock front (stage 1). The dislocation density increase as the deformation proceeds (stage 2). In stage 3 and 4, the nanodimer evolves to non-crystalline structure

(Figure 5.8 (b)). The fast elastic stress wave leads the gap tuning process. It has multiple reflections and transmissions at interfaces including MTLl-Au and substrate-Ti contacts before the slower plastic wave with a speed of ~65 km/s deforms Au along its path and form a mushroom shape. Numerous Shockley partial dislocations are nucleated inside Au and a phase change from FCC to BCC is observed (Figure 5.8(c)) in stage 1 and 2. The amorphorization of nanodimers starts from the top and bottom surface and propagates to the center and finally change to liquid like metal in stage 4. In the case of rigid MTL, the amount of deformation is much severer than using deformable MTL (comparing Figures 5.8 (b-c) with 5.8 (e-f)), as most of the energy is used to deform the Au nanodimers instead of dissipated in stress wave propagation in MTL. The dislocation density (Figure 5.8 (e)) is much higher than that in Figure 5.8 (b) (stage 1). From stage 2, the majority part of the nanodimers changes to amorphous. In stage 3 and 4, the two liquid-like metal hit and join seamlessly.
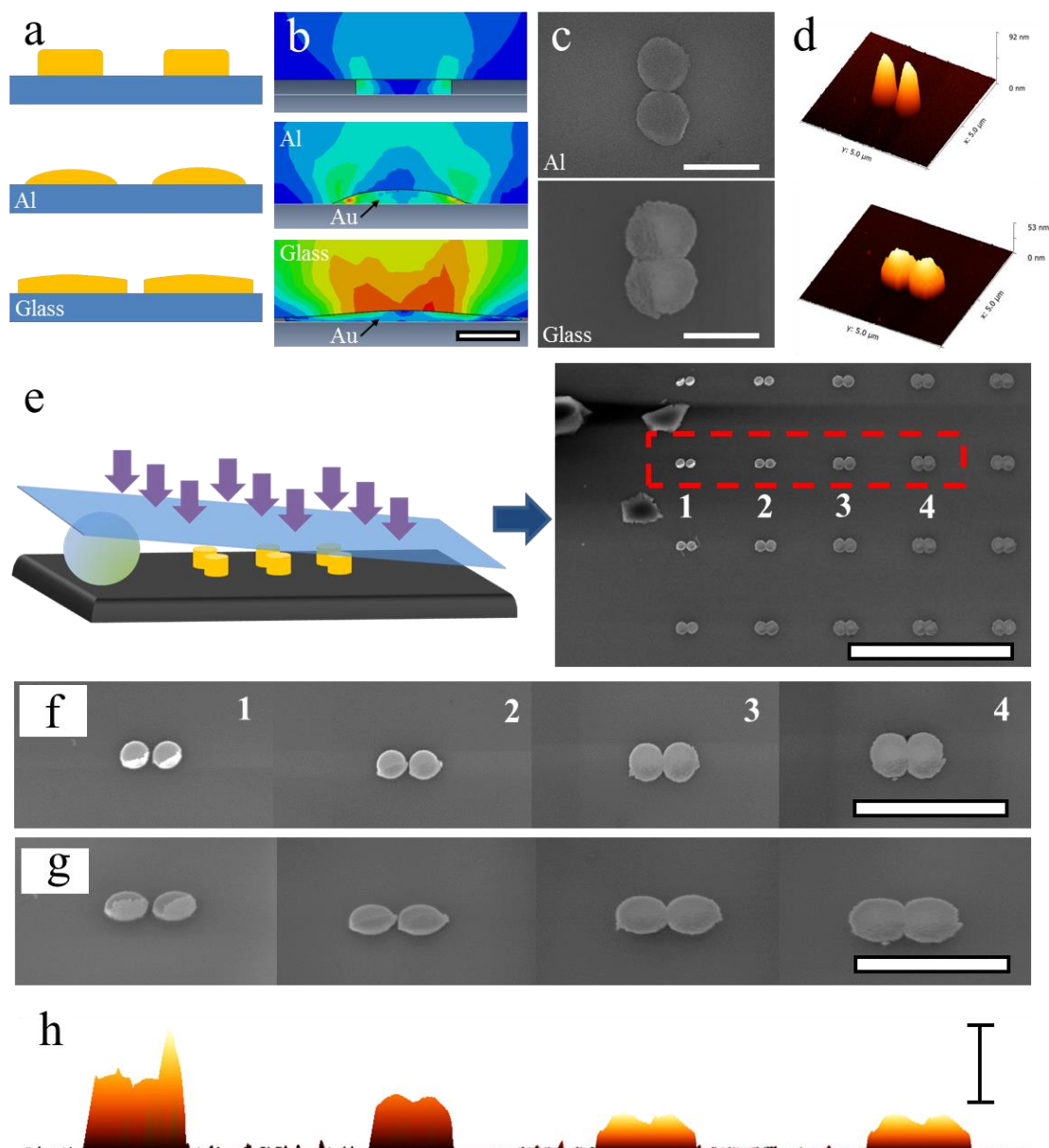
5.9   a) Schematic of Au nanodimers before and after LST with Al and glass flyers. b) Finite element modeling of LST with different flyers. Scale bar: 300 nm. c) SEM images of dimers processed with Al and glass flyers (b2, c2). Scare bars: 1 μm. d) Corresponding AFM images of (c). e) Laser shock tuning with glass flyer and preplaced silica particles for spatially varied pressure. SEM image of the treated nanoantennas is shown on the right. Scale bar: 10 μm. f) High-magnification SEM images of individual nanoantenna indicated in (e). Scale bar: 3 μm. g) Tilted view of (f). Scale bar: 2 μm. h) 3D views of dimers measured by AFM. Scale bar: 100 nm.

In order to validate gap formation in LST with rigid MTL, we use thin glass slide (170 μm) as the compressor instead (Figure 5.9). The bending stiffness and compressive strength of

glass are around 29×10^6 N·nm and 1 GPa, respectively, both of which are significantly higher than corresponding values of Al (190 N·nm and 140 MPa). As shown in Figure 5.9 (a-c), the nanodimer deformed through a rigid MTL is significantly larger than that obtained from the deformable MTL. According to the AFM images in Figure 5.9 (d), the nanodimers in the case of the deformable MTL are more cone-shaped, demonstrating better flexibility/conformability of the deformable MTL consistent with the simulation results. We then place hard silicon micro-particles around Au nanodimers as spacers and carry out LST with a glass rigid MTL. The initial dimensions of all the nanodimers are the same. However, as the silicon particles hinder pressure transfer (Figure 5.9 (e)), the deformation of nanodimers is in gradient distribution (Figure 5.9 (f-h)) with more severe deformation far from the Si particles. The nanodimers (#1 and #2 in Figure 5.9 (f-g)) are deformed with gap-shrinking. With the amount of deformation increase, the nanodimers hit and join (#3, #4 in Figure 5.9 (f-g)) as liquid metals, similar to the simulated results in Figure 5.8 (e-f). The responses of the nanodimers are thus indicators of interfacial contacts and dynamic properties of the MTL.

LST could also be used as a simple and cost-effective technique to study dynamic mechanical responses of various nanomaterials at strain rates not achievable in any other conventional methods including the state-of-the-art Hopkinson bar test. This could open a new regime of ultra-high strain rate testing of mechanical properties at nanoscale. Besides the aforementioned dimer structures, LST is versatile and can effectively change the geometries of other nanoantennas, such as concentric rings, bowties, split-ring and V-shaped resonators, and is anticipated to significantly impact on their radiation properties. SEM images of these plasmonic nanoantennas treated with various laser fluences are shown in Figure 5.10. Compared with the surface morphologies obtained on nanodimers (Figure 5.2), material flow for other noncircular geometries is not isotropic. It is found that laser shock tends to smoothen sharp geometrical features, especially when the fluence is above 14 kJ/cm^2. As we discussed earlier, the deformation of nanoantennas is influenced by strain hardening, strain gradient plasticity, strain rate effect, and nanoantenna-MTL/substrate interactions. LST of complex geometries are thus more complicated. Future studies are need to unveil the mechanisms beneath and insights for process control.
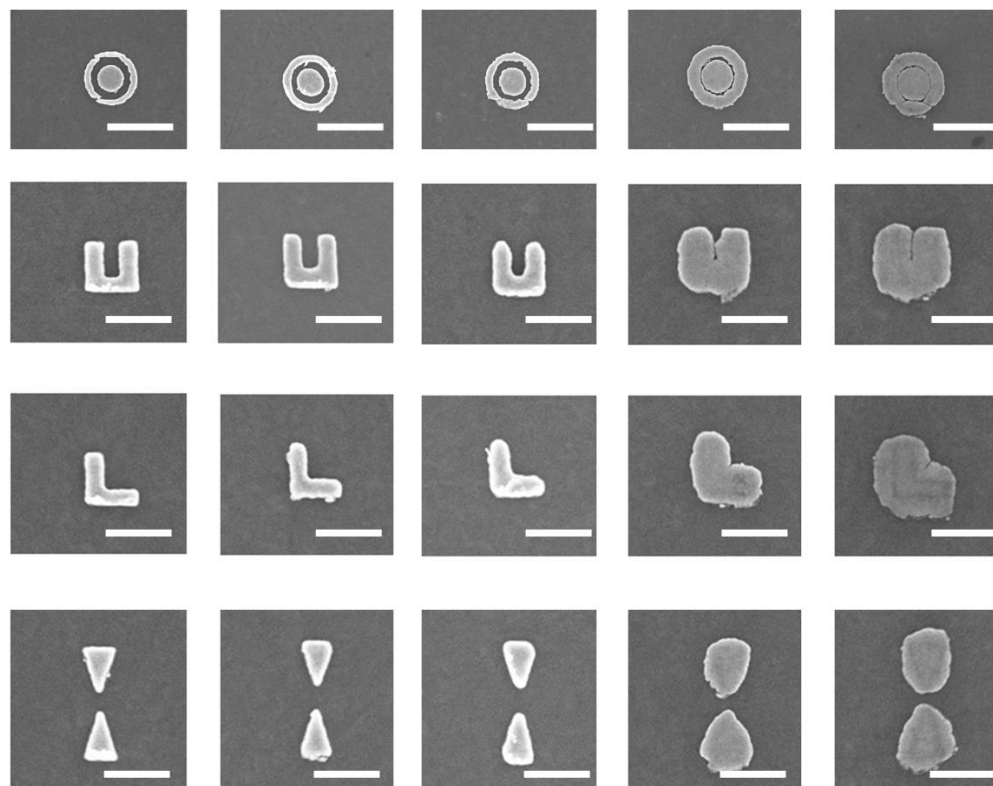
5.10 Laser shock of different Au nanoantennas with increaseing laser energy fluence from left to right: before laser shock, laser shock with fluence 7.5 kJ/cm^2, 11 kJ/cm^2, 14 kJ/cm^2, and 17 kJ/cm^2. Scale bar: 1 μm.

5.4.4 Optical properties of the LST treated gap nanoengineered metal structures

We further test the optical properties of the nano-gaped metallic structures by dark field spectroscopy and Raman spectroscopy. The treated nanodimers with enlarged nanoparticle size and shortened interparticle gap distance show red-shifts of their plasmon modes because of combined effects of geometrical resonances and plasmon hybridization. The initial diameters of the nanoparticles are 100 nm and the gap distance is 45 nm. For the original structure, there is no or very weak local surface plasmon resonance (LSPR) coupling between two nanoparticles due to the large gap distance. Because of structural symmetry, the original dimer just has one LSPR mode located at 597.5 nm (black line in Figure 5.11). With laser shock at 7.5 kJ/m^2, the first peak of the red line, corresponding to the transverse or anti-bonding mode, is red-shifted due to the larger nanoparticle size,

which agrees with the previous theoretical study. The second peak (located at 735 nm), corresponding to the bonding or longitude mode, has a lower intensity than the previous one since the gap distance is still too large to generate strong coupling. Both peaks continuously shift towards longer wavelengths with higher laser fluence. The intensity ratio of the peaks increases with increasing laser fluence of LST, indicating an enhanced plasmon hybridization. For the nanodimer supported on ITO glass, a remarkably narrow dip at 670 nm corresponding to charge transfer plasmon mode is observed at laser fluence of 11 kJ/m^2.
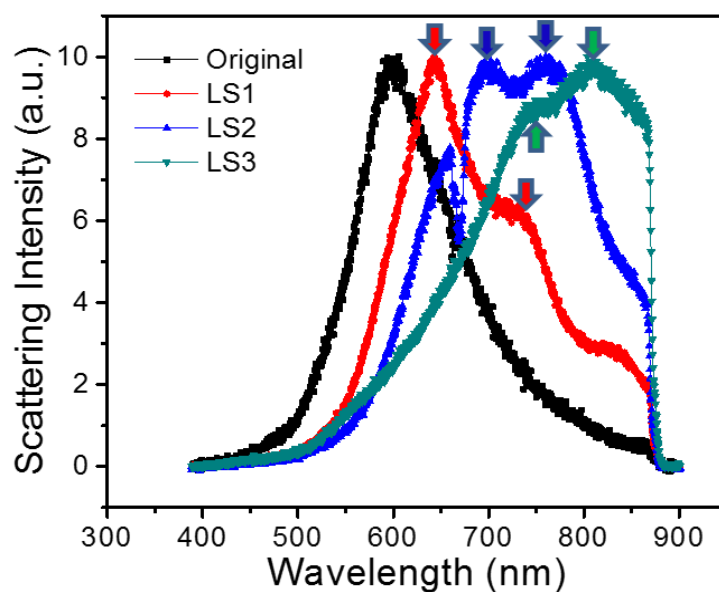
5.11 Dark-field scattering spectra (normalized to the peak intensities) of the nanoparticle dimers.
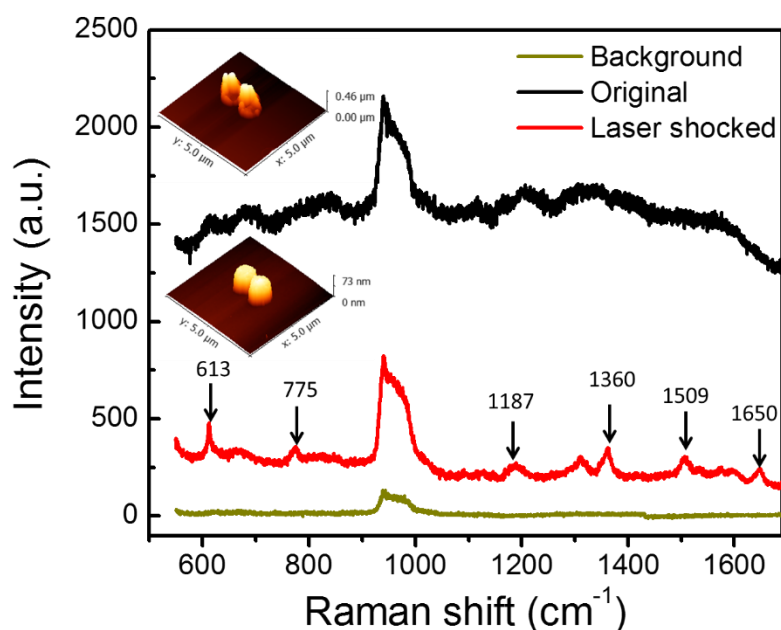
5.12 SERS performances of Au nanodimers before and after laser shock (LS1). The insets show the corresponding AFM images. Laser excitation wavelength: 633 nm. The laser polarization direction is parallel to the dimer axis.

With the tunable nanodimer geometries and optical properties, various applications could be explored. Surface enhanced Raman spectroscopy (SERS) of plasmonic nanoantennas is of great interest to biologists, chemists, physicist, and engineers as it can find its wide use in cell visualization, bio-sensing, electron/charge transfer and energy harvesting devices. We then probed the influence of LST on SERS performance of plasmonic nanostructures. The original and laser shocked samples were immersed in diluted R6G solutions for the purpose of detecting the changes in molecular sensing capability. As shown in Figure 5.12, the untreated sample has no distinguishable Raman signatures of the molecules, and strong photoluminescence background from the Au nanostructures. On the contrary, the shocked plasmonic nanodimer shows a reduced background. Characteristic Raman signatures of R6G molecules at 613, 775, 1187, 1360, 1509 and 1650 cm^{-1} become distinguishable, demonstrating an enhanced sensing capability with laser shock. It should be noted that although rough surface features could serve as SERS hot spots, they also increase electron scattering rates and damp localized surface plasmons.
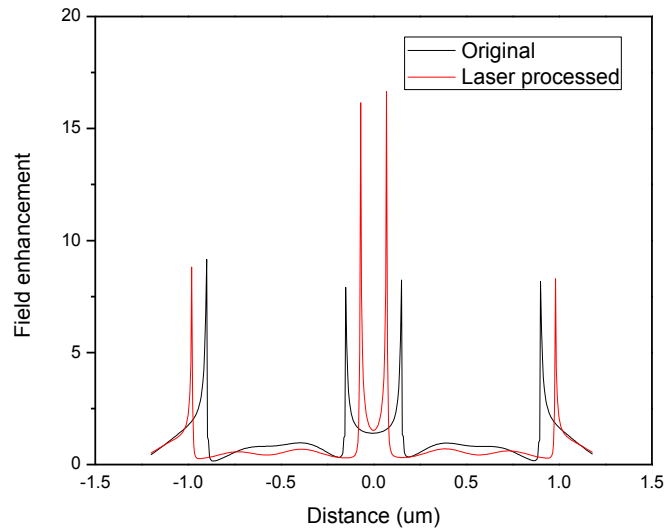
5.13 Calculated field enhancement factors before and after laser shock compression.

Figure 5.13 shows a line profile of calculated field enhancement after laser shock compression. As shown in the figure, as the diameter of the disk increases after laser shock processing, the field enhancement peaks between two disks move closer and the value increases two folds, while the field enhancements at the other two ends are almost unchanged. The huge increase of the field enhancement due to laser shock compression would definitely better the performances of the device in applications such as optical metamaterials, plasmonics, electronics, photonics, imaging and sensing. Further increase of the field enhancement by using different laser pressure, material properties, and initial geometries will be taken out in the future. The observed increase of sensitivity agrees well with our numerical simulations based on finite difference time difference (FDTD) method. Besides gap size shrinking for enhanced local fields and resonance shifts, more work is needed in the future for optimizing optical properties of plasmonic nanoantennas with LST.

5.5   Summary

This chapter presents a general strategy that utilizes the laser shock induced superplastic forming to enable precise nanoscale gap formation of ordered metallic nanostructures. The MTL has significant effects on the plastic deformation and gap formation of the

nanostructure arrays. Under laser shock compression with a rigid MTL, the microstructures change from crystalline to liquid-like metals, expand at high speed and hit each other, resulting with shrinking and fusion of the gaps. However, when a deformable MTL is used, its interactive and collaborative superplastic forming with targeted metallic nanoarrays generates self-limited gap shrinking and an ultrafine line-gap forms. Sub-10 nm metallic nanogaps could be fabricated ultrafast with large scale. Nanoparticle size-effects on nanogap formation was also studied. This ultrafast opto-mechanical method can be used to tune the geometries of various metallic nanostructures. The process enables tuning the surface plasmon resonances of nanoantennas and boosts the performance of their applications in surface enhanced Raman scattering. The nanodimers after LST show red-shifts of their plasmonic resonances and emergences of additional peaks due to enhanced light confinement. This ultrafast opto-mechanical nanomanufacturing method provides a general strategy to tune nanogaps in many metallic nanostructures at large scale, offering unique robustness for interrogation of both quantum and classic coupling interactions.

6. LASER SHOCK PATTERNING OF NANOWIRES AND 2D CRYSTALS

6.1 Introduction

One-dimensional materials such as Semiconductor nanowires (SCNWs) and two-dimensional crystals such as graphene and MoS_2 have unique electrical and optical properties. Due to the ever-increasing thrust for enhanced packaging density of nano-scale device components, these materials assume incredible significance and are deemed as potential candidates as nanoscale building blocks for numerous applications in electrical, electromechanical, photovoltaic, optical and optoelectronic devices.[205–212] Significantly, such nanowires can fulfill dual purposes, first being its role as interconnects and the other one as functional material components. One can achieve band-gap engineering by composition modulation[213,214] or by diameter variation[215]. As an alternative to such approaches, elastic strain offers a promising approach to modulate electronic structures of 1D and 2D materials and their carrier dynamics. It was observed that SCNWs can sustain much larger strains than their bulk counterparts, due to increased mechanical strength with less defects and larger surface/volume ratio[216,217], leaving large room for strain engineering. Strained silicon technology has been applied to boost transistor performance through mobility enhancement[218]. Germanium, which is an indirect band-gap material, can be band-gap engineered to a direct band gap of 0.34 eV at 4.2 % longitudinal tensile strain[219]. Band-gap engineering has been reported to greatly impact on its carrier mobility [220], luminescence behavior[221] and lasing action[222]. Enhanced electronic mobility via strain engineering would pave the way for germanium nanowires (GeNWs) to be employed as a promising material for the channels in complementary metal–oxide–semiconductor (CMOS) devices and flexible electronics. Straining of 2D materials such as graphene, black phosphorus, and Transition metal dichalcogenide (TMDC) monolayers has attracted intense research interest in order to tune the band structures[223–227].

For one-dimensional nanowires, the straining technique has been limited for a long time to lattice mismatch which has several challenges including high density of defects, strain relaxation, and differences of doping diffusion properties[218]. Alternative methods

developed in recent years, such as bending with AFM or a manipulator[217,228,229], stretching in sophisticated micromechanical strain module[230] or etched nano-bridges[229], and buckling through a pre-strained elastic substrates such as PDMS[231,232], are beneficial for understanding the strain-induced physical and electrical property changes. However, these methods are difficult to be implemented for practical applications in semiconductor technology, given the fact that they are either inefficient to manufacture in large scale due to the one-by-one deformation nature, or incapable of integrating reliable electrodes and gating for the fabrication of transistors. It is therefore, imperative to develop a CMOS-compatible approach to controllably deform chemically synthesized SCNWs in a scalable manner, thereby opening the potential to practically implement strain engineered physical properties.

To realize elastic straining of SCNWs with CMOS compatibility, it is desirable that (a) the strain level should be tunable and dislocations or cracks should be avoided; (b) the elastic strain needs to be self-preserved after processing; and (c) the strained SCNWs need to be compatible with silicon technology and sit on substrates with reliable gate modulations. In this article, we report on the exploitation of a laser ablation based approach with a predefined nanomold for guided elastic straining, which meets these key requirements. In previous studies, laser shock has been demonstrated to achieve shaping of metal thin film and nanomaterials [10,46,144,155,233], with the introduction of high-density dislocations, plastic flow and defects. However, unlike metallic components which are highly flexible and mechanically robust, SCNWs are brittle in nature and could easily break at strains slightly higher than their limits. The application of laser shock as an ultrafast approach for parallel shaping of SCNWs has never been exploited.

In this chapter, the straining of germanium nanowires[234] would be explored in detail. After that, the progress on deformation of two-dimensional material such as graphene is reported.

6.2   Materials and methods

GeNWs growth: GeNWs were grown by vapor-liquid-solid (VLS) mechanism in a chemical vapor deposition (CVD) chamber following the literature procedure.[23] In brief;

the substrate used for the purpose was thoroughly etched with a buffered hydrogen fluoride (HF) solution before any growth commences to remove the surface oxide layer. A well-mixed solution containing gold colloidal nanoparticles (AuNPs) and 10 % HF/H_2O was then dispersed on the substrate. The substrate was then rinsed, dried, and loaded in the CVD chamber. The substrates were then annealed at temperatures in the range of 280 - 400 ^{0}C for about 5 min in flowing hydrogen at pressure of 100 Torr. The duration between the particle deposition and the onset of annealing was approximately 10 min. Post annealing, GeNW growth was carried out using mixture of GeH_4 (10 sccm) which was actually 10 % diluted in hydrogen and 40 sccm of hydrogen at a total pressure of 100 Torr and a substrate temperature of 280 ^{0}C. Growth took place for 40 minutes. The TEM images of the Ge NWs are shown in Figure 6.1.
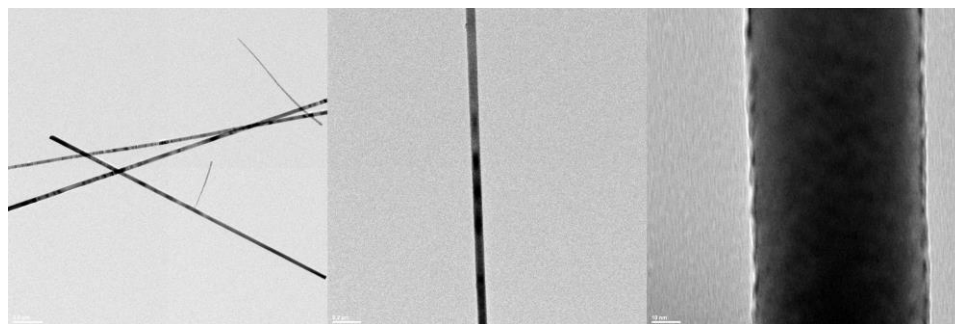
6.1 TEM images of Ge NWs used in the study.

2D crystals: Graphene or hexagonal boron nitride grown on copper foil (Graphene Supermarket, Inc.) was spin spin-coated with a sacrificial PMMA layer, baked at 180 °C for 2 min and then the bottom graphene was etched away. For graphene transfer, typical wet transfer methods were applied.

Nanowire transfer: After the mold preparation, the GeNWs were transferred onto the mold surface by a contact sliding or direct printing process. In contact sliding, the substrate with grown GeNWs (donor substrate) was faced down against the mold substrate (acceptor substrate) and slid to the direction perpendicular to the length direction of the mold channels with the application of mild pressure. GeNWs were then transferred to the mold substrate with the alignment along the sliding direction, resulting in laterally aligned GeNWs suspended over the mold channels.

MD simulation was used to investigate the evolution of microstructure and defects and the generation and distribution of atomic scale stress/strain. We used MD simulations to

complement our FEM simulations at continuum level with information about the nanoscale deformation mechanism of LSI. The open source MD package LAMMPS was used in all our MD simulations. The mold is composed of silicon with diamond lattice with size 5.48 Å.

6.3   Deformation of germanium nanowires
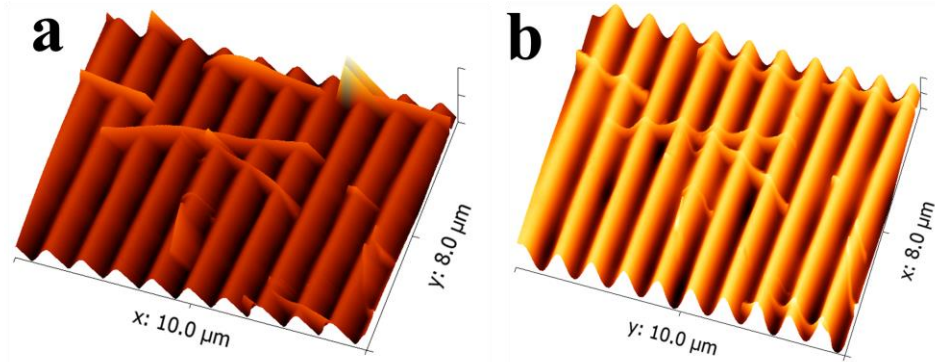
6.2 AFM images of the same nanowires before and after laser shock. No GeNW is lost after LSES, giving a shaping yield of 100 %.

To tackle the present limitations, we develop a laser shock elastic straining (LSES) approach which includes four key steps. First, nanoscale-channels on Si wafer are fabricated by electron-beam lithography or focused ion beam (FIB) milling. Thermal annealed SiO_2 serves as back-gate dielectric for field effect transistors (FET). Second, a thin layer of insulating polymer is deposited on the nanostructured silicon wafer through dip/spin coating and cross-linked by thermal annealing. Polyvinylpyrrolidone (PVP), a polymer which has been demonstrated to be a high-performance gate dielectric[235,236] with dielectric constant[237] similar to SiO_2, is used in this study to serve as cushion of nanowire shaping and elastic strain preserver. Third, SCNWs (germanium-GeNW or silicon - SiNW) are grown by bottom-up vapor deposition or top-down lithography, and then transferred onto the mold surface by contact sliding [238], transfer printing or direct printing process[120]. As shown in Fig. 1b, the SiNWs are fabricated by e-beam lithography (EBL) of silicon-on-insulator (SOI) wafer followed with dry etching Si layer and lift-off. The SiNWs were then transfer printed onto the nanomolds surface. The GeNWs are grown by CVD and

transferred on to the nanomolds by contact sliding. Finally, a nanosecond laser is used to generate shock wave to deform the SCNWs into the nanomolds conformally.

Our approach yields ultrafast elastic straining of brittle SCNWs on silicon substrates. The GeNWs are deformed conformally onto the nanomolds by laser shock elastic straining (LSES), as shown in Figure 6.2. No SCNWs are lost after LSES, giving a shaping yield of 100 % for the GeNWs investigated. During the LSES, an intense pressure is exerted uniformly on the nanowires, which deforms thousands of nanowires into the mold cavities in parallel. The shock pressure can be controlled by the laser intensity, confinement, and ablative coating. The nanowires can be considered as free beams at suspending parts and are pinned at the bar sections by the high pressure. There is no sliding or turning of the nanowires on the mold surface. Highly reliable controlled deformation in the elastic region is critical and is realized by smooth transitions of mold geometries and the polymer cushion. As the nanowires gain the momentum from laser shock and get deformed against the polymer thin layer on silicon mold, viscoplastic deformation of the polymer consumes excessive shock energy and eliminates stress concentration by avoiding point contacts between the brittle SCNWs with the substrate. It should be noted that the laser shock process takes place within tens of nanoseconds, yielding an ultra-high strain rate not achievable in traditional methods. This would inhibit brittle cracking triggered by random imperfections on the nanowire surface in the case of low strain rates[239]. The advantage of LSES also lies in the fact that the elastically deformed SCNWs, which normally tends to relax to the unstrained state after unloading, is self-anchored through van der Waals interactions between SCNWs and the polymer thin layer, while state-of-the-art strained electrical devices based on chemically synthesized SCNWs provide no mechanism to maintain the elastic deformation after relieving the external loads.
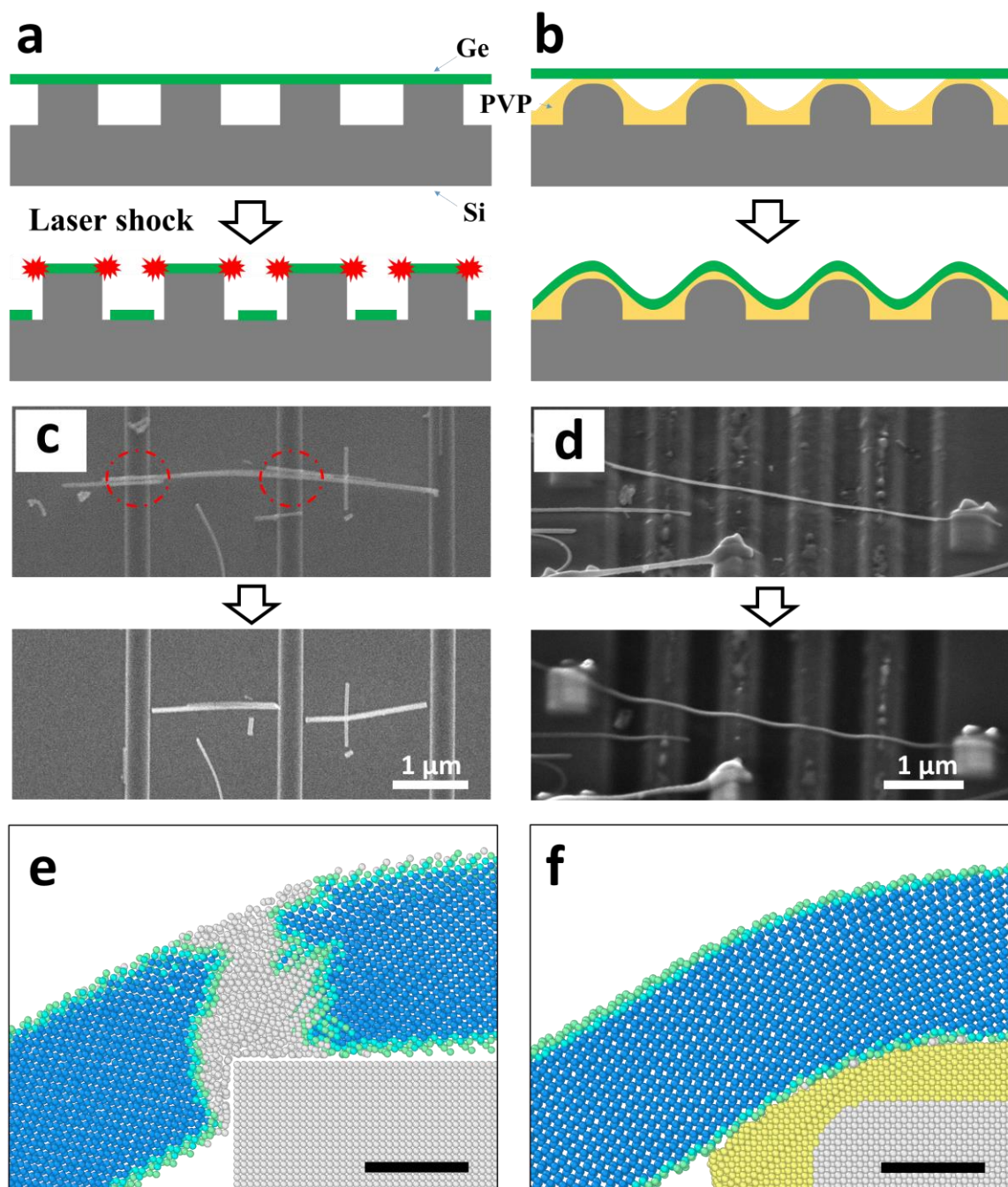
6.3 (a) Schematic of GeNWs failures at geometrical sharp corners of silicon mold. (b) Schematic of LSES of GeNWs with smoothed mold corners. (c) and (d) are corresponding SEM images of (a) and (b), respectively. (e) Molecular dynamics simulations of (c), showing amorphization of GeNW (white area) at sharp corners due to stress concentration. (f) MD simulation of deformation with self-smoothed mold corner by applying deformable materials as cushion (PVP). Scale bars for: (c-d)1 μm, (e-f) 3 nm.

Interaction between the SCNWs and 3D nanostructured substrates: The deformation behavior of the shocked SCNWs in LSES strongly depends on their contacts with mold surfaces. When directly shocking SCNWs on silicon or silicon dioxide surfaces, their "hard" contacts, especially those at the structural edges, can result in failures. Silicon molds fabricated through wet/dry etching are typically with atomically sharp edges, which would result in giant stress concentrations and damages to the brittle nanowires. Although the laser pressure used is less than 1 GPa, which is lower than the strength of the GeNWs, the stress concentration effect at the point or line contacts, results in much larger localized stress, irreversible plastic deformations (amorphization) and shear-stress induced cracks, as shown in Figure 6.3 and Figure 6.4. Highly localized elastic strains in a nanowire before its failure, if any, are difficult to control. The strains are relaxed once the SCNWs are broken. In the LSES approach, we tackle this problem by employing polymer cushioning and mold edge rounding. The deformation interlayer between GeNWs and the "hard" silicon substrate, e.g. the polymer cushion, creates an opportunity for soft landing of the GeNWs (Figure 6.4). It provides a self-smoothing mechanism of the sharp geometries and could dynamically accommodate stress distributions. We also fabricate rounded edges by appropriate adjusting electron/ion beam parameters and thermal annealing. A wavy GeNW strained on a round trench could be obtained after laser shock. By pinning the nanowire with deposited metals, we demonstrate that the process is not due to sliding of the nanowire at mold surface, and an obvious length elongation is observed.
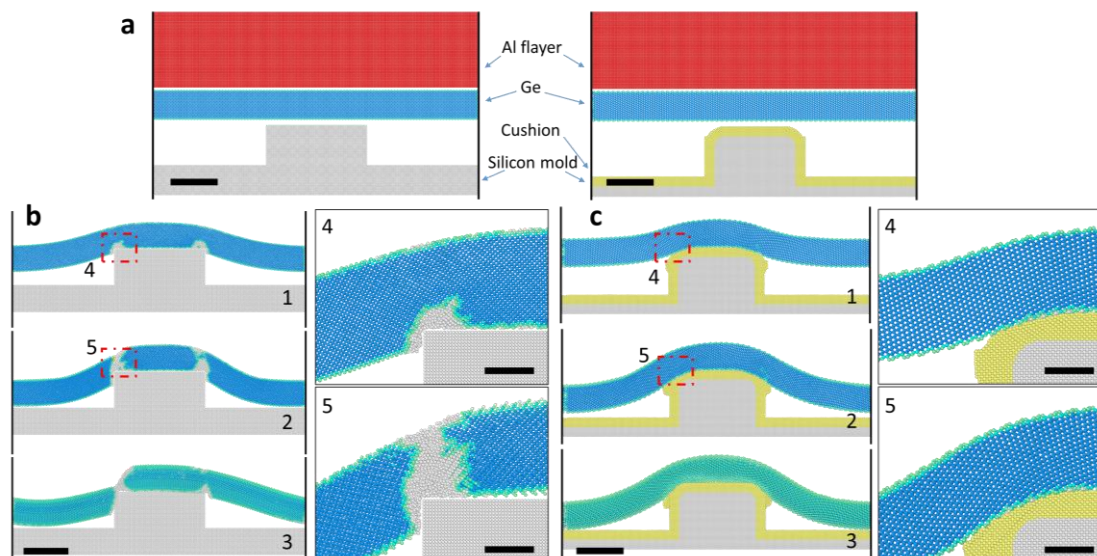
6.4 (a) Molecular dynamics simulation setup of laser shock shaping of GeNWs with sharp and smoothed mold corners. (b) Evolution of the GeNW morphologies and its amorpholization (white areas) at different time steps. ((1): 75 fs; (2): 125 fs; (3): 500 fs. (4) and (5) are the zoom-in atomic images of (1) and (2), respectively.) (c) The same as (b) but deformed with self-smoothed mold corner by applying deformable materials as cushion (PVP). Scale bars: 10 nm (a), (b1-b3), and (c1-c3); and 3 nm (b4-b5) and (c4-c5).

Molecular dynamics simulations are used to interpret the observed effects of edge sharpness and polymer cushion, as shown in Figure 6.5. Although the laser pressure used is less than 1 GPa and lower than the strength of the GeNWs, the stress concentration rises at point and line contacts upon contacting with a "hard" silicon substrate, resulting in much larger localized stress and irreversible plastic deformations. During our simulation, we have noticed at the point contact, amorpholization and shear-stress induced cracking of the GeNWs take place. A deformation interlayer between GeNWs and the "hard" silicon substrate, e.g. the polymer cushion used in our approach, creates an opportunity for soft landing of the GeNWs. It provides a self-smoothing mechanism of the sharp geometries and could dynamically accommodate stress distributions.
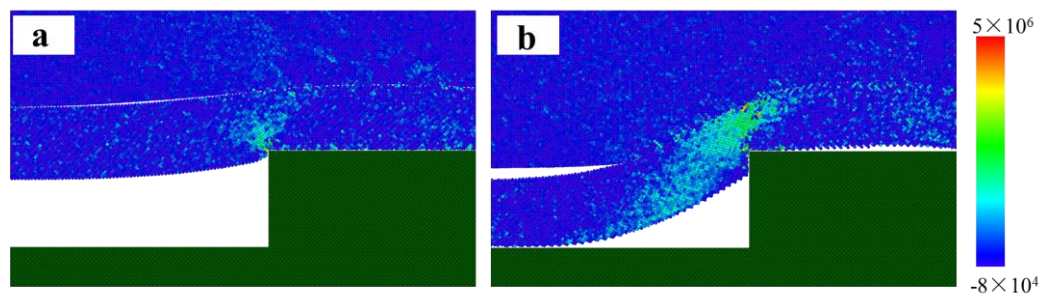
Figure 6.5 In-plane shear stress concentration due to sharp mold corners.
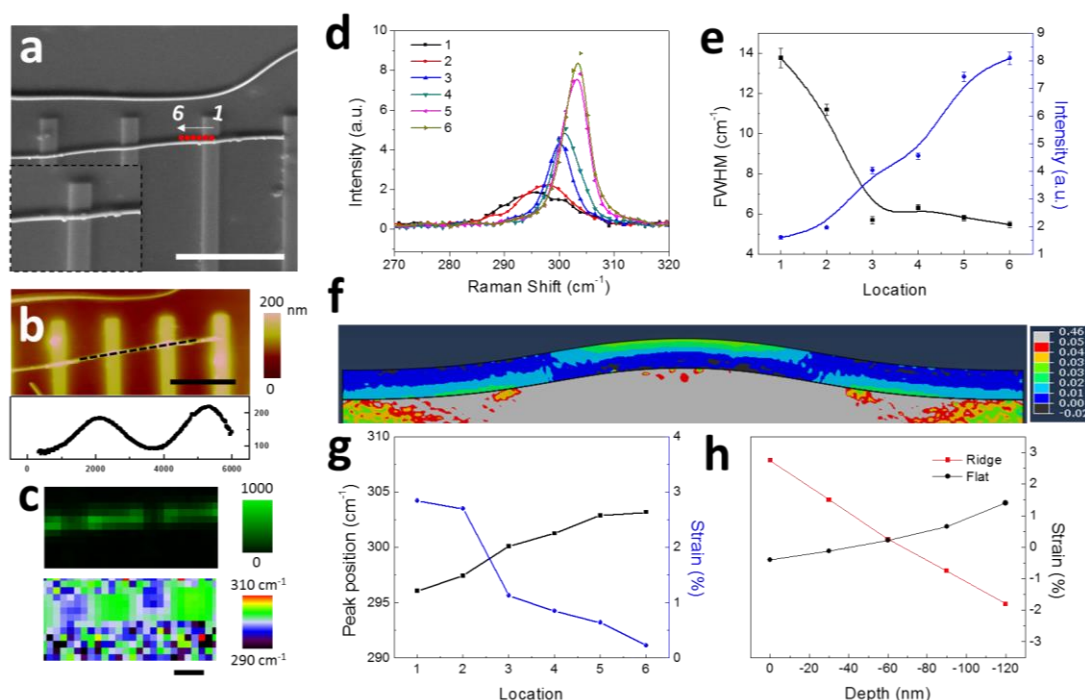
6.5 Raman spectroscopy characterization of strain distribution in shaped GeNWs. (a) SEM image of the GeNW investigated. (b) AFM height (upper) and line profile (lower) measurements of the nanowire. (c) Measured Raman intensity (upper) and peak position (lower) mapping. (d) Raman spectra from 270 cm^{-1} to 320 cm^{-1}. The positions are indicated in (a). (e) Measured Ge peak FWHM and intensities. (f) Simulated strain fields of the GeNW by FEM. (g) Plot of Raman peak shifts and calculated strains. (h) Strain variations along depth directions. Scale bars: (a) 4 μm, (b) 3 μm, (c) 1 μm.

Inhomogeneous elastic strains in GeNWs after 3D nanoshaping: To further confirm that the elastic nature of LSES and shed light on the strain distributions, spatially resolved Raman spectroscopy is employed with circularly polarized 532 nm excitation, a 100× objective lens with numerical aperture NA=0.85, and a fiber coupled grating spectrometer (2400 lines/mm). The laser intensity was kept sufficiently low to avoid heating effect.

Arrays of far-isolated ridges are designed for better strain visualization. The surface morphology of the nanowire investigated is shown in Figure 6.6. The obtained Raman spectra around the shaped nanowire, including the Ge peak intensities and peak positions. The silicon peaks are located at 520.1 cm^{-1} for all obtained spectra, while the Ge peaks are continuously blue-shifted from the ridge top to the trench center, indicating a spatially varied tensile strains. The Ge peak on the ridge is significantly broadened and has a decreased intensity, compared to the non-shaped nanowires. The observed peak shifts are compared with strain fields obtained through finite element modeling (FEM). The maximum peak shift of 7.1 cm^{-1} in this nanowire, corresponds to an average tensile strain of 2.4 % along [111] crystallographic directions within the circularly polarized laser spot[240–242]. The peak is also significantly broadened due to strain variations within the probed area, in both lateral and depth directions. Based on the AFM profiling and FEM modeling, we calculate the elastic strain at the ridge to be 2.8 %, which agrees well with the experimental data. Similar results are obtained on other strained GeNWs, demonstrating the elastic straining nature of the described LSES approach.
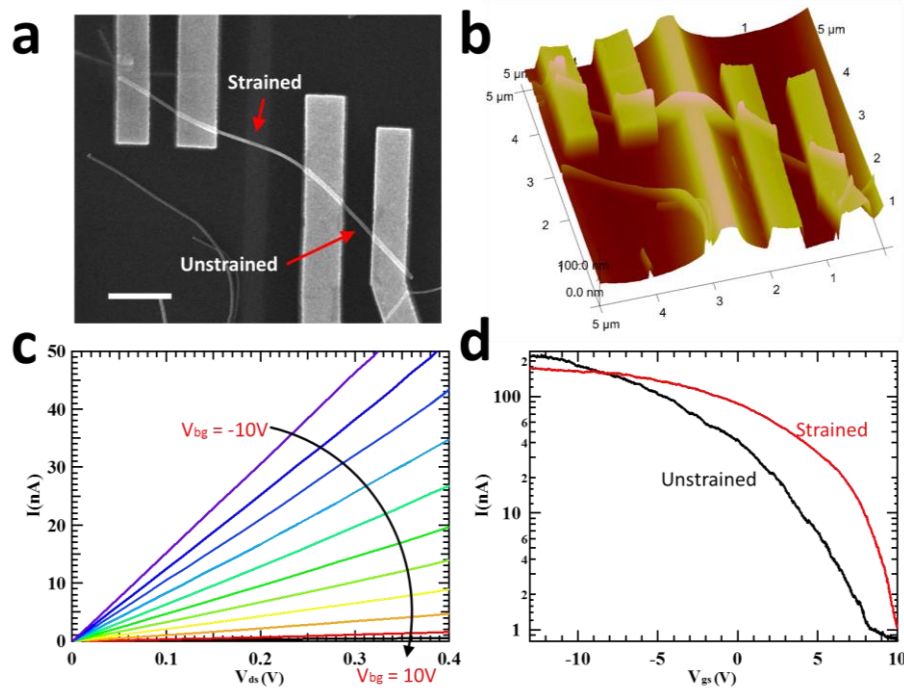
6.6 (a) SEM and (b) AFM imaging of the fabricated laser shock strained GeNW device. Scale bar: 1 µm. (c) Output characteristics and (d) transfer characteristics of the GeNW device. The strained area is at the proximity of the trench while the rest is unstrained. The channel length of the strained area is 1.4 µm while that of the unstrained area is 600 nm.

Laser shock induced straining effect on FET device performance: Unlike traditional straining techniques based on lattice mismatch, or polymer substrates stretching, LSES is versatile for applying controllable strains up to the strain limit of the material, and being compatible with current semiconductor technology. To shine light on the laser shock induced straining effect on FET device performance, the transfer and output characteristics of the strained and unstrained areas on the same NW are compared. As shown in Figure 6.7, a GeNW is placed across a trench which generates bending strain of the NW at its proximity. The field-effect mobility could be calculated by

$$\mu = \frac{dI_{DS}}{dV_{GS}} \times \frac{L^2}{C_e} \times \frac{1}{V_{DS}}$$

Eq. 6.1

Where I_{DS} is the source-drain current, V_{GS} the gate voltage, L the channel length, V_{DS} is source-drain voltage. Since PVP has approximately the same dielectric constant[237] with SiO_2, C_e the effect gate-capacitance is given by

$$C_e = \frac{2\pi\varepsilon_0\varepsilon L}{cosh^{-1}(\frac{R+t_e}{R})}$$

Eq. 6.2

Where t_e and ε are the effective thickness and the dielectric constant, respectively. $t_e \approx t_{ox} + t_p$. Where t_{ox} and t_p are the thickness of SiO_2 and PVP, respectively. The unstrained part has $t_{ox} = 90\ nm$, $t_p = 125\ nm$; for the strained part has $t_{ox} = 240\ nm$, $t_p = 100\ nm$. The mobility enhancement is determined by

$$\frac{\mu_s}{\mu_{us}} = \frac{\left(\frac{dI_{DS}}{dV_{GS}}\right)_s}{\left(\frac{dI_{DS}}{dV_{GS}}\right)_{us}} \cdot \frac{L_s}{L_{us}} \cdot \frac{(C_e)_{us}}{(C_e)_s} \qquad \text{Eq. 6.3}$$

The strain results in a 120% enhanced transconductance and 238% enhanced field-effect hole mobility, due to modification of the effective masses [243]. The device on/off ratio is also found to be decreased from 2.77×10^2 to 1.76×10^2, agreeing with the band gap shrinkage under the presence of both tensile and compressive strains. As the thicknesses of gate dielectrics for the strained and unstrained devices are different, the device performance could be further boosted by adopting conformal top gating. In principle, the strain fields of the SCNWs could be designed by adjusting laser parameters and mold geometries, yielding tunable band structure engineering, the details of which are beyond the scope of the current work and leave large room for future device performance optimization.

6.4 Deformation of graphene-copper hybrid structures
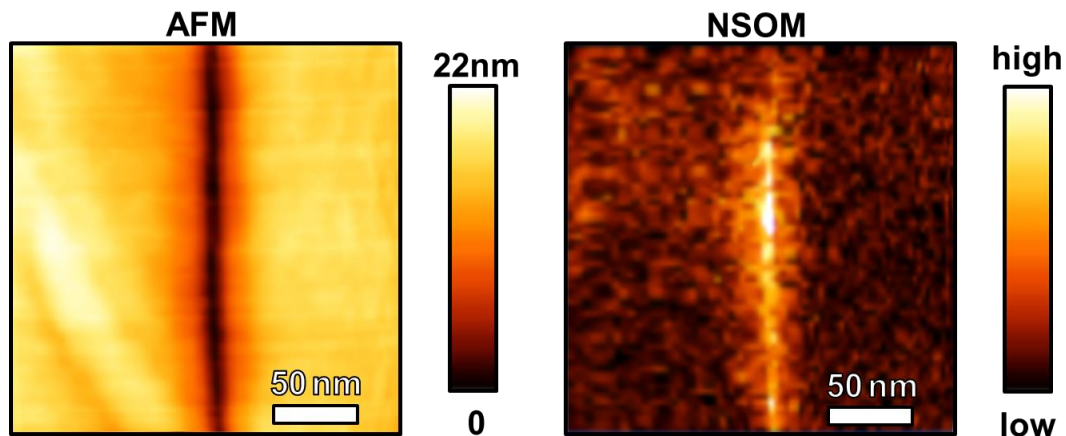
6.7 AFM image of a graphene-Cu nanogap after LSI, and NSOM measurement of local field.

Besides one-dimensional nanowires, various two-dimensional crystals have also been demonstrated to be deformable under laser shock. Figure 6.8 shows laser shock

deformation of graphene-copper hybrid structure. Parallel ultrafine nanogaps are instantaneously formed during the process. The local field is probed using a near-field scanning optical microscope (NSOM) (Figure 6.8). As shown in the NSOM image, a high-intensity region has been detected at the center of the nanogap with laser excitation wavelength 633 nm. Because of the resolution limit of the NSOM tip, the two hot spots located at the structural corners are merged during the experiment, resulting in a single high-intensity slit. Graphene can be strained without breaking under certain conditions.
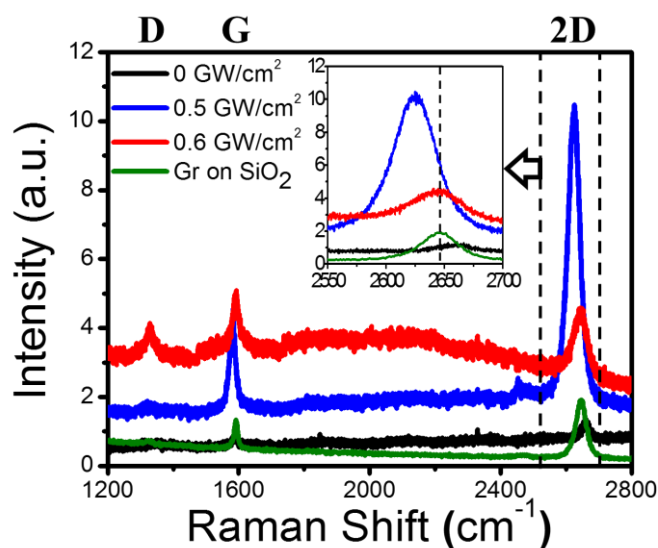
6.8 Raman spectrum of graphene on SiO2, graphene on Cu and nanopatterned graphene-Cu structures by LSI.

The strainability of graphene by deforming to 3D nanoscale surface has been studied. Figure 6.9 shows the Raman spectrum of the graphene-Cu thin film after LSI under several laser conditions. When the laser intensity is larger than 0.6 GW/cm^2, graphene will be cut into nanogaps (Figure 6.9). The Raman spectrum shows that D peak (related to defect level) is high, while G peak is not shifted relative to that in the unstrained graphene, since strain is released after cut. When the laser intensity is less than 0.5 GW/cm^2, the graphene is continuous and conformal on nanoshaped Cu. This is indicated in the Raman spectrum where the D peak is low and the G peak is shifted to the left because of tensile straining.
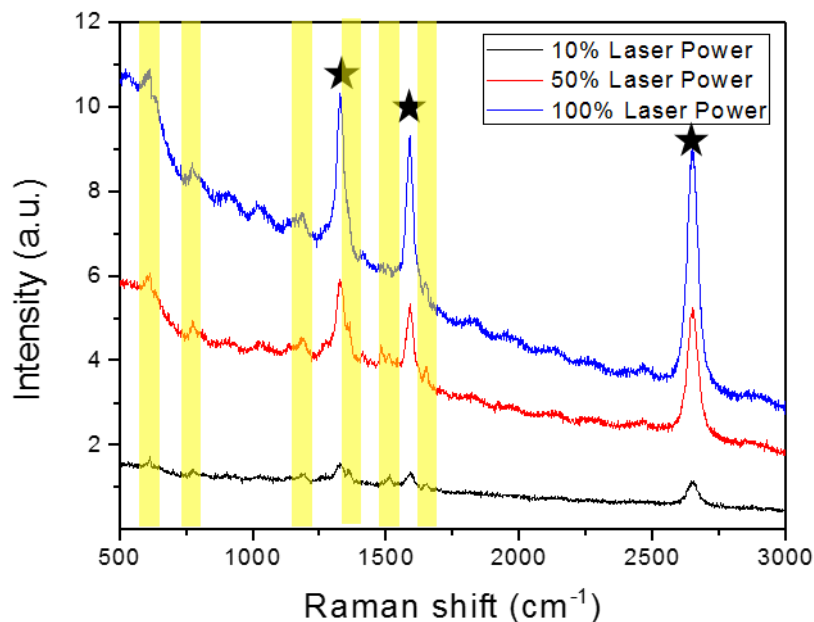
6.9 Molecular sensing of R6G on graphene-Cu nanostructures.

The formed hybrid system has potential applications in serving as molecular sensing platform. To this end, the sample is soaked in low-concentration R6G aquatic solution for 30 min, followed by complete DI water rinsing and naturally drying. The detect laser power is kept low to avoid apparent heating of the samples and photocarbonization of the molecules. As the copper film gets punched into nano-holes or nano-trenches with scalable dimensions, graphene is conformally deformed, streched and factured at its maximum strains. The photoluminescence background of the system is found to have around 100-fold increase. D peak signature of the imprinted graphene is found to be most significant and it results from new graphene edge formation. Some residual strains of graphene are detected as the G peak gets split.[41] The broken graphene edge which has high tendency in reacting with bio-molecules is located at sharp corners and coincides with the plasmonic hot spots. Thus the hybrid system could result in high sensitivity and selectivity of the target molecules. As shown in Figure 6.10, vibrational fingerprints of molecules at 613, 775, 1187, 1360, 1509 and 1650 cm^{-1} could be distinguished when it is detected on top of nano-trenches, a significance difference compared to the background copper flat surface. As the laser intensity keeps increasing after low intensity measurements, these fingerprints are still distinguishable which accounts to high thermal conductivity of graphene and its protection over photo-damage of the molecules.

The graphene-copper hybrid system, which is fabricated through one step of thickness reduction and another step of laser shock pressure processing, is the first report on having graphene and copper nanostructures at the same time. The simplicity of the fabrication process, the economy and availability of the materials used make it potential for mass and roll-to-roll production. This process opens new avenues for the fabrication of graphene micro/nano-ribbons.

6.5   Summary

In conclusion, we have demonstrated for the first time that brittle SCNWs can be nano-shaped at ultra-high strain rate in an ultrafast and controllable manner. This method utilizes laser-induced shock loading to deform SCNWs onto 3D-nanostructured silicon substrates with a cushioning polymer dielectric nano-layer, resulting in storage of elastic strains in SCNWs without dislocations or cracks. The elastic straining achieved by LSES is self-preserved and CMOS-compatible. The elastic strains of GeNWs are experimentally investigated by spatially resolved Raman spectroscopy and TEM, and confirmed by numerical simulations at both atomic and continuum-mechanics scales. As a result of 3D straining, the inhomogeneous elastic strains in GeNWs results in notable Raman peak shifts and broadening, which bring more tunability of electrical-optical property in SCNWs than traditional strain engineering. Nanowire FETs are fabricated with LSES treated GeNWs, and it is found to yield significantly enhanced hole mobilities and modulated on/off ratios. Hybrid systems of graphene and metallic nanostructures are demonstrated with this technique. This laser-based nanoshaping technique is versatile and suitable for variety of semiconductor nanowires and other 1D nano-structures and 2D crystals. The findings in this study would potentially bring many breakthroughs in future, as it provides a clean technology for band engineering of various materials for large-scale applications.

7. CONCLUSION AND FUTURE WORK

7.1   Conclusions

In this dissertation, laser shock imprinting is developed as a top-down method for the fabrication and modification of metallic nanoarrays, and deformation of low-dimensional materials. Precise control over structural dimensions, ultrafast processing (nanosecond processing time), capability of roll-to-roll mass production at economic cost and in scalable manner are some of the attributes of this emerging technology. Both continuum models and molecular dynamics modeling are applied to investigate the stress wave propagation and temperature rise. Hybrid film treated by LSI shows improved surface smoothness, better interface and enhanced mechanical integrity for robust use. Patterned gold nanostructures act as an excellent optical antenna and results in strong optical field confinement, which have aptly been exploited for sensitive molecular detection. Cold processing nature of LSI would suit to precision nanomanufacturing of functional structures on a variety of flexible substrates and thereby would find bio-applications.

The application of laser shock in post-fabrication processing of metallic nanostructures results in ultrafine and tunable nanogaps. The momentum transfer layer has significant effects on the plastic deformation and gap formation of the nanostructure arrays. Under laser shock with a rigid MTL, the microstructures change from crystalline to liquid-like metals, expand at high speed and hit each other, resulting with shrinking and fusion of the gaps. When a deformable MTL is used, its interactive and collaborative superplastic forming with targeted metallic nanoarrays generates self-limited gap shrinking and an ultrafine line-gap forms. This ultrafast opto-mechanical method can be used to tune the geometries of various metallic nanostructures. The process enables the tuning of the surface plasmon resonances of nanoantennas and boosts the performance of their applications in surface enhanced Raman scattering. The nanodimers after LST show red-shifts of their plasmonic resonances and emergences of additional peaks due to enhanced light confinement.

Laser shock nano-shaping of one-dimensional brittle SCNWs at ultra-high strain rate is demonstrated in an ultrafast and controllable manner. The application of laser-induced shock wave yields the deformation of SCNWs onto 3D-nanostructured silicon substrates with a cushioning polymer dielectric nano-layer, resulting in storage of elastic strains in SCNWs without dislocations or cracks. The elastic straining achieved is self-preserved and CMOS-compatible. The elastic strains of GeNWs are experimentally investigated by spatially resolved Raman spectroscopy and TEM, and confirmed by numerical simulations at both atomic and continuum-mechanics scales. As a result of 3D straining, the inhomogeneous elastic strains in GeNWs results in notable Raman peak shifts and broadening, which bring tunability of electrical-optical property in SCNWs than traditional strain engineering. Nanowire FETs are fabricated with LSES treated GeNWs, and it is found to yield significantly enhanced hole mobilities and modulated on/off ratios. This laser-based nanoshaping technique is versatile and suitable for variety of semiconductor nanowires and other 1D nano-structures. The findings in this study would potentially bring many breakthroughs in future, as it provides a clean technology for band engineering of SCNWs for large-scale applications.

7.2 Future works

It has been demonstrated throughout this study that laser shock could be effectively applied to fabricate and manipulate metallic nanostructures, one-dimensional and two-dimensional materials, which could significantly change their physical properties. Patterning of CVD grown 2D crystals such as graphene on metallic free-standing films have showed remarkable coupling effect. Straining effect of 2D crystals after laser hybrid processing is anticipated to result in changes of the electrical properties and band-gap opening. Further development is needed in order to (1) measure electrical properties by fabricating Field-effect transistors; (2) quantify band-gap opening by Scanning Tunneling Microscope; (3) probe local optical and physical properties in hybrid 2D crystal - metal nanostructures; (4) seek for simplified and realistic implementation of laser shock technique in processing of 2D crystals to benefit the society.

REFERENCES

(1)   Chung, J.; Ko, S.; Bieri, N. R.; Grigoropoulos, C. P.; Poulikakos, D. Conductor Microstructures by Laser Curing of Printed Gold Nanoparticle Ink. *Appl. Phys. Lett.* **2004**, *84*, 801–803.

(2)   Ko, S. H.; Pan, H.; Grigoropoulos, C. P.; Luscombe, C. K.; Fréchet, J. M. J.; Poulikakos, D. All-Inkjet-Printed Flexible Electronics Fabrication on a Polymer Substrate by Low-Temperature High-Resolution Selective Laser Sintering of Metal Nanoparticles. *Nanotechnology* **2007**, *18*, 345202.

(3)   Garnett, E. C.; Cai, W.; Cha, J. J.; Mahmood, F.; Connor, S. T.; Greyson Christoforo, M.; Cui, Y.; McGehee, M. D.; Brongersma, M. L. Self-Limited Plasmonic Welding of Silver Nanowire Junctions. *Nat. Mater.* **2012**, *11*, 241–249.

(4)   Cao, X.; Jahazi, M.; Immarigeon, J. P.; Wallace, W. A Review of Laser Welding Techniques for Magnesium Alloys. *J. Mater. Process. Technol.* **2006**, *171*, 188–204.

(5)   Benyounis, K. Y.; Olabi, a. G.; Hashmi, M. S. J. Effect of Laser Welding Parameters on the Heat Input and Weld-Bead Profile. *J. Mater. Process. Technol.* **2005**, *164-165*, 978–985.

(6)   Montross, C. S.; Wei, T.; Ye, L.; Clark, G.; Mai, Y. Laser Shock Processing and Its Effects on Microstructure and Properties of Metal Alloys : A Review. **2006**, *24*, 1021–1036.

(7)   Zhang, W.; Yao, Y. L. Micro Scale Laser Shock Processing of Metallic Components. *J. Manuf. Sci. Eng.* **2002**, *124*, 369–378.

(8)   Ye, C.; Suslov, S.; Kim, B. J.; Stach, E. a.; Cheng, G. J. Fatigue Performance Improvement in AISI 4140 Steel by Dynamic Strain Aging and Dynamic Precipitation during Warm Laser Shock Peening. *Acta Mater.* **2011**, *59*, 1014–1025.

(9)   Thompson, S. E.; Parthasarathy, S. Moore's Law: The Future of Si Microelectronics. *Mater. Today* **2006**, *9*, 20–25.

(10)   Li, J.; Liao, Y.; Suslov, S.; Cheng, G. J. Laser Shock-Based Platform for Controllable Forming of Nanowires. *Nano Lett.* **2012**, *12*, 3224–3230.

(11)   Li, J.; Chung, T. F.; Chen, Y. P.; Cheng, G. J. Nanoscale Strainability of Graphene by Laser Shock-Induced Three-Dimensional Shaping. *Nano Lett.* **2012**, *12*, 4577–4583.

(12)   Li, J.; Zhang, R. J.; Jiang, H. Q.; Cheng, G. J. Scalable Nano-Patterning of Graphenes Using Laser Shock. *Nanotechnology* **2011**, *22*, 475303.

(13)   Yang, Y.; Zhang, M. Y.; Cheng, G. J. Dense and Uniform Au Nanospheres on Glass through Confined Nanosecond Pulsed Laser Irradiation. *Appl. Phys. Lett.* **2011**, *99*, 091901.

(14)   Liu, Z.; Wang, Y.; Liao, Y.; Cheng, G. J. Direction-Tunable Nanotwins in Copper Nanowires by Laser-Assisted Electrochemical Deposition. *Nanotechnology* **2012**, *23*, 125602.

(15)   Narayan, R.; Goering, P. Laser Micro- and Nanofabrication of Biomaterials. *MRS Bull.* **2011**, *36*, 973–982.

(16)   Gao, H.; Cheng, G. J. 3D Microscale Laser Dynamic Forming: Multiscale Modeling and Experimental Validation. *J. Appl. Phys.* **2011**, *109*.

(17)   Park, J. B.; Xiong, W.; Gao, Y.; Qian, M.; Xie, Z. Q.; Mitchell, M.; Zhou, Y. S.; Han, G. H.; Jiang, L.; Lu, Y. F. Fast Growth of Graphene Patterns by Laser Direct Writing. *Appl. Phys. Lett.* **2011**, *98*, 9–12.

(18)   Jiang, L.; Liu, P.; Yan, X.; Leng, N.; Xu, C.; Xiao, H.; Lu, Y. High-Throughput Rear-Surface Drilling of Microchannels in Glass Based on Electron Dynamics Control Using Femtosecond Pulse Trains. *Opt. Lett.* **2012**, *37*, 2781.

(19)   Yu, C.; Gao, H.; Yu, H.; Jiang, H.; Cheng, G. J. Laser Dynamic Forming of Functional Materials Laminated Composites on Patterned Three-Dimensional Surfaces with Applications on Flexible Microelectromechanical Systems. *Appl. Phys. Lett.* **2009**, *95*, 091108.

(20)   Peyre, P.; Fabbro, R.; Merrien, P.; Lieurade, H. P. Laser Shock Processing of Aluminium Alloys. Application to High Cycle Fatigue Behaviour. *Mater. Sci. Eng. A* **1996**, *210*, 102–113.

(21)   Lee, J.-H.; Veysset, D.; Singer, J. P.; Retsch, M.; Saini, G.; Pezeril, T.; Nelson, K. a; Thomas, E. L. High Strain Rate Deformation of Layered Nanocomposites. *Nat. Commun.* **2012**, *3*, 1164.

(22)   Ki, H.; Mazumder, J.; Mohanty, P. S. Modeling of Laser Keyhole Welding: Part II. Simulation of Keyhole Evolution, Velocity, Temperature Profile, and Experimental Verification. *Metall. Mater. Trans. A* **2002**, *33*, 1831–1842.

(23)   Ki, H.; Mazumder, J.; Mohanty, P. S. Modeling of Laser Keyhole Welding: Part I. Mathematical Modeling, Numerical Methodology, Role of Recoil Pressure, Multiple Reflections, and Free Surface Evolution. *Metall. Mater. Trans. A* **2002**, *33*, 1817–1830.

(24)   Tan, W.; Shin, Y. C. Multi-Scale Modeling of Solidification and Microstructure Development in Laser Keyhole Welding Process for Austenitic Stainless Steel. *Comput. Mater. Sci.* **2015**, *98*, 446–458.

(25)   Hu, Y.; He, X.; Yu, G.; Zhao, S. Capillary Convection in Pulsed - Butt Welding of Miscible Dissimilar Couple. *Proc. Inst. Mech. Eng. Part C J. Mech. Eng. Sci.* **2016**, *0*, 1–12.

(26)   Hu, Y.; He, X.; Yu, G.; Ge, Z.; Zheng, C.; Ning, W. Heat and Mass Transfer in Laser Dissimilar Welding of Stainless Steel and Nickel. *Appl. Surf. Sci.* **2012**, *258*, 5914–5922.

(27)   Lin, D.; Ye, C.; Liao, Y.; Suslov, S.; Liu, R.; Cheng, G. J. Mechanism of Fatigue Performance Enhancement in a Laser Sintered Superhard Nanoparticles Reinforced Nanocomposite Followed by Laser Shock Peening. *J. Appl. Phys.* **2013**, *113*.

(28)   Ye, C.; Suslov, S.; Kim, B. J.; Stach, E. a.; Cheng, G. J. Fatigue Performance Improvement in AISI 4140 Steel by Dynamic Strain Aging and Dynamic Precipitation during Warm Laser Shock Peening. *Acta Mater.* **2011**, *59*, 1014–1025.

(29)   Liao, Y.; Ye, C.; Gao, H.; Kim, B.-J.; Suslov, S.; Stach, E. a.; Cheng, G. J. Dislocation Pinning Effects Induced by Nano-Precipitates during Warm Laser Shock Peening: Dislocation Dynamic Simulation and Experiments. *J. Appl. Phys.* **2011**, *110*, 023518.

(30)   Fabbro, R.; Fournier, J.; Ballard, P.; Devaux, D.; Virmont, J. Physical Study of Laser-Produced Plasma in Confined Geometry. *J. Appl. Phys.* **1990**, *68*, 775–784.

(31)   Gao, H.; Ye, C.; Cheng, G. J. Deformation Behaviors and Critical Parameters in Microscale Laser Dynamic Forming. *J. Manuf. Sci. Eng.* **2009**, *131*, 051011.

(32)   Liao, Y.; Suslov, S.; Ye, C.; Cheng, G. J. The Mechanisms of Thermal Engineered Laser Shock Peening for Enhanced Fatigue Performance. *Acta Mater.* **2012**, *60*, 4997–5009.

(33)   Ye, C.; Suslov, S.; Lin, D.; Cheng, G. J. Deformation-Induced Martensite and Nanotwins by Cryogenic Laser Shock Peening of AISI 304 Stainless Steel and the Effects on Mechanical Properties. *Philosophical Magazine*, 2012, *92*, 1369–1389.

(34)   Liao, Y.; Yang, Y.; Cheng, G. J. Enhanced Laser Shock by an Active Liquid Confinement—Hydrogen Peroxide. *J. Manuf. Sci. Eng.* **2012**, *134*, 034503.

(35)   Gao, H.; Ye, C.; Cheng, G. J. Deformation Behaviors and Critical Parameters in Microscale Laser Dynamic Forming. *J. Manuf. Sci. Eng.* **2009**, *131*, 051011.

(36) Ye, C.; Cheng, G. J. Effects of Temperature on Laser Shock Induced Plastic Deformation: The Case of Copper. *J. Manuf. Sci. Eng.* **2010**, *132*, 061009.

(37) Aouani, H.; Rahmani, M.; Navarro-Cía, M.; Maier, S. a. Third-Harmonic-Upconversion Enhancement from a Single Semiconductor Nanoparticle Coupled to a Plasmonic Antenna. *Nat. Nanotechnol.* **2014**, *9*, 290–294.

(38) Ding, W.; Zhou, L.; Chou, S. Y. Enhancement and Electric Charge Assisted Tuning of Nonlinear Light Generation in Bipolar Plasmonics. *Nano Lett.* **2014**.

(39) Van Nieuwstadt, J.; Sandtke, M.; Harmsen, R.; Segerink, F.; Prangsma, J.; Enoch, S.; Kuipers, L. Strong Modification of the Nonlinear Optical Response of Metallic Subwavelength Hole Arrays. *Phys. Rev. Lett.* **2006**, *97*, 146102.

(40) Watanabe, K.; Menzel, D.; Nilius, N.; Freund, H.-J. Photochemistry on Metal Nanoparticles. *Chem. Rev.* **2006**, *106*, 4301–4320.

(41) Heeg, S.; Fernandez-Garcia, R.; Oikonomou, A.; Schedin, F.; Narula, R.; Maier, S. a; Vijayaraghavan, A.; Reich, S. Polarized Plasmonic Enhancement by Au Nanostructures Probed through Raman Scattering of Suspended Graphene. *Nano Lett.* **2013**, *13*, 301–308.

(42) Pieczonka, N. P. W.; Aroca, R. F. Single Molecule Analysis by Surfaced-Enhanced Raman Scattering. *Chem. Soc. Rev.* **2008**, *37*, 946–954.

(43) Zhang, R.; Zhang, Y.; Dong, Z. C.; Jiang, S.; Zhang, C.; Chen, L. G.; Zhang, L.; Liao, Y.; Aizpurua, J.; Luo, Y.; *et al.* Chemical Mapping of a Single Molecule by Plasmon-Enhanced Raman Scattering. *Nature* **2013**, *498*, 82–86.

(44) Wu, H.-Y.; Choi, C. J.; Cunningham, B. T. Plasmonic Nanogap-Enhanced Raman Scattering Using a Resonant Nanodome Array. *Small* **2012**, *8*, 2878–2885.

(45) Yokota, Y.; Ueno, K.; Misawa, H. Highly Controlled Surface-Enhanced Raman Scattering Chips Using Nanoengineered Gold Blocks. *Small* **2011**, *7*, 252–258.

(46) Hu, Y.; Lee, S.; Kumar, P.; Nian, Q.; Wang, W.; Irudayaraj, J.; Cheng, G. J. Water Flattens Graphene Wrinkles: Laser Shock Wrapping of Graphene onto Substrate-Supported Crystalline Plasmonic Nanoparticle Arrays. *Nanoscale* **2015**, *7*, 19885–19893.

(47) Lee, S.; Kumar, P.; Hu, Y.; Cheng, G. J.; Irudayaraj, J. Graphene Laminated Gold Bipyramids as Sensitive Detection Platforms for Antibiotic Molecules. *Chem. Commun.* **2015**, *51*, 15494–15497.

(48)   Wang, K.; Schonbrun, E.; Steinvurzel, P.; Crozier, K. B. Trapping and Rotating Nanoparticles Using a Plasmonic Nano-Tweezer with an Integrated Heat Sink. *Nat. Commun.* **2011**, *2*, 469.

(49)   Juan, M. L.; Righini, M.; Quidant, R. Plasmon Nano-Optical Tweezers. *Nat. Photonics* **2011**, *5*, 349–356.

(50)   Echtermeyer, T. J.; Britnell, L.; Jasnos, P. K.; Lombardo, a; Gorbachev, R. V; Grigorenko, a N.; Geim, a K.; Ferrari, a C.; Novoselov, K. S. Strong Plasmonic Enhancement of Photovoltage in Graphene. *Nat. Commun.* **2011**, *2*, 458.

(51)   Atwater, H. a; Polman, A. Plasmonics for Improved Photovoltaic Devices. *Nat. Mater.* **2010**, *9*, 205–213.

(52)   Diukman, I.; Tzabari, L.; Berkovitch, N.; Tessler, N.; Orenstein, M. Controlling Absorption Enhancement in Organic Photovoltaic Cells by Patterning Au Nano Disks within the Active Layer. *Opt. Express* **2011**, *19 Suppl 1*, A64–A71.

(53)   Berry, C. W.; Wang, N.; Hashemi, M. R.; Unlu, M.; Jarrahi, M. Significant Performance Enhancement in Photoconductive Terahertz Optoelectronics by Incorporating Plasmonic Contact Electrodes. *Nat. Commun.* **2013**, *4*, 1622.

(54)   Renger, J.; Quidant, R.; van Hulst, N.; Novotny, L. Surface-Enhanced Nonlinear Four-Wave Mixing. *Phys. Rev. Lett.* **2010**, *104*, 046803.

(55)   Chirumamilla, M.; Toma, A.; Gopalakrishnan, A.; Das, G.; Zaccaria, R. P.; Krahne, R.; Rondanina, E.; Leoncini, M.; Liberale, C.; De Angelis, F.; *et al.* 3D Nanostar Dimers with a Sub-10-Nm Gap for Single-/Few-Molecule Surface-Enhanced Raman Scattering. *Adv. Mater.* **2014**, *26*, 2353–2358.

(56)   Hu, M.; Ou, F. S.; Wu, W.; Naumov, I.; Li, X.; Bratkovsky, A. M.; Williams, R. S.; Li, Z. Gold Nanofingers for Molecule Trapping and Detection. *J. Am. Chem. Soc.* **2010**, *132*, 12820–12822.

(57)   Kravets, V. G.; Schedin, F.; Jalil, R.; Britnell, L.; Gorbachev, R. V; Ansell, D.; Thackray, B.; Novoselov, K. S.; Geim, a K.; Kabashin, a V; *et al.* Singular Phase Nano-Optics in Plasmonic Metamaterials for Label-Free Single-Molecule Detection. *Nat. Mater.* **2013**, *12*, 304–309.

(58)   Oulton, R. F.; Sorger, V. J.; Zentgraf, T.; Ma, R.-M.; Gladden, C.; Dai, L.; Bartal, G.; Zhang, X. Plasmon Lasers at Deep Subwavelength Scale. *Nature* **2009**, *461*, 629–632.

(59)   Akimov, a V; Mukherjee, a; Yu, C. L.; Chang, D. E.; Zibrov, a S.; Hemmer, P. R.; Park, H.; Lukin, M. D. Generation of Single Optical Plasmons in Metallic Nanowires Coupled to Quantum Dots. *Nature* **2007**, *450*, 402–406.

(60) Lee, S.; Hahm, M. G.; Vajtai, R.; Hashim, D. P.; Thurakitseree, T.; Chipara, A. C.; Ajayan, P. M.; Hafner, J. H. Utilizing 3D SERS Active Volumes in Aligned Carbon Nanotube Scaffold Substrates. *Adv. Mater.* **2012**, *24*, 5261–5266.

(61) BoáMogensen, K.; Palanco, M. Surface-Enhanced Raman Scattering on Aluminum Using near Infrared and Visible Excitation. *Chem. Commun.* **2014**.

(62) Gopinath, A.; Boriskina, S. V; Feng, N.-N.; Reinhard, B. M.; Dal Negro, L. Photonic-Plasmonic Scattering Resonances in Deterministic Aperiodic Structures. *Nano Lett.* **2008**, *8*, 2423–2431.

(63) Huang, J.-S.; Callegari, V.; Geisler, P.; Brüning, C.; Kern, J.; Prangsma, J. C.; Wu, X.; Feichtner, T.; Ziegler, J.; Weinmann, P.; *et al.* Atomically Flat Single-Crystalline Gold Nanostructures for Plasmonic Nanocircuitry. *Nat. Commun.* **2010**, *1*, 150.

(64) Qin, D.; Xia, Y.; Whitesides, G. M. Soft Lithography for Micro- and Nanoscale Patterning. *Nat. Protoc.* **2010**, *5*, 491–502.

(65) Cherukulappurath, S.; Johnson, T. W.; Lindquist, N. C.; Oh, S.-H. Template-Stripped Asymmetric Metallic Pyramids for Tunable Plasmonic Nanofocusing. *Nano Lett.* **2013**, *13*, 5635–5641.

(66) Lee, K.-L.; Chen, P.-W.; Wu, S.-H.; Huang, J.-B.; Yang, S.-Y.; Wei, P.-K. Enhancing Surface Plasmon Detection Using Template-Stripped Gold Nanoslit Arrays on Plastic Films. *ACS Nano* **2012**, *6*, 2931–2939.

(67) Lindquist, N. C.; Nagpal, P.; Lesuffleur, A.; Norris, D. J.; Oh, S.-H. Three-Dimensional Plasmonic Nanofocusing. *Nano Lett.* **2010**, *10*, 1369–1373.

(68) Nagpal, P.; Lindquist, N. C.; Oh, S.-H.; Norris, D. J. Ultrasmooth Patterned Metals for Plasmonics and Metamaterials. *Science* **2009**, *325*, 594–597.

(69) Geim, A. K.; Novoselov, K. S. The Rise of Graphene. *Nat. Mater.* **2007**, *6*, 183–191.

(70) Novoselov, K. S.; Geim, a K.; Morozov, S. V; Jiang, D.; Katsnelson, M. I.; Grigorieva, I. V; Dubonos, S. V; Firsov, a a. Two-Dimensional Gas of Massless Dirac Fermions in Graphene. *Nature* **2005**, *438*, 197–200.

(71) Lal, S.; Link, S.; Halas, N. J. Nano-Optics from Sensing to Waveguiding. *Nat. Photonics* **2007**, *1*, 641–648.

(72) Barnes, W.; Dereux, A.; Ebbesen, T. Surface Plasmon Subwavelength Optics. *Nature* **2003**, *424*, 824–830.

(73) Ozbay, E. Plasmonics: Merging Photonics and Electronics at Nanoscale Dimensions. *Science* **2006**, *311*, 189–193.

(74) Zhang, X.; Liu, Z. Superlenses to Overcome the Diffraction Limit. *Nat. Mater.* **2008**, *7*, 435–441.

(75) Stewart, M. E.; Anderton, C. R.; Thompson, L. B.; Maria, J.; Gray, S. K.; Rogers, J. a; Nuzzo, R. G. Nanostructured Plasmonic Sensors. *Chem. Rev.* **2008**, *108*, 494–521.

(76) Linic, S.; Christopher, P.; Ingram, D. B. Plasmonic-Metal Nanostructures for Efficient Conversion of Solar to Chemical Energy. *Nat. Mater.* **2011**, *10*, 911–921.

(77) Mu, Q.; Jiang, G.; Chen, L.; Zhou, H.; Fourches, D.; Tropsha, A.; Yan, B. Chemical Basis of Interactions Between Engineered Nanoparticles and Biological Systems. *Chem. Rev.* **2014**, *114*, 7740–7781.

(78) Hwang, S. W.; Shin, D. H.; Kim, C. O.; Hong, S. H.; Kim, M. C.; Kim, J.; Lim, K. Y.; Kim, S.; Choi, S. H.; Ahn, K. J.; *et al.* Plasmon-Enhanced Ultraviolet Photoluminescence from Hybrid Structures of graphene/ZnO Films. *Phys. Rev. Lett.* **2010**, *105*, 1–4.

(79) Zhang, W.; Lee, S.; McNear, K. L.; Chung, T. F.; Lee, S.; Lee, K.; Crist, S. a; Ratliff, T. L.; Zhong, Z.; Chen, Y. P.; *et al.* Use of Graphene as Protection Film in Biological Environments. *Sci. Rep.* **2014**, *4*, 4097.

(80) Prasai, D.; Tuberquia, J. C.; Harl, R. R.; Jennings, G. K.; Bolotin, K. I. Graphene: Corrosion-Inhibiting Coating. *ACS Nano* **2012**, *6*, 1102–1108.

(81) Wilson, P. M.; Zobel, A.; Lipatov, A.; Schubert, E.; Hofmann, T.; Sinitskii, A. Multilayer Graphitic Coatings for Thermal Stabilization of Metallic Nanostructures. *ACS Appl. Mater. Interfaces* **2015**, *7*, 2987–2992.

(82) Su, Y.; Kravets, V. G.; Wong, S. L.; Waters, J.; Geim, a. K.; Nair, R. R. Impermeable Barrier Films and Protective Coatings Based on Reduced Graphene Oxide. *Nat. Commun.* **2014**, *5*, 4843.

(83) Wang, P.; Liang, O.; Zhang, W.; Schroeder, T.; Xie, Y.-H. Ultra-Sensitive Graphene-Plasmonic Hybrid Platform for Label-Free Detection. *Adv. Mater.* **2013**, *25*, 4918–4924.

(84) Xu, W.; Ling, X.; Xiao, J.; Dresselhaus, M. S.; Kong, J.; Xu, H.; Liu, Z.; Zhang, J. Surface Enhanced Raman Spectroscopy on a Flat Graphene Surface. *Proc. Natl. Acad. Sci. U. S. A.* **2012**, *109*, 9281–9286.

(85)   Mehta, R.; Chugh, S.; Chen, Z. Enhanced Electrical and Thermal Conduction in Graphene-Encapsulated Copper Nanowires. *Nano Lett.* **2015**, 150206084313000.

(86)   Lee, J. S.; You, K. H.; Park, C. B. Highly Photoactive, Low Bandgap TiO2 Nanoparticles Wrapped by Graphene. *Adv. Mater.* **2012**, *24*, 1084–1088.

(87)   Wei, D.; Liang, J.; Zhu, Y.; Yuan, Z.; Li, N.; Qian, Y. Formation of Graphene-Wrapped Nanocrystals at Room Temperature through the Colloidal Coagulation Effect. *Part. Part. Syst. Charact.* **2013**, *30*, 143–147.

(88)   Chen, Y.; Guo, F.; Jachak, A.; Kim, S.-P.; Datta, D.; Liu, J.; Kulaots, I.; Vaslet, C.; Jang, H. D.; Huang, J.; *et al.* Aerosol Synthesis of Cargo-Filled Graphene Nanosacks. *Nano Lett.* **2012**, *12*, 1996–2002.

(89)   Luo, J.; Zhao, X.; Wu, J.; Jang, H. D.; Kung, H. H.; Huang, J. Crumpled Graphene-Encapsulated Si Nanoparticles for Lithium Ion Battery Anodes. *J. Phys. Chem. Lett.* **2012**, *3*, 1824–1829.

(90)   Xu, Y.; Yi, R.; Yuan, B.; Wu, X. High Capacity MoO2/graphite Oxide Composite Anode for Lithium-Ion Batteries. *J. Phys. Chem. Lett.* **2012**, *3*, 309–314.

(91)   Ma, R.; Lu, Z.; Wang, C.; Wang, H.-E.; Yang, S.; Xi, L.; Chung, J. C. Y. Large-Scale Fabrication of Graphene-Wrapped FeF3 Nanocrystals as Cathode Materials for Lithium Ion Batteries. *Nanoscale* **2013**, *5*, 6338–6343.

(92)   Jyothirmayee Aravind, S. S.; Ramaprabhu, S. Graphene Wrapped Multiwalled Carbon Nanotubes Dispersed Nanofluids for Heat Transfer Applications. *J. Appl. Phys.* **2012**, *112*, 124304.

(93)   Wang, H.; Yang, Y.; Liang, Y.; Robinson, J. T.; Li, Y.; Jackson, A. Graphene-Wrapped Sulfur Particles as a Rechargeable Lithium À Sulfur Battery Cathode Material with High Capacity and Cycling Stability. **2011**, 2644–2647.

(94)   Ahn, K.-S.; Seo, S.-W.; Park, J.-H.; Min, B.-K.; Jung, W.-S. The Preparation of Alumina Particles Wrapped in Few-Layer Graphene Sheets and Their Application to Dye-Sensitized Solar Cells. *Bull. Korean Chem. Soc.* **2011**, *32*, 1579–1582.

(95)   Shi, Y.; Chou, S.-L.; Wang, J.-Z.; Wexler, D.; Li, H.-J.; Liu, H.-K.; Wu, Y. Graphene Wrapped LiFePO4/C Composites as Cathode Materials for Li-Ion Batteries with Enhanced Rate Capability. *J. Mater. Chem.* **2012**, *22*, 16465.

(96)   Song, H. Y.; Geng, S. F.; An, M. R.; Zha, X. W. Atomic Simulation of the Formation and Mechanical Behavior of Carbon Nanoscrolls. *J. Appl. Phys.* **2013**, *113*.

(97)   Li, Y. F.; Yu, H. Q.; Li, H.; An, C. G.; Zhang, K.; Liew, K. M.; Liu, X. F. How Do Metal/graphene Self-Assemble into Core-Shelled Composite Nanostructures? *J. Phys. Chem. C* **2011**, *115*, 6229–6234.

(98)   Li, X.; Zhu, Y.; Cai, W.; Borysiak, M.; Han, B.; Chen, D.; Piner, R. D.; Colombo, L.; Ruoff, R. S. Transfer of Large-Area Graphene Films for High-Performance Transparent Conductive Electrodes. *Nano Lett.* **2009**, *9*, 4359–4363.

(99)   Liang, X.; Sperling, B. a; Calizo, I.; Cheng, G.; Hacker, C. A.; Zhang, Q.; Obeng, Y.; Yan, K.; Peng, H.; Li, Q.; *et al.* Toward Clean and Crackless Transfer of Graphene. *ACS Nano* **2011**, *5*, 9144–9153.

(100) Suk, J. W.; Kitt, A.; Magnuson, C. W.; Hao, Y.; Ahmed, S.; An, J.; Swan, A. K.; Goldberg, B. B.; Ruoff, R. S. Transfer of CVD-Grown Monolayer Graphene onto Arbitrary Substrates. *ACS Nano* **2011**, *5*, 6916–6924.

(101) Wang, D.-Y.; Huang, I.-S.; Ho, P.-H.; Li, S.-S.; Yeh, Y.-C.; Wang, D.-W.; Chen, W.-L.; Lee, Y.-Y.; Chang, Y.-M.; Chen, C.-C.; *et al.* Clean-Lifting Transfer of Large-Area Residual-Free Graphene Films. *Adv. Mater.* **2013**, *25*, 4521–4526.

(102) Meyer, J. C.; Geim, a K.; Katsnelson, M. I.; Novoselov, K. S.; Booth, T. J.; Roth, S. The Structure of Suspended Graphene Sheets. *Nature* **2007**, *446*, 60–63.

(103) Zhu, S.; Li, T. Wrinkling Instability of Graphene on Substrate-Supported Nanoparticles. *J. Appl. Mech.* **2014**, *81*, 061008.

(104) Zhou, Y.; Chen, Y.; Liu, B.; Yang, Z.; Hu, M.; Wang, S. Mechanics of Nanoscale Wrinkling of Graphene on a Non-Developable Spherical Surface. *Carbon N. Y.* **2014**, *84*, 263–271.

(105) Li, T. Extrinsic Morphology of Graphene. *Model. Simul. Mater. Sci. Eng.* **2011**, *19*, 054005.

(106) Bao, W.; Miao, F.; Chen, Z.; Zhang, H.; Jang, W.; Dames, C.; Lau, C. N. Controlled Ripple Texturing of Suspended Graphene and Ultrathin Graphite Membranes. *Nat. Nanotechnol.* **2009**, *4*, 562–566.

(107) Guinea, F.; Katsnelson, M. I.; Vozmediano, M. a H. Midgap States and Charge Inhomogeneities in Corrugated Graphene. *Phys. Rev. B - Condens. Matter Mater. Phys.* **2008**, *77*, 1–8.

(108) Guinea, F.; Horovitz, B.; Le Doussal, P. Gauge Field Induced by Ripples in Graphene. *Phys. Rev. B - Condens. Matter Mater. Phys.* **2008**, *77*, 1–8.

(109) Vázquez De Parga, a. L.; Calleja, F.; Borca, B.; Passeggi, M. C. G.; Hinarejos, J. J.; Guinea, F.; Miranda, R. Periodically Rippled Graphene: Growth and Spatially Resolved Electronic Structure. *Phys. Rev. Lett.* **2008**, *100*, 1–4.

(110) Klimov, N. N.; Jung, S.; Zhu, S.; Li, T.; Wright, C. a.; Solares, S. D.; Newell, D. B.; Zhitenev, N. B.; Stroscio, J. a. Electromechanical Properties of Graphene Drumheads. *Science (80-.).* **2012**, *336*, 1557–1561.

(111) Scharfenberg, S.; Mansukhani, N.; Chialvo, C.; Weaver, R. L.; Mason, N. Observation of a Snap-through Instability in Graphene. *Appl. Phys. Lett.* **2012**, *100*, 2010–2013.

(112) Wagner, T. J. W.; Vella, D. The Sensitivity of Graphene "Snap-through" to Substrate Geometry. *Appl. Phys. Lett.* **2012**, *100*.

(113) Boukhvalov, D. W.; Katsnelson, M. I. Enhancement of Chemical Activity in Corrugated Graphene. *J. Phys. Chem. C* **2009**, *113*, 14176–14178.

(114) Politano, A.; Chiarello, G. Periodically Rippled Graphene on Ru(0 0 0 1): A Template for Site-Selective Adsorption of Hydrogen Dimers via Water Splitting and Hydrogen-Spillover at Room Temperature. *Carbon N. Y.* **2013**, *61*, 412–417.

(115) Kimouche, A.; Renault, O.; Samaddar, S.; Winkelmann, C.; Courtois, H.; Fruchart, O.; Coraux, J. Modulating Charge Density and Inelastic Optical Response in Graphene by Atmospheric Pressure Localized Intercalation through Wrinkles. *Carbon N. Y.* **2014**, *68*, 73–79.

(116) Zhang, Y.; Fu, Q.; Cui, Y.; Mu, R.; Jin, L.; Bao, X. Enhanced Reactivity of Graphene Wrinkles and Their Function as Nanosized Gas Inlets for Reactions under Graphene. *Phys. Chem. Chem. Phys.* **2013**, *15*, 19042–19048.

(117) Talari, a. C. S.; Evans, C. a.; Holen, I.; Coleman, R. E.; Rehman, I. U. Raman Spectroscopic Analysis Differentiates between Breast Cancer Cell Lines. *J. Raman Spectrosc.* **2015**, *46*, 421–427.

(118) Oliver, W. C.; Pharr, G. M. An Improved Technique for Determining Hardness and Elastic Modulus Using Load and Displacement Sensing Indentation Experiments. *Journal of Materials Research*, 1992, *7*, 1564–1583.

(119) Wang, X.; Cui, Y.; Irudayaraj, J. Single-Cell Quantification of Cytosine Modifications by Hyperspectral Dark-Field Imaging. *ACS Nano* **2015**, *9*, 11924–11932.

(120) Carlson, A.; Bowen, A. M.; Huang, Y.; Nuzzo, R. G.; Rogers, J. a. Transfer Printing Techniques for Materials Assembly and Micro/nanodevice Fabrication. *Adv. Mater.* **2012**, *24*, 5284–5318.

(121) Thomann, I.; Pinaud, B. a; Chen, Z.; Clemens, B. M.; Jaramillo, T. F.; Brongersma, M. L. Plasmon Enhanced Solar-to-Fuel Energy Conversion. *Nano Lett.* **2011**, *11*, 3440–3446.

(122) Ferry, V. E.; Sweatlock, L. a; Pacifici, D.; Atwater, H. a. Plasmonic Nanostructure Design for Efficient Light Coupling into Solar Cells. *Nano Lett.* **2008**, *8*, 4391–4397.

(123) Pillai, S.; Catchpole, K. R.; Trupke, T.; Green, M. a. Surface Plasmon Enhanced Silicon Solar Cells. *J. Appl. Phys.* **2007**, *101*, 093105.

(124) Kamat, P. V. Meeting the Clean Energy Demand: Nanostructure Architectures for Solar Energy Conversion. *J. Phys. Chem. C* **2007**, *111*, 2834–2860.

(125) Liang, H.; Li, Z.; Wang, W.; Wu, Y.; Xu, H. Highly Surface-Roughened â€œFlower-Likeâ€ • Silver Nanoparticles for Extremely Sensitive Substrates of Surface-Enhanced Raman Scattering. *Adv. Mater.* **2009**, *21*, 4614–4618.

(126) Wang, Y.; Becker, M.; Wang, L.; Liu, J.; Scholz, R.; Peng, J.; Go, U.; Christiansen, S.; Kim, D. H.; Steinhart, M. Nanostructured Gold Films for SERS by Block Copolymer-Templated Galvanic Displacement Reactions.

(127) Li, J. F.; Huang, Y. F.; Ding, Y.; Yang, Z. L.; Li, S. B.; Zhou, X. S.; Fan, F. R.; Zhang, W.; Zhou, Z. Y.; Wu, D. Y.; *et al.* Shell-Isolated Nanoparticle-Enhanced Raman Spectroscopy. *Nature* **2010**, *464*, 392–395.

(128) Bardhan, R.; Grady, N.; Cole, J.; Joshi, A.; Halas, N. Fluorescence Enhancement by Au Nanostructures: Nanoshells and Nanorods. *ACS Nano* **2009**, *3*.

(129) Anger, P.; Bharadwaj, P.; Novotny, L. Enhancement and Quenching of Single-Molecule Fluorescence. *Phys. Rev. Lett.* **2006**, *96*, 113002.

(130) Pompa, P. P.; Martiradonna, L.; Torre, a Della; Sala, F. Della; Manna, L.; De Vittorio, M.; Calabi, F.; Cingolani, R.; Rinaldi, R. Metal-Enhanced Fluorescence of Colloidal Nanocrystals with Nanoscale Control. *Nat. Nanotechnol.* **2006**, *1*, 126–130.

(131) Aslan, K.; Wu, M.; Lakowicz, J. R.; Geddes, C. D. Fluorescent Core - Shell Ag @ SiO 2 Nanocomposites for Metal-Enhanced Fluorescence and Single Nanoparticle Sensing Platforms. **2007**, 1524–1525.

(132) Huang, X.; El-Sayed, I. H.; Qian, W.; El-Sayed, M. a. Cancer Cell Imaging and Photothermal Therapy in the near-Infrared Region by Using Gold Nanorods. *J. Am. Chem. Soc.* **2006**, *128*, 2115–2120.

(133) Kim, J.; Park, S.; Lee, J. E.; Jin, S. M.; Lee, J. H.; Lee, I. S.; Yang, I.; Kim, J.-S.; Kim, S. K.; Cho, M.-H.; *et al.* Designed Fabrication of Multifunctional Magnetic Gold Nanoshells and Their Application to Magnetic Resonance Imaging and Photothermal Therapy. *Angew. Chemie* **2006**, *118*, 7918–7922.

(134) Loo, C.; Lowery, A.; Halas, N.; West, J.; Drezek, R. Immunotargeted Nanoshells for Integrated Cancer Imaging and Therapy. *Nano Lett.* **2005**, *5*, 709–711.

(135) Cheng, L.; Yang, K.; Li, Y.; Chen, J.; Wang, C.; Shao, M.; Lee, S.-T.; Liu, Z. Facile Preparation of Multifunctional Upconversion Nanoprobes for Multimodal Imaging and Dual-Targeted Photothermal Therapy. *Angew. Chemie* **2011**, *123*, 7523–7528.

(136) Xu, H.; Käll, M. Surface-Plasmon-Enhanced Optical Forces in Silver Nanoaggregates. *Phys. Rev. Lett.* **2002**, *89*, 246802.

(137) Roxworthy, B. J.; Ko, K. D.; Kumar, A.; Fung, K. H.; Chow, E. K. C.; Liu, G. L.; Fang, N. X.; Toussaint, K. C. Application of Plasmonic Bowtie Nanoantenna Arrays for Optical Trapping, Stacking, and Sorting. *Nano Lett.* **2012**, *12*, 796–801.

(138) Schurig, D.; Mock, J. J.; Justice, B. J.; Cummer, S. a; Pendry, J. B.; Starr, a F.; Smith, D. R. Metamaterial Electromagnetic Cloak at Microwave Frequencies. *Science* **2006**, *314*, 977–980.

(139) Cai, W.; Chettiar, U. K.; Kildishev, A. V.; Shalaev, V. M. Optical Cloaking with Metamaterials. *Nat. Photonics* **2007**, *1*, 224–227.

(140) Pendry, J. B. Negative Refraction Makes a Perfect Lens. *Phys. Rev. Lett.* **2000**, *85*, 3966–3969.

(141) Chen, K.-P.; Drachev, V. P.; Borneman, J. D.; Kildishev, A. V; Shalaev, V. M. Drude Relaxation Rate in Grained Gold Nanoantennas. *Nano Lett.* **2010**, *10*, 916–922.

(142) Huang, J.-S.; Callegari, V.; Geisler, P.; Brüning, C.; Kern, J.; Prangsma, J. C.; Wu, X.; Feichtner, T.; Ziegler, J.; Weinmann, P.; *et al.* Atomically Flat Single-Crystalline Gold Nanostructures for Plasmonic Nanocircuitry. *Nat. Commun.* **2010**, *1*, 150.

(143) Hu, Y.; Kumar, P.; Xuan, Y.; Deng, B.; Qi, M.; Cheng, G. J. Controlled and Stabilized Light-Matter Interaction in Graphene: Plasmonic Film with Large-Scale 10-Nm Lithography. *Adv. Opt. Mater.* **2016**, *4*, 1811–1823.

(144) Hu, Y.; Kumar, P.; Xu, R.; Zhao, K.; Cheng, G. J. Ultrafast Direct Fabrication of Flexible Substrate-Supported Designer Plasmonic Nanoarrays. *Nanoscale* **2016**, *8*, 172–182.

(145) Gao, H.; Hu, Y.; Xuan, Y.; Li, J.; Yang, Y.; Martinez, R. V.; Li, C.; Luo, J.; Qi, M.; Cheng, G. J. Large-Scale Nanoshaping of Ultrasmooth 3D Crystalline Metallic Structures. *Science (80-.).* **2014**, *346*, 1352–1356.

(146) Zhu, W.; Rukhlenko, I. D.; Premaratne, M. Graphene Metamaterial for Optical Reflection Modulation. *Appl. Phys. Lett.* **2013**, *102*, 241914.

(147) Li, Z.; Yu, N. Modulation of Mid-Infrared Light Using Graphene-Metal Plasmonic Antennas. *Appl. Phys. Lett.* **2013**, *102*, 131108.

(148) Plimpton, S. Fast Parallel Algorithms for Short-Range Molecular Dynamics. *J. Comput. Phys.* **1995**.

(149) Stukowski, A. Visualization and Analysis of Atomistic Simulation Data with OVITO–the Open Visualization Tool. *Model. Simul. Mater. Sci. Eng.* **2010**, *18*, 015012.

(150) Li, J.; Gao, H.; Cheng, G. J. Forming Limit and Fracture Mode of Microscale Laser Dynamic Forming. *J. Manuf. Sci. Eng.* **2010**, *132*, 061005.

(151) Pierazzo, E.; Artemieva, N.; Asphaug, E.; Baldwin, E. C.; Cazamias, J.; Coker, R.; Collins, G. S.; Crawford, D. a.; Davison, T.; Elbeshausen, D.; *et al.* Validation of Numerical Codes for Impact and Explosion Cratering: Impacts on Strengthless and Metal Targets. *Meteorit. Planet. Sci.* **2008**, *43*, 1917–1938.

(152) Karanjgaokar, N. J.; Oh, C. S.; Lambros, J.; Chasiotis, I. Inelastic Deformation of Nanocrystalline Au Thin Films as a Function of Temperature and Strain Rate. *Acta Mater.* **2012**, *60*, 5352–5361.

(153) Jonnalagadda, K.; Karanjgaokar, N.; Chasiotis, I.; Chee, J.; Peroulis, D. Strain Rate Sensitivity of Nanocrystalline Au Films at Room Temperature. *Acta Mater.* **2010**, *58*, 4674–4684.

(154) Yu, Z.; Gao, H.; Wu, W.; Ge, H.; Chou, S. Y. Fabrication of Large Area Subwavelength Antireflection Structures on Si Using Trilayer Resist Nanoimprint Lithography and Liftoff. *J. Vac. Sci. Technol. B Microelectron. Nanom. Struct.* **2003**, *21*, 2874.

(155) Gao, H.; Hu, Y.; Xuan, Y.; Li, J.; Yang, Y.; Martinez, R. V.; Li, C.; Luo, J.; Qi, M.; Cheng, G. J. Large-Scale Nanoshaping of Ultrasmooth 3D Crystalline Metallic Structures. *Science (80-.).* **2014**, *346*, 1352–1356.

(156) Vieu, C.; Carcenac, F.; Pepin, A.; Chen, Y. Electron Beam Lithography: Resolution Limits and Applications. *Appl. Surf. Sci.* **2000**, 111–117.

(157) Tseng, A. a. Recent Developments in Nanofabrication Using Focused Ion Beams. *Small* **2005**, *1*, 924–939.

(158) Choi, J.; Kim, H. J.; Wang, M. C.; Leem, J.; King, W. P.; Nam, S. Three-Dimensional Integration of Graphene via Swelling, Shrinking, and Adaptation. *Nano Lett.* **2015**, *15*, 4525–4531.

(159) Berweger, S.; Atkin, J. M.; Olmon, R. L.; Raschke, M. B. Light on the Tip of a Needle: Plasmonic Nanofocusing for Spectroscopy on the Nanoscale. *J. Phys. Chem. Lett.* **2012**, *3*, 945–952.

(160) Jain, P. K.; Huang, W.; El-Sayed, M. a. On the Universal Scaling Behavior of the Distance Decay of Plasmon Coupling in Metal Nanoparticle Pairs: A Plasmon Ruler Equation. *Nano Lett.* **2007**, *7*, 2080–2088.

(161) Wen, F.; Zhang, Y.; Gottheim, S.; King, N. S.; Zhang, Y.; Nordlander, P.; Halas, N. J. Charge Transfer Plasmons: Optical Frequency Conductances and Tunable Infrared Resonances. *ACS Nano* **2015**, *9*, 6428–6435.

(162) Zhu, X.; Shi, L.; Schmidt, M. S.; Boisen, A.; Hansen, O.; Zi, J.; Xiao, S.; Mortensen, N. A. Enhanced Light-Matter Interactions in Graphene-Covered Gold Nanovoid Arrays. *Nano Lett.* **2013**, *13*, 4690–4696.

(163) Xu, W.; Ling, X.; Xiao, J.; Dresselhaus, M. S.; Kong, J.; Xu, H.; Liu, Z.; Zhang, J. Surface Enhanced Raman Spectroscopy on a Flat Graphene Surface. *Proc. Natl. Acad. Sci.* **2012**, *109*, 9281–9286.

(164) Thompson, C. V. Solid-State Dewetting of Thin Films. *Annu. Rev. Mater. Res.* **2012**, *42*, 399–434.

(165) Chen, a. Y.; Shi, S. S.; Liu, F.; Wang, Y.; Li, X.; Gu, J. F.; Xie, X. F. Effect of Annealing Atmosphere on the Thermal Coarsening of Nanoporous Gold Films. *Appl. Surf. Sci.* **2015**, *355*, 133–138.

(166) Huang, J.-S.; Callegari, V.; Geisler, P.; Brüning, C.; Kern, J.; Prangsma, J. C.; Wu, X.; Feichtner, T.; Ziegler, J.; Weinmann, P.; *et al.* Atomically Flat Single-Crystalline Gold Nanostructures for Plasmonic Nanocircuitry. *Nat. Commun.* **2010**, *1*, 150.

(167) Wang, Y.; Ni, Z.; Hu, H.; Hao, Y.; Wong, C. P.; Yu, T.; Thong, J. T. L.; Shen, Z. X. Gold on Graphene as a Substrate for Surface Enhanced Raman Scattering Study. *Appl. Phys. Lett.* **2010**, *97*, 163111.

(168) Xu, W.; Ling, X.; Xiao, J.; Dresselhaus, M. S.; Kong, J.; Xu, H.; Liu, Z.; Zhang, J. Surface Enhanced Raman Spectroscopy on a Flat Graphene Surface. *Proc. Natl. Acad. Sci. U. S. A.* **2012**, *109*, 9281–9286.

(169) Balandin, A. a; Ghosh, S.; Bao, W.; Calizo, I.; Teweldebrhan, D.; Miao, F.; Lau, C. N. Superior Thermal Conductivity of Single-Layer Graphene. *Nano Lett.* **2008**, *8*, 902–907.

(170) Wang, L.; Uppuluri, S. M.; Jin, E. X.; Xu, X. Nanolithography Using High Transmission Nanoscale Bowtie Apertures. *Nano Lett.* **2006**, *6*, 361–364.

(171) Lim, D.-K.; Jeon, K.-S.; Hwang, J.-H.; Kim, H.; Kwon, S.; Suh, Y. D.; Nam, J.-M. Highly Uniform and Reproducible Surface-Enhanced Raman Scattering from DNA-Tailorable Nanoparticles with 1-Nm Interior Gap. *Nat. Nanotechnol.* **2011**, *6*, 452–460.

(172) Zhang, W.; Ding, F.; Li, W.-D.; Wang, Y.; Hu, J.; Chou, S. Y. Giant and Uniform Fluorescence Enhancement over Large Areas Using Plasmonic Nanodots in 3D Resonant Cavity Nanoantenna by Nanoimprinting. *Nanotechnology* **2012**, *23*, 225301.

(173) Fu, Y.; Zhang, J.; Lakowicz, J. R. Largely Enhanced Single-Molecule Fluorescence in Plasmonic Nanogaps Formed by Hybrid Silver Nanostructures. *Langmuir* **2013**, *29*, 2731–2738.

(174) Im, H.; Bantz, K. C.; Lindquist, N. C.; Haynes, C. L.; Oh, S.-H. Vertically Oriented Sub-10-Nm Plasmonic Nanogap Arrays. *Nano Lett.* **2010**, *10*, 2231–2236.

(175) Lim, D.-K.; Jeon, K.-S.; Kim, H. M.; Nam, J.-M.; Suh, Y. D. Nanogap-Engineerable Raman-Active Nanodumbbells for Single-Molecule Detection. *Nat. Mater.* **2010**, *9*, 60–67.

(176) Eftekhari, F.; Escobedo, C.; Ferreira, J.; Duan, X.; Girotto, E. M.; Brolo, A. G.; Gordon, R.; Sinton, D. Nanoholes as Nanochannels: Flow-through Plasmonic Sensing. *Anal. Chem.* **2009**, *81*, 4308–4311.

(177) Pan, L.; Bogy, D. Data Storage: Heat-Assisted Magnetic Recording. *Nat. Photonics* **2009**, *3*, 2–3.

(178) Challener, W. a.; Peng, C.; Itagi, a. V.; Karns, D.; Peng, W.; Peng, Y.; Yang, X.; Zhu, X.; Gokemeijer, N. J.; Hsia, Y.-T.; *et al.* Heat-Assisted Magnetic Recording by a near-Field Transducer with Efficient Optical Energy Transfer. *Nat. Photonics* **2009**, *3*, 220–224.

(179) Kryder, M.; Gage, E. Heat Assisted Magnetic Recording. *Proc. ...* **2008**, *96*.

(180) Neumann, L.; Pang, Y.; Houyou, A.; Juan, M. L.; Gordon, R.; van Hulst, N. F. Extraordinary Optical Transmission Brightens near-Field Fiber Probe. *Nano Lett.* **2011**, *11*, 355–360.

(181) Pernice, W. H. P.; Li, M.; Garcia-Sanchez, D.; Tang, H. X. Analysis of Short Range Forces in Opto-Mechanical Devices with a Nanogap. *Opt. Express* **2010**, *18*, 12615–12621.

(182) Tsuboi, Y.; Shoji, T.; Kitamura, N.; Takase, M.; Murakoshi, K.; Mizumoto, Y.; Ishihara, H. Optical Trapping of Quantum Dots Based on Gap-Mode-Excitation of Localized Surface Plasmon. *J. Phys. Chem. Lett.* **2010**, *1*, 2327–2333.

(183) Zhang, W.; Huang, L.; Santschi, C.; Martin, O. J. F. Trapping and Sensing 10 Nm Metal Nanoparticles Using Plasmonic Dipole Antennas. *Nano Lett.* **2010**, *10*, 1006–1011.

(184) Chen, X.; Guo, Z.; Yang, G.-M.; Li, J.; Li, M.-Q.; Liu, J.-H.; Huang, X.-J. Electrical Nanogap Devices for Biosensing. *Mater. Today* **2010**, *13*, 28–41.

(185) Min, S. K.; Kim, W. Y.; Cho, Y.; Kim, K. S. Fast DNA Sequencing with a Graphene-Based Nanochannel Device. *Nat. Nanotechnol.* **2011**, *6*, 162–165.

(186) Ivanov, A. P.; Instuli, E.; McGilvery, C. M.; Baldwin, G.; McComb, D. W.; Albrecht, T.; Edel, J. B. DNA Tunneling Detector Embedded in a Nanopore. *Nano Lett.* **2011**, *11*, 279–285.

(187) Lee, J. H.; Chung, S.; Kim, S. J.; Han, J. Poly (Dimethylsiloxane) -Based Protein Preconcentration Using a Nanogap Generated by Junction Gap Breakdown Key to the Application of Proteomics in a Biological System . **2007**, *79*, 6868–6873.

(188) Partel, S.; Dincer, C.; Kasemann, S.; Kieninger, J.; Edlinger, J.; Urban, G. Lift-Off Free Fabrication Approach for Periodic Structures with Tunable Nano Gaps for Interdigitated Electrode Arrays. *ACS Nano* **2015**, acsnano.5b06405.

(189) Liang, X.; Chou, S. Y. Nanogap Detector inside Nanofluidic Channel for Fast Real-Time Label-Free DNA Analysis. *Nano Lett.* **2008**, *8*, 1472–1476.

(190) Liu, Z.; Boltasseva, A.; Pedersen, R. H.; Bakker, R.; Kildishev, A. V.; Drachev, V. P.; Shalaev, V. M. Plasmonic Nanoantenna Arrays for the Visible. *Metamaterials* **2008**, *2*, 45–51.

(191) Liu, N.; Tang, M. L.; Hentschel, M.; Giessen, H.; Alivisatos, a P. Nanoantenna-Enhanced Gas Sensing in a Single Tailored Nanofocus. *Nat. Mater.* **2011**, *10*, 631–636.

(192) Barcelo, S. J.; Kim, A.; Wu, W.; Li, Z. Fabrication of Deterministic Nanostructure Assemblies with Sub-Nanometer Spacing Using a Nanoimprinting Transfer Technique. *ACS Nano* **2012**, *6*, 6446–6452.

(193) Fursina, a.; Lee, S.; Sofin, R. G. S.; Shvets, I. V.; Natelson, D. Nanogaps with Very Large Aspect Ratios for Electrical Measurements. *Appl. Phys. Lett.* **2008**, *92*, 113102.

(194) Thompson, C. V. Solid-State Dewetting of Thin Films. *Annu. Rev. Mater. Res.* **2012**, *42*, 399–434.

(195) Ding, T.; Sigle, D.; Zhang, L.; Mertens, J.; de Nijs, B.; Baumberg, J. Controllable Tuning Plasmonic Coupling with Nanoscale Oxidation. *ACS Nano* **2015**, *9*, 6110–6118.

(196) Huang, F.; Baumberg, J. J. Actively Tuned Plasmons on Elastomerically Driven Au Nanoparticle Dimers. *Nano Lett.* **2010**, *10*, 1787–1792.

(197) Aksu, S.; Huang, M.; Artar, A.; Yanik, A. a; Selvarasah, S.; Dokmeci, M. R.; Altug, H. Flexible Plasmonics on Unconventional and Nonplanar Substrates. *Adv. Mater.* **2011**, *23*, 4422–4430.

(198) Clark, A. W.; Thompson, D. G.; Graham, D.; Cooper, J. M. Engineering DNA Binding Sites to Assemble and Tune Plasmonic Nanostructures. *Adv. Mater.* **2014**, *26*, 4286–4292.

(199) Hu, Y.; Xuan, Y.; Wang, X.; Deng, B.; Saei, M.; Jin, S.; Irudayaraj, J.; Cheng, G. J. Superplastic Formation of Metal Nanostructure Arrays with Ultrafine Gaps. *Adv. Mater.* **2016**, *28*, 9152–9162.

(200) Greer, J. R.; Oliver, W. C.; Nix, W. D. Size Dependence of Mechanical Properties of Gold at the Micron Scale in the Absence of Strain Gradients. *Acta Mater.* **2005**, *53*, 1821–1830.

(201) Jennings, A. T.; Burek, M. J.; Greer, J. R. Microstructure versus Size: Mechanical Properties of Electroplated Single Crystalline Cu Nanopillars. *Phys. Rev. Lett.* **2010**, *104*, 135503.

(202) Gurrutxaga-Lerma, B.; Balint, D. S.; Dini, D.; Eakins, D. E.; Sutton, A. P. Attenuation of the Dynamic Yield Point of Shocked Aluminum Using Elastodynamic Simulations of Dislocation Dynamics. *Phys. Rev. Lett.* **2015**, *114*, 1–5.

(203) Ravelo, R.; Germann, T. C.; Guerrero, O.; An, Q.; Holian, B. L. Shock-Induced Plasticity in Tantalum Single Crystals: Interatomic Potentials and Large-Scale Molecular-Dynamics Simulations. *Phys. Rev. B* **2013**, *88*, 134101.

(204) Nix, W. D.; Gao, H. Indentation Size Effects in Crystalline Materials: A Law for Strain Gradient Plasticity. *J. Mech. Phys. Solids* **1998**, *46*, 411–425.

(205) Ionescu, A. M. Electronic Devices: Nanowire Transistors Made Easy. *Nat. Nanotechnol.* **2010**, *5*, 178–179.

(206) Xu, S.; Qin, Y.; Xu, C.; Wei, Y.; Yang, R.; Wang, Z. L. Self-Powered Nanowire Devices. *Nat. Nanotechnol.* **2010**, *5*, 366–373.

(207) Ju, S.; Facchetti, A.; Xuan, Y.; Liu, J.; Ishikawa, F.; Ye, P.; Zhou, C.; Marks, T. J.; Janes, D. B. Fabrication of Fully Transparent Nanowire Transistors for Transparent and Flexible Electronics. *Nat. Nanotechnol.* **2007**, *2*, 378–384.

(208) Husain, a.; Hone, J.; Postma, H. W. C.; Huang, X. M. H.; Drake, T.; Barbic, M.; Scherer, a.; Roukes, M. L. Nanowire-Based Very-High-Frequency Electromechanical Resonator. *Appl. Phys. Lett.* **2003**, *83*, 1240–1242.

(209) Adachi, M. M.; Anantram, M. P.; Karim, K. S. Core-Shell Silicon Nanowire Solar Cells. *Sci. Rep.* **2013**, *3*, 2–7.

(210) Cao, L.; White, J. S.; Park, J.-S.; Schuller, J. a; Clemens, B. M.; Brongersma, M. L. Engineering Light Absorption in Semiconductor Nanowire Devices. *Nat. Mater.* **2009**, *8*, 643–647.

(211) Babinec, T. M.; Hausmann, B. J. M.; Khan, M.; Zhang, Y.; Maze, J. R.; Hemmer, P. R.; Loncar, M. A Diamond Nanowire Single-Photon Source. *Nat. Nanotechnol.* **2010**, *5*, 195–199.

(212) Li, Y.; Qian, F.; Xiang, J.; Lieber, C. M. Nanowire Electronic and Optoelectronic Devices. *Mater. Today* **2006**, *9*, 18–27.

(213) Gu, F.; Yang, Z.; Yu, H.; Xu, J.; Wang, P.; Tong, L.; Pan, A. Spatial Bandgap Engineering along Single Alloy Nanowires. *J. Am. Chem. Soc.* **2011**, *133*, 2037–2039.

(214) Shin, J. C.; Kim, K. H.; Yu, K. J.; Hu, H.; Yin, L.; Ning, C.; Rogers, J. a; Zuo, J.; Li, X. In X Ga 1- X As Nanowires on Silicon: One-Dimensional Heterogeneous Epitaxy, Bandgap Engineering, and Photovoltaics. *Nano Lett.* **2011**, *11*, 4831–4838.

(215) Myalitsin, A.; Strelow, C.; Wang, Z.; Li, Z.; Kipp, T.; Mews, A. Diameter Scaling of the Optical Band Gap in Individual CdSe Nanowires Diameter Scaling of the Optical Band Gap in Individual CdSe Nanowires. **2011**, 7920–7927.

(216) Smith, D. a.; Holmberg, V. C.; Lee, D. C.; Korgel, B. a. Young's Modulus and Size-Dependent Mechanical Quality Factor of Nanoelectromechanical Germanium Nanowire Resonators. *J. Phys. Chem. C* **2008**, *112*, 10725–10729.

(217) Hoffmann, S.; Utke, I.; Moser, B.; Michler, J.; Christiansen, S. H.; Schmidt, V.; Senz, S.; Werner, P.; Gösele, U.; Ballif, C. Measurement of the Bending Strength of Vapor-Liquid-Solid Grown Silicon Nanowires. *Nano Lett.* **2006**, *6*, 622–625.

(218) Ieong, M. Silicon Device Scaling to the Sub-10-Nm Regime. *Science (80-.).* **2004**, *306*, 2057–2060.

(219) Zhang, F.; Crespi, V. H.; Zhang, P. Prediction That Uniaxial Tension along 111 Produces a Direct Band Gap in Germanium. *Phys. Rev. Lett.* **2009**, *102*, 1–4.

(220) Murphy-Armando, F.; Fahy, S. Giant Enhancement of N-Type Carrier Mobility in Highly Strained Germanium Nanostructures. *J. Appl. Phys.* **2011**, *109*.

(221) Audoit, G.; Mhuircheartaigh, É. N.; Lipson, S. M.; Morris, M. a.; Blau, W. J.; Holmes, J. D. Strain Induced Photoluminescence from Silicon and Germanium Nanowire Arrays. *J. Mater. Chem.* **2005**, *15*, 4809.

(222) Liu, J.; Sun, X.; Camacho-Aguilera, R.; Kimerling, L. C.; Michel, J. Ge-on-Si Laser Operating at Room Temperature. *Opt. Lett.* **2010**, *35*, 679–681.

(223) Quereda, J.; San-Jose, P.; Parente, V.; Vaquero-Garzon, L.; Molina-Mendoza, A. J.; Agraït, N.; Rubio-Bollinger, G.; Guinea, F.; Roldán, R.; Castellanos-Gomez, A. Strong Modulation of Optical Properties in Black Phosphorus through Strain-Engineered Rippling. *Nano Lett.* **2016**, *16*, 2931–2937.

(224) Manzeli, S.; Allain, A.; Ghadimi, A.; Kis, A. Piezoresistivity and Strain-Induced Band Gap Tuning in Atomically Thin MoS_2. *Nano Lett.* **2015**, *15*, 5330–5335.

(225) Gill, S. T.; Hinnefeld, J. H.; Zhu, S.; Swanson, W. J.; Li, T.; Mason, N. Mechanical Control of Graphene on Engineered Pyramidal Strain Arrays. *ACS Nano* **2015**, *9*, 5799–5806.

(226) Lu, J.; Bao, Y.; Su, C. L.; Loh, K. P. Properties of Strained Structures and Topological Defects in Graphene. *ACS Nano* **2013**, *7*, 8350–8357.

(227) Desai, S. B.; Seol, G.; Kang, J. S.; Fang, H.; Battaglia, C.; Kapadia, R.; Ager, J. W.; Guo, J.; Javey, A. Strain Induced Indirect to Direct Bandgap Transition in Multilayer WSe2. *Nano Lett.* **2014**, DOI:10.1021/nl501638a.

(228) Smith, D. a; Holmberg, V. C.; Korgel, B. a. Flexible Germanium Nanowires: Ideal Strength, Room Temperature Plasticity, and Bendable Semiconductor Fabric. *ACS Nano* **2010**, *4*, 2356–2362.

(229) Süess, M. J.; Geiger, R.; Minamisawa, R. a.; Schiefler, G.; Frigerio, J.; Chrastina, D.; Isella, G.; Spolenak, R.; Faist, J.; Sigg, H. Analysis of Enhanced Light Emission from Highly Strained Germanium Microbridges. *Nat. Photonics* **2013**, *7*, 466–472.

(230) Greil, J.; Lugstein, a; Zeiner, C.; Strasser, G.; Bertagnolli, E. Tuning the Electro-Optical Properties of Germanium Nanowires by Tensile Strain. *Nano Lett.* **2012**, *12*, 6230–6234.

(231) Ryu, S. Y.; Xiao, J.; Park, W. Il; Son, K. S.; Huang, Y. Y.; Paik, U.; Rogers, J. a. Lateral Buckling Mechanics in Silicon Nanowires on Elastomeric Substrates. *Nano Lett.* **2009**, *9*, 3214–3219.

(232) Xu, F.; Lu, W.; Zhu, Y. Controlled 3D Buckling of Silicon Nanowires for Stretchable Electronics. *ACS Nano* **2011**, *5*, 672–678.

(233) Kumar, P.; Li, J.; Nian, Q.; Hu, Y.; Cheng, G. J. Plasmonic Tuning of Silver Nanowires by Laser Shock Induced Lateral Compression. *Nanoscale* **2013**, *5*, 6311.

(234) Hu, Y.; Li, J.; Tian, J.; Xuan, Y.; Deng, B.; McNear, K. L.; Lim, D. G.; Chen, Y.; Yang, C.; Cheng, G. J. Parallel Nanoshaping of Brittle Semiconductor Nanowires for Strained Electronics. *Nano Lett.* **2016**, acs.nanolett.6b03366.

(235) Roberts, M. E.; Queraltó, N.; Mannsfeld, S. C. B.; Reinecke, B. N.; Knoll, W.; Bao, Z. Cross-Linked Polymer Gate Dielectric Films for Low-Voltage Organic Transistors. *Chem. Mater.* **2009**, *21*, 2292–2299.

(236) Klauk, H.; Halik, M.; Zschieschang, U.; Schmid, G.; Radlik, W.; Weber, W. High-Mobility Polymer Gate Dielectric Pentacene Thin Film Transistors. *J. Appl. Phys.* **2002**, *92*, 5259.

(237) Chen, F. C.; Chu, C. W.; He, J.; Yang, Y.; Lin, J. L. Organic Thin-Film Transistors with Nanocomposite Dielectric Gate Insulator. *Appl. Phys. Lett.* **2004**, *85*, 3295–3297.

(238) Javey, A.; Nam, S.; Friedman, R. S.; Yan, H.; Lieber, C. M. Layer-by-Layer Assembly of Nanowires for Three-Dimensional, Multifunctional Electronics. *Nano Lett.* **2007**, *7*, 773–777.

(239) Ramachandramoorthy, R.; Gao, W.; Bernal, R.; Espinosa, H. High Strain Rate Tensile Testing of Silver Nanowires: Rate-Dependent Brittle-to-Ductile Transition. *Nano Lett.* **2015**, acs.nanolett.5b03630.

(240) Peng, C. Y.; Huang, C. F.; Fu, Y. C.; Yang, Y. H.; Lai, C. Y.; Chang, S. T.; Liu, C. W. Comprehensive Study of the Raman Shifts of Strained Silicon and Germanium. *J. Appl. Phys.* **2009**, *105*.

(241) Süess, M. J.; Minamisawa, R. A.; Geiger, R.; Bourdelle, K. K.; Sigg, H.; Spolenak, R. Power-Dependent Raman Analysis of Highly Strained Si Nanobridges. *Nano Lett.* **2014**.

(242) Süess, M. J.; Geiger, R.; Minamisawa, R. a.; Schiefler, G.; Frigerio, J.; Chrastina, D.; Isella, G.; Spolenak, R.; Faist, J.; Sigg, H. Analysis of Enhanced Light Emission from Highly Strained Germanium Microbridges. *Nat. Photonics* **2013**, *7*, 466–472.

(243) Riddet, C.; Watling, J. R.; Chan, K. H.; Parker, E. H. C.; Whall, T. E.; Leadley, D. R.; Asenov, A. Hole Mobility in Germanium as a Function of Substrate and Channel Orientation, Strain, Doping, and Temperature. *IEEE Trans. Electron Devices* **2012**, *59*, 1878–1884.

VITA

EDUCATION:

Ph. D. in Industrial Engineering, Purdue University, West Lafayette, IN, 2016

Advisor: Gary J. Cheng

Title of Dissertation: "Laser Shock Imprinting of Metallic Nanostructures and Shock Processing of Low-dimensional Materials"

M.S. Institute of Mechanics, Chinese Academy of Sciences (CAS), Beijing, China, 2012

Advisors: Xiuli He and Gang Yu

Title of Dissertation: "Heat and mass transfer in laser dissimilar welding"

B.S. in Engineering Mechanics, Southeast University (SEU), Nanjing, P. R. China, 2009

RESEARCH INTEREST:

- Laser based manufacturing: laser shock imprinting, surface patterning and micro/nano-structuring; Laser shock induced post-fabrication tuning of metallic nanostructures; laser welding, laser surface remelting; laser-matter interaction.
- Ultra-high strain-rate deformation and straining of single/multi- layers of graphene, Transition metal dichalcogenide (TMD), and semiconductor nanowires (1D).
- Laser shock wrapping of 2D materials on 3D structures.
- Heat and mass transfer and nanomechanics in laser material processing.

PUBLICATIONS

- **Hu, Y**.; Li, J.; Tian, J.; Xuan, Y.; Deng, B.; McNear, K. L.; Lim, D. G.; Chen, Y.; Yang, C.; Cheng, G. J. Parallel Nanoshaping of Brittle Semiconductor Nanowires for Strained Electronics. Nano Lett. 2016, acs.nanolett.6b03366.
- **Hu, Y**.; Xuan, Y.; Wang, X.; Deng, B.; Saei, M.; Jin, S.; Irudayaraj, J.; Cheng, G. J. Superplastic Formation of Metal Nanostructure Arrays with Ultrafine Gaps. Adv. Mater. 2016, 28, 9152–9162.
- **Hu, Y**.; Kumar, P.; Xuan, Y.; Deng, B.; Qi, M.; Cheng, G. J. Controlled and Stabilized Light-Matter Interaction in Graphene: Plasmonic Film with Large-Scale 10-Nm Lithography. *Adv. Opt. Mater.* **2016**, *4*, 1811–1823.
- **Hu, Y**.; Kumar, P.; Xu, R.; Zhao, K.; Cheng, G. J. Ultrafast Direct Fabrication of Flexible Substrate-Supported Designer Plasmonic Nanoarrays. Nanoscale 2016, 8, 172–182.
- Nian, Q.; Saei, M.; **Hu, Y**.; Deng, B.; Jin, S.; Cheng, G. J. Additive Roll Printing Activated Cold Welding of 2D Crystals and 1D Nanowires Layers for Flexible Transparent Conductor and Planer Energy Storage. Extrem. Mech. Lett. 2016, 1–15.
- Jin, S.; Ziabari, A.; Koh, Y. R.; Saei, M.; Wang, X.; Deng, B.; **Hu, Y**.; Bahk, J.-H.; Shakouri, A.; Cheng, G. J. Enhanced Thermoelectric Performance of P-Type View the MathML Source Nanowires with Pulsed Laser Assisted Electrochemical Deposition. Extrem. Mech. Lett. 2016, 1–11.
- Hu, Z.; Tong, G.; Lin, D.; Nian, Q.; Shao, J.; **Hu, Y**.; Saeib, M.; Jin, S.; Cheng, G. J. Laser Sintered Graphene Nickel Nanocomposites. J. Mater. Process. Technol. 2016, 231, 143–150.
- Hu, Z.; Saei, M.; Tong, G.; Lin, D.; Nian, Q.; **Hu, Y**.; Jin, S.; Xu, J.; Cheng, G. J. Numerical Simulation of Temperature Field Distribution for Laser Sintering Graphene Reinforced Nickel Matrix Nanocomposites. J. Alloys Compd. 2016, 688, 438–448.
- Ouyang, L.; **Hu, Y**.; Zhu, L.; Cheng, G. J.; Irudayaraj, J. A Reusable Laser Wrapped Graphene-Ag Array Based SERS Sensor for Trace Detection of Genomic DNA Methylation. Biosens. Bioelectron. 2016.
- **Hu, Y**.; He, X.; Yu, G.; Zhao, S. Capillary Convection in Pulsed - Butt Welding of Miscible Dissimilar Couple. Proc. Inst. Mech. Eng. Part C J. Mech. Eng. Sci. 2016, 0, 1–12.
- **Hu, Y**.; He, X.; Yu, G.; Li, S.; Zheng, C.; Ning, W. Experimental and Numerical Study on Laser Keyhole Welding of 42CrMo under Air and Argon Atmosphere. Int. J. Adv. Manuf. Technol. 2016.

- Lee, S. *; Kumar, P. *; **Hu, Y**. *; Cheng, G. J.; Irudayaraj, J. Graphene Laminated Gold Bipyramids as Sensitive Detection Platforms for Antibiotic Molecules. Chem. Commun. 2015, 51, 15494–15497. (* co-leading authors)
- **Hu, Y**. *; Lee, S. *; Kumar, P.; Nian, Q.; Wang, W.; Irudayaraj, J.; Cheng, G. J. Water Flattens Graphene Wrinkles: Laser Shock Wrapping of Graphene onto Substrate-Supported Crystalline Plasmonic Nanoparticle Arrays. Nanoscale 2015, 7, 19885–19893. (* co-leading authors)
- Liu, J.; Kumar, P.; **Hu, Y**.; Cheng, G. J.; Irudayaraj, J. Enhanced Multiphoton Emission from CdTe/ZnS Quantum Dots Decorated on Single-Layer Graphene. J. Phys. Chem. C 2015, 119, 6331–6336.
- Gao, H. *; **Hu, Y**. *; Xuan, Y. *; Li, J.; Yang, Y.; Martinez, R. V.; Li, C.; Luo, J.; Qi, M.; Cheng, G. J. Large-Scale Nanoshaping of Ultrasmooth 3D Crystalline Metallic Structures. Science (80-.). 2014, 346, 1352–1356. (* co-leading authors)
- Lin, D.; Nian, Q.; Deng, B. W.; Jin, S. Y.; **Hu, Y. W**.; Wang, W. Q.; Cheng, G. J. Three-Dimensional Printing of Complex Structures: Man Made or toward Nature? ACS Nano 2014, 8, 9710–9715.
- Lin, D.; Deng, B.; Sassman, S.; **Hu, Y**.; Suslov, S.; Cheng, G. J. Magnetic Field Assisted Growth of Highly Dense-Fe2O3 Single Crystal Nanosheets and Their Application in Water Treatment. RSC Adv. 2014, 4, 18621.
- Kumar, P.; Li, J.; Nian, Q.; **Hu, Y**.; Cheng, G. J. Plasmonic Tuning of Silver Nanowires by Laser Shock Induced Lateral Compression. Nanoscale 2013, 5, 6311.
- **Hu, Y**.; He, X.; Yu, G.; Ge, Z.; Zheng, C.; Ning, W. Heat and Mass Transfer in Laser Dissimilar Welding of Stainless Steel and Nickel. Appl. Surf. Sci. 2012, 258, 5914–5922.
- Zhao, S.; Yu, G.; He, X.; **Hu, Y**. Microstructural and Mechanical Characteristics of Laser Welding of Ti6Al4V and Lead Metal. J. Mater. Process. Technol. 2012, 212, 1520–1527.